Draft version February 17, 2021
Preprint typeset using LaTeX style emulateapj v. 5/14/03

MODEL LIGHT CURVES FOR TYPE IB AND IC SUPERNOVAE

S. E. Woosley[1], Tuguldur Sukhbold[2,3,4], and D. N. Kasen[5,6]

Draft version February 17, 2021

ABSTRACT

Using the Monte Carlo code, SEDONA, multiband photometry and spectra are calculated for supernovae derived from stripped helium stars with presupernova masses from 2.2 to 10.0 $M_\odot$. The models are representative of evolution in close binaries and have previously been exploded using a parametrized one-dimensional model for neutrino-transport. A subset, those with presupernova masses in the range 2.2 - 5.6 $M_\odot$, have many properties in common with observed Type Ib and Ic supernovae, including a median ejected mass near 2 $M_\odot$, explosion energies near 1×10^{51} erg, typical ^{56}Ni masses 0.07 - 0.09 $M_\odot$, peak times of about 20 days, and a narrow range for the V-R color index 10 days post V-maximum near 0.3 mag. The median peak bolometric luminosity, near $10^{42.3}$ erg s^{-1}, is fainter, however, than for several observational tabulations and the brightest explosion has a bolometric luminosity of only $10^{42.50}$ erg s^{-1}. The brightest absolute B, V, and R magnitudes at peak are -17.2, -17.8, and -18.0. These limits are fainter than some allegedly typical Type Ib and Ic supernovae and could reflect problems in our models or the observational analysis. Helium stars with lower and higher masses also produce interesting transients that may have been observed including fast, faint, blue transients and long, red, faint Type Ic supernovae. New models are specifically presented for SN 2007Y, SN 2007gr, SN 2009jf, LSQ13abf, SN 2008D, and SN 2010X.

Subject headings: stars: binaries, supernovae:general, supernovae: individual SN 2007Y, SN 2007gr, SN 2009jf, LSQ13abf, SN 2008D, SN 2010X

1. INTRODUCTION

In a series of papers (Woosley 2019; Ertl et al. 2020; Woosley, Sukhbold, & Janka 2020), we have explored the observational consequences of helium stars evolved with mass loss. The intent of these papers has been to capture some of the essential elements of massive stellar evolution in binary systems with sufficiently close separations that the envelope of one or both stars is lost to its companion when the star starts to become a red supergiant. While the treatment of the binary interaction itself is crude - the entire envelope is assumed to be lost at central helium ignition - these studies have the advantage of including a broad range of masses and following the evolution through the final stages of core collapse and explosion in a realistic way.

Because of the limitations of the KEPLER code (Weaver, Zimmerman, & Woosley 1978) and the interesting upper bound it gave on supernova luminosities, it is worthwhile to repeat the calculations of light curves in Ertl et al. (2020) with a better treatment of the radiation transport. KEPLER does not give reliable estimates of the photometry and spectra that are of great interest to observers. The present paper uses the SEDONA, an implicit Monte-Carlo code that includes the effects of tens of millions of lines, to compute the light curves and spectra. While the version of SEDONA employed here also has limitations, such as assuming a homologously coasting state for the ejecta and local thermodynamic equilibrium (LTE), using it can make a better connection between the explosion models and several recent compilations of observational data.

The paper is observationally oriented. Bolometric luminosities are calculated, but also absolute magnitudes for various filters, color indices, light curve shapes, peak magnitude distributions, and spectra. In six cases, these results are compared with specific historic supernovae. In the end, the case is compelling that most stripped envelope supernovae are best understood in a traditional scenario of binary mass exchange, neutrino-powered explosions without rotation, and radioactivity-illuminated light curves. There remains, however, a puzzling minority of observed events that are too bright. This could reflect deficiencies in the one-dimensional explosion models, errors in estimating bolometric luminosities from its components by the observers, errors in extinction corrections or distances, or the existence of more than one mechanism operating to explode and illuminate common stripped-envelope supernovae. We return to these issues in the conclusions (§6).

2. MODELS AND CODES

2.1. *Explosion Models*

The presupernova evolution of mass-losing helium stars was studied by Woosley (2019) for star masses, at helium ignition, from 1.6 $M_\odot$ to 120 $M_\odot$. This range corresponds to main sequence masses from approximately 10 to 250 $M_\odot$. For standard assumptions regarding mass loss (Yoon 2017, with $f_{\rm WR} = 1$), helium stars with initial masses below 2.5 $M_\odot$ were found to produce white dwarfs or electron-capture supernova and their final evolution was not followed. For the other stars, mass loss resulted in presupernova masses in the range 2 to 60 $M_\odot$. The effect of a larger mass loss rate, closer to that favored

[1] Department of Astronomy and Astrophysics, University of California, Santa Cruz, CA 95064
[2] Department of Astronomy, Ohio State University, Columbus, Ohio, 43210
[3] Center for Cosmology and AstroParticle Physics, Ohio State University, Columbus OH 43210
[4] NASA Hubble Fellow
[5] Department of Astronomy, University of California, Berkeley, CA 94720
[6] Lawrence Berkeley National Laboratory, Berkeley, CA, 94720

by Yoon, $f_{\rm WR} = 1.5$, was also examined.

The explosion of a large subset of these models, those that did not end up as as pulsational-pair instability supernovae or collapse directly to black holes, was simulated in a one-dimensional (1D) neutrino-transport code, PHOTB, by Ertl et al. (2020). The collapse to a black hole was determined by following the accretion onto the proto-neutron star long enough to assure that no outgoing shock emerged. In some cases not considered here, a black hole was formed by fall back even though the outer part of the star was ejected. This reduced model set consisted of 133 helium stars with initial masses from 2.5 to 40 $M_\odot$, corresponding to presupernova masses from 2.1 to 19.6 $M_\odot$. The efficiency of the neutrino-powered explosions was calibrated to SN 1987A and the Crab. The ejected mass, fall-back mass, final kinetic energy, and remnant mass were determined for each star in a self-consistent way that depended upon the progenitor structure. Considerable attention was paid to limits on the amount of ^{56}Ni each explosion produced, and lower and upper bounds consistent with the (1D) neutrino-powered assumption and nucleosynthesis were established. An additional set of models with mass loss rates 1.5 times the standard Yoon values ($f_{\rm WR} = 1.5$) was also considered. More recently, Woosley, Sukhbold, & Janka (2020) used the remnant mass distributions calculated by Ertl et al. (2020) to estimate the initial mass-function averaged birth function and mean masses for black holes and neutron stars in close binary systems and found good agreement with present observables.

Ertl et al. (2020) used a variety of central engines to simulate their explosions. Their standard model was W18, but four other cases were also considered that used different presupernova models for SN 1987A. The average outcomes for these such as explosion energy, mass cut, and ^{56}Ni synthesis did not vary greatly for the five different central engines. See Figs. 2 and 3 and Table 2 of Ertl et al. (2020) and Figs. 8, 9, 13, and 17 and Table 4 of Sukhbold et al. (2016). Since we will find (§2.3; Fig. 2) that bolometric light curves calculated using SEDONA and KEPLER agree quite well, we will, with one exception, use only the models from Ertl et al. (2020) with their W18 central engine for the present study. The exception is an 8.00 $M_\odot$ helium star evolved with twice the standard mass loss rate ($f_{\rm WR} = 2$) and exploded manually without the benefit of a neutrino-transport calculation. This was necessary to examine the effects of the composition on the outcome of a star with presupernova mass low enough to be common yet composed mostly of carbon and oxygen and not helium (see §3.2 and Yoon et al. 2019). The evolution of this star gave a presupernova mass of 3.63 $M_\odot$ and an iron core of 1.48 $M_\odot$, similar to a standard model ($f_{\rm WR} = 1$) with initial mass 4.7 $M_\odot$. An explosion with final kinetic energy 1.28×10^{51} erg was generated using a piston situated near the edge of the silicon core at 1.64 $M_\odot$.

Except for this single model, the results of Ertl et al. (2020) for the bolometric properties using the other central engines remain valid and sufficient. In addition to the standard model set with $f_{\rm WR} = 1$, we continued to carry the parallel set with $f_{\rm WR} = 1.5$ which was also exploded by Ertl et al. (2020).

The supernova models used are summarized in Table 1 and Table 2. Except for the 8.0 $M_\odot$ model men-

Table 1. Properties of main models

$M_{\rm He}$ [$M_\odot$]	$M_{\rm preSN}$ [$M_\odot$]	Ni + Tr [$M_\odot$]	$3/4 \times M_{\rm NSE}$ [$M_\odot$]	$E_{\rm exp}$ [B]	$M_{\rm ej}$ [$M_\odot$]
		$f_{\rm WR} = 1$			
2.70	2.21	0.012	0.024	0.21	0.85
2.80	2.30	0.011	0.024	0.23	0.89
2.90	2.37	0.018	0.035	0.38	0.93
3.20	2.59	0.037	0.060	0.67	1.14
3.30	2.67	0.035	0.055	0.59	1.20
3.40	2.74	0.024	0.039	0.40	1.22
3.50	2.81	0.026	0.040	0.42	1.27
3.60	2.88	0.024	0.035	0.35	1.32
3.70	2.95	0.046	0.064	0.69	1.45
3.80	3.02	0.049	0.070	0.80	1.51
3.90	3.09	0.044	0.059	0.59	1.59
4.00	3.15	0.045	0.061	0.64	1.62
4.10	3.22	0.042	0.058	0.61	1.70
4.20	3.29	0.051	0.069	0.77	1.77
4.30	3.36	0.068	0.087	0.95	1.85
4.40	3.42	0.064	0.085	0.97	1.92
4.50	3.49	0.070	0.099	1.28	1.90
4.62	3.57	0.081	0.109	1.39	1.98
4.75	3.65	0.076	0.108	1.46	2.10
4.88	3.73	0.076	0.109	1.47	2.16
5.00	3.81	0.080	0.112	1.49	2.22
5.13	3.89	0.074	0.105	1.39	2.28
5.25	3.97	0.065	0.095	1.26	2.33
5.38	4.05	0.094	0.126	1.65	2.55
5.50	4.13	0.082	0.117	1.58	2.60
5.63	4.21	0.067	0.096	1.26	2.41
5.75	4.29	0.070	0.098	1.28	2.55
5.88	4.36	0.083	0.117	1.57	2.79
6.00	4.44	0.058	0.084	1.07	2.82
6.13	4.52	0.088	0.122	1.62	2.94
6.25	4.59	0.085	0.119	1.58	3.00
6.38	4.67	0.078	0.113	1.52	3.05
6.50	4.75	0.077	0.111	1.49	3.14
6.63	4.82	0.081	0.115	1.53	3.21
6.75	4.89	0.066	0.076	0.77	2.99
6.88	4.97	0.088	0.113	1.35	3.29
7.00	5.04	0.088	0.114	1.37	3.33
7.13	5.12	0.103	0.135	1.70	3.56
7.25	5.19	0.088	0.103	1.06	3.58
7.38	5.26	0.093	0.119	1.43	3.57
7.50	5.34	0.091	0.116	1.38	3.61
7.63	5.41	0.094	0.119	1.42	3.70
7.75	5.48	0.097	0.122	1.45	3.76
7.88	5.55	0.094	0.120	1.42	3.82
8.00	5.63	0.044	0.061	0.70	3.95
		$f_{\rm WR} = 1.5$			
5.00	3.43	0.094	0.124	1.60	1.85
5.50	3.70	0.087	0.115	1.47	2.08
6.00	3.96	0.087	0.118	1.56	2.32
6.50	4.21	0.068	0.098	1.30	2.50
7.00	4.45	0.077	0.109	1.45	2.84
7.50	4.69	0.077	0.108	1.39	3.02
8.00	4.92	0.076	0.110	1.47	3.26
8.50	4.90	0.089	0.114	1.35	3.18
9.00	4.87	0.052	0.078	1.01	3.14
9.50	4.88	0.093	0.118	1.40	3.16
10.0	4.96	0.084	0.106	1.24	3.21
10.5	5.08	0.077	0.092	0.96	3.45
11.0	5.19	0.090	0.105	1.13	3.44
11.5	5.32	0.079	0.095	1.02	3.60
12.0	5.43	0.076	0.092	0.99	3.71
12.5	5.53	0.101	0.124	1.41	3.82
13.0	5.64	0.094	0.115	1.30	3.98

Note. — Explosive properties are all based on `W18` engine (Ertl et al. 2020).

Table 2. Properties of special case models

$M_{\rm He}$ [$M_\odot$]	$M_{\rm preSN}$ [$M_\odot$]	Ni + Tr [$M_\odot$]	$3/4 \times M_{\rm NSE}$ [$M_\odot$]	$E_{\rm exp}$ [B]	$M_{\rm ej}$ [$M_\odot$]
$f_{\rm WR} = 2.0$			artificial explosion		
8.00x2	3.63	-	0.099	1.28	1.99
$f_{\rm WR} = 1.0$			engine = `W18`		
2.50	2.07	0.007	0.015	0.11	0.74
2.60	2.15	0.008	0.018	0.15	0.79
12.0	7.24	0.071	0.079	0.81	5.33
19.0	9.98	0.093	0.102	1.00	8.32

tioned above, quantities in the tables were adopted without modification from Ertl et al. (2020). "Ni + Tr" and "$3/4 \times M_{\rm NSE}$" refer to a typical and a maximum ^{56}Ni mass and their meanings are discussed extensively in that publication. Here, in keeping with the goal of producing the brightest possible supernovae this model set allows, the "$3/4 \times M_{\rm NSE}$" value is adopted here as standard. These values can reasonably be reduced in any light curve simulation, but not increased. $M_{\rm presn}$ and $M_{\rm ej}$ are the masses of the presupernova star and the ejecta, after any fallback is over, and $E_{\rm exp}$ is its terminal kinetic energy. For the exceptional 8.00 $M_\odot$ model that was manually exploded, a ^{56}Ni mass of 0.099 $M_\odot$ was enforced by adjusting the mass cut. The reason for this will become apparent in §3.2 when the colors of this model are compared with another (4.50 $M_\odot$; $f_{\rm WR} = 1$) model with this mass of ^{56}Ni.

The standard models that used $f_{\rm WR} = 1$ are labeled by their initial helium star mass and the prefix "He". Model He5.00 thus began its computational lifetime as a 5 $M_\odot$ helium star, lost mass using $f_{\rm WR} = 1$, and exploded with a final mass of 3.81 $M_\odot$ using the W18 central engine. The other explosion models in Table 1 that used $f_{\rm WR} = 1.5$ will have an "x1.5" attached to their name. Model He5.00x1.5 thus also began as a 5 $M_\odot$ helium star, but ended with a mass of 3.43 $M_\odot$ and was exploded using the W18 central engine. All of these models in Table 1 are candidates for normal Type Ib and Ic supernovae (§3). The files are available to those wanting to use these explosion models for their own studies.

An additional 4 low and high mass models using the same explosion and mass-loss assumptions, but not considered "normal" are given in Table 2. Model He8.00x2 had an initial mass of 8.00 $M_\odot$ but twice the standard mass loss rate.

2.2. *Use of the SEDONA Code*

SEDONA (Kasen et al. 2006, 2008; Roth & Kasen 2015) is a multi-dimensional implicit Monte Carlo code, used here in one dimension. Given the ejecta properties i.e., the density, composition, and velocity profile of the freely expanding supernova material, SEDONA does a detailed treatment of the gamma-ray transport and self-consistently determines the emergent broadband light curves and spectra. The temperature structure is solved assuming radiative equilibrium. Lines are treated in the expansion opacity formalism and assumed to be purely absorbing. Otherwise no free parameters need be adjusted in the radiative transfer calculation. It is assumed that the excited states of the various ions are in thermal equilibrium. Opacities include the effects of over 20 million iron-group lines and about 800,000 lines of hydrogen through calcium (http://kurucz.harvard.edu/vitabib.html; Kurucz 1994, 1995, 2009). The ions included here were He, C, N, O, Ne, Mg, Si, Ar, Ca, Ti, Cr, Fe, Co, and Ni. The only energy source was the decay of ^{56}Ni and ^{56}Co. Each ion except helium carried 7 stages of ionization and from 300 to 2000 levels. The initial thermal energy from the KEPLER explosion model was included.

To make a link with the explosion simulations, KEPLER models were evolved to a coasting configuration, typically 1 day, but 2 days in some of the more massive models with slower expansion speeds, and mapped into SEDONA. The original zoning was preserved except that few bottom zones with coasting speeds less than 500 km s^{-1} and surface zones moving faster than 30,000 km s^{-1} were excised. The ^{56}Ni mass and velocity of the remaining zones was then adjusted slightly so as to preserve the final total ^{56}Ni and kinetic energy given by Ertl et al. (2020, see also Table 1 and Table 2). In a few cases where sensitivity to ^{56}Ni mass was studied, the ^{56}Ni mass was multiplied by a constant and the other mass fractions renormalized so as to keep the sum of the mass fractions equal to one. Typical spatial resolution varied from 200 zones for the models with small ejected mass to 1220 zones for the heaviest model. The models were then mixed as discussed in §2.3.

Most runs were initialized with 1 million particles and added 140,000 particles per time step. Particles that escaped were allowed to leave the grid. Typical runs took about 350 time steps and terminated after 100 days. Finer time steps were used early in the calculation. The typical time step near maximum light was 0.3 days. The typical maximum number of particles on the grid at that time was 15 million. Several runs were carried out with four times the number of particles in order to obtain well converged spectra. These showed that the broadband light curves were well converged for the smaller value. Calculations were run in the LUX supercomputer at UCSC using 4 to 8 nodes (160 to 320 CPU). Run times were shorter for the lighter models with higher velocity and fewer zones, but ranged from several hours to 15 hours.

The principal output of SEDONA consists of a time series of spectra from the far UV to infrared (10^{14} to 2×10^{16} Hz; 100 to 20,000 Å). In order to generate multiband light curves, these spectra were then folded with different filter response functions (§3.2).

2.3. *Mixing*

One of the greatest uncertainties in any modeling of the multi-color light curves or spectra of Type Ib and Ic supernovae is the extent to which the ejecta, especially ^{56}Ni and ^{4}He, have been mixed. See Dessart et al. (2012), Dessart et al. (2015), and Yoon et al. (2019) for discussions. The mixing of iron-group elements to large velocity provides a source of opacity that blankets the blue and ultraviolet emission making the supernova redder at peak. The decay of ^{56}Ni provides heat that maintains ionization to a larger radius in a mixed model hence

supporting a larger photosphere and cooler effective temperature. The early color evolution of the supernova is thus especially sensitive to mixing Yoon et al. (2019). If ^{56}Ni and ^{4}He are mixed together, the decay of the former can aid in exciting lines of the latter (Lucy 1991; Dessart et al. 2012; Woosley & Eastman 1997), dramatically affecting the spectrum and even the classification of the supernova as Type Ib or Ic. Above some mass, the small residual helium may be ejected with such high velocity that, depending on mixing, no ^{56}Ni and ^{4}He commingle. Hence no strong, non-thermal lines of helium will be present in the spectrum and it will be Type Ic. But the supernova can also be Type Ic if there is a thick buffer of carbon, oxygen, and heavier elements between the ^{56}Ni and even a thick shell of helium. When ^{56}Ni is mixed to larger radii, the light curve rises earlier and may decline earlier. The peak bolometric luminosity is thus affected, though the change is generally not large.

Despite its importance, mixing in Type Ib and Ic supernova has not received nearly as much attention in multi-dimensional simulation as Type IIp. Focus in the latter has frequently been on the Rayleigh-Taylor instability created as the outgoing shock decelerates in regions of increasing ρr^3, where ρ is the local density and r the shock radius. Major mixing occurs when the helium core encounters the hydrogen envelope and is forced to decelerate. This kind of mixing is present in exploding helium stars as well, but lacking a hydrogen envelope, the consequences are not as dramatic.

A second kind of mixing occurs in all varieties of core-collapse supernovae and is driven by the essential asymmetry of the central engine. In neutrino-powered explosions, the "hot bubble" is unstable and expands at different rates for different angles. See for example, Figs 10 and 11 of Wongwathanarat et al. (2017). If a magnetar powers the explosion, similar anisotropies will exist (Chen et al. 2017). For explosions that impart their energy in a time short compared with the shock crossing time for the presupernova star, about a minute here, the final velocity of the ejected plumes depends on their initial speed and how much matter they interact with on the way out. There is usually an upper bound to their speed (Wongwathanarat et al. 2017).

As is often noted, this mixing is not microscopic. It does not lead to the homogenization of the composition. Rather material is ejected in plumes and clumps that extend to higher final velocity than some of the other ejecta that initially was at smaller radius. Mixing is thus intrinsically a multi-dimensional process that cannot be properly replicated in 1D. For a clear demonstration in nature, see the supernova remnant for Cas-A and its well studied "fast moving knots". Whatever is done here in 1D will be a gross approximation.

Many artificial prescriptions exist for mixing in one-dimensional simulations of supernovae. Most have, at their root, early attempts to model mixing in SN 1987A, and involve moving a "boxcar average" through the supernova ejecta multiple times. A boxcar with an interval of specified mass, is moved outwards through the supernova model, zone by zone until either some maximum mass or the surface of the ejecta is reached. At each zone the overlying interval is completely mixed while conserving mass. The mixing operation is often performed through the supernova several times with a decreasing mixing interval so that the final curve for abundance as a function of mass is smooth. In our previous studies (e.g. Ertl et al. 2020), an initial boxcar width of 0.15 $M_{\rm ej}$ was employed , where $M_{\rm ej}$ is the mass ejected in the supernova (presupernova mass minus remnant mass). This mixing region was moved through all the ejecta three times and then a final fourth mixing was applied using an interval half as great, i.e., 0.075 $M_{\rm ej}$. Importantly, this mixing was continued to the surface of the star, so some ^{56}Ni was mixed to arbitrarily high velocity.

A similar prescription was employed by Dessart et al. (2015), but instead of mixing in mass, they mixed in velocity intervals. Specifically, for the study of Type Ib and Ic supernovae, they recommended a 1000 km s^{-1} mixing interval as characteristic of weak mixing and 2000 km s^{-1} as representative of strong mixing and explored the consequences. The Dessart et al mixing and Ertl et al mixing are shown for Model He6.00, which ejected 2.32 M$_\odot$ (see Table 1) in Fig. 1. Note the tail extending to very high velocity for the Dessart major mixing case and the Ertl et al prescription. Since the abundance of ^{56}Ni in these high velocity zones exceeds the abundance of solar iron in the initial model, 0.0014, this will have a major effect on the spectrum.

While we could find no published three-dimensional studies of post-explosive mixing in completely stripped massive stars exploded with neutrino transport, the results should resemble closely what Wongwathanarat et al. (2017) calculated for a Type IIb supernova with a very low mass hydrogenic envelope. Their initial model had a helium and heavy element core of 4.4 M$_\odot$ capped by 0.3 M$_\odot$ of low density hydrogen envelope. The ejected mass was 3.0 M$_\odot$ of core material plus the 0.3 M$_\odot$ of envelope, and the explosion energy was 1.47×10^{51} erg. Though intended as a model for Cas-A, the helium core mass and structure of their Model W15-2-cw-IIb is very similar to Model He6.0 here (Table 1). Wongwathanarat et al. (2017) found that mixing in their ejecta was characterized by a maximum speed for ^{56}Ni of about 7000 km s^{-1} with only a small amount, about 1%, being mixed out to 7000 - 9000 km s^{-1}. They point out that this is consistent with the maximum speed seen for ^{44}Ti in Cas-A of 6300 $\pm$ 1250 km s^{-1} (Grefenstette et al. 2017). They also point out that this speed is consistent with dimensional arguments for the bulk speed $(2E/M_{\rm ej})^{1/2} \approx 7000$ km s^{-1}. Dessart et al. (2016) say that this bulk speed is characteristic of the Doppler velocity measured for He I (5875 Å) at maximum in supernovae of Type IIb and Ib. It thus seems quite doubtful that substantial ^{56}Ni will be mixed to speeds in excess of 10,000 km s^{-1} in models like He6.00. Dessart's high mixing and Ertl et al. standard mixing are thus unrealistic at high speeds where the ejected material has been accelerated by a shock going down a density gradient.

With admittedly large residual uncertainty, we adopt a mixing formalism where the bulk of the ^{56}Ni and other heavy elements is mixed out to a speed given by the bulk velocity. That is the mixing is characterized by a maximum speed of

$$v_{\rm mix} \;=\; 6000 \left(\frac{E_{51}}{M_{\rm ej}/3{\rm M}_\odot} \right)^{1/2} \;{\rm km\ s^{-1}} \qquad (1)$$

where E_{51} is the kinetic energy of the ejecta in units of 10^{51} erg. To account for a small amount of material at

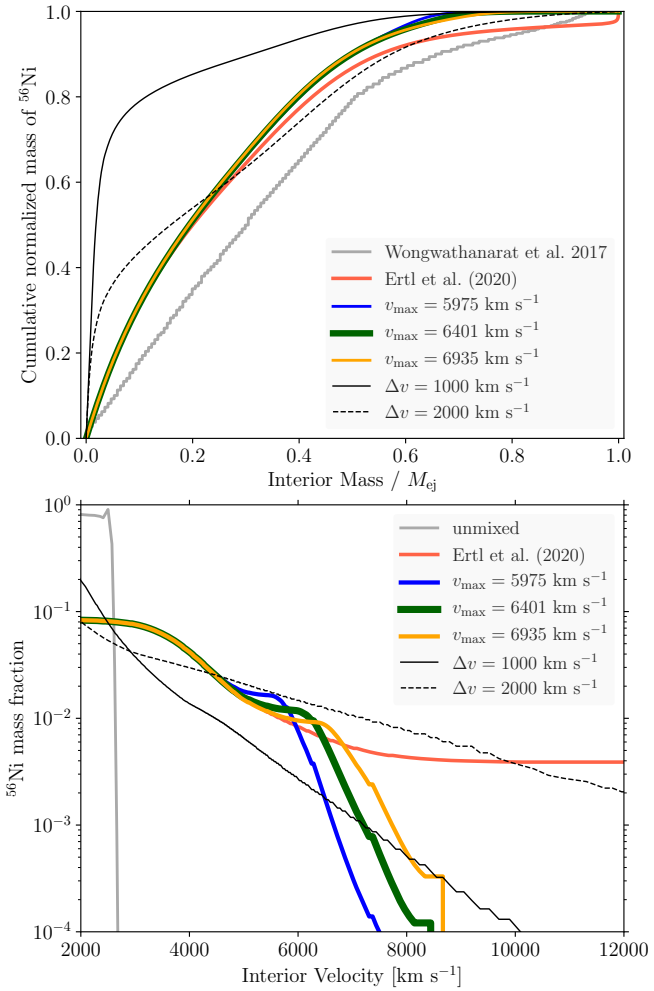

FIG. 1.— Mixing in Model He6.00. The top panel shows several possible prescriptions for the mixing of ^{56}Ni in mass compared with a multi-dimensional simulation of a Type IIb supernova with a similar helium core mass by Wongwathanarat et al. (2017, solid gray curve). Three of the prescriptions involve mixing to a maximum velocity using a moving boxcar method based on mass coordinate (blue, green, orange). Two others (solid and dashed black) invoke a similar mixing in velocity space as suggested by Dessart et al. (2015). The solid red line is the mixing used in the previous KEPLER study of light curves (Ertl et al. 2020). The thick dark green line labeled 6400 km s^{-1} is the standard mixing used in this paper. B and especially U magnitudes are very sensitive to the extent to which ^{56}Ni is mixed to high velocity. The bottom panel shows this same mixing plotted as a function of terminal velocity.

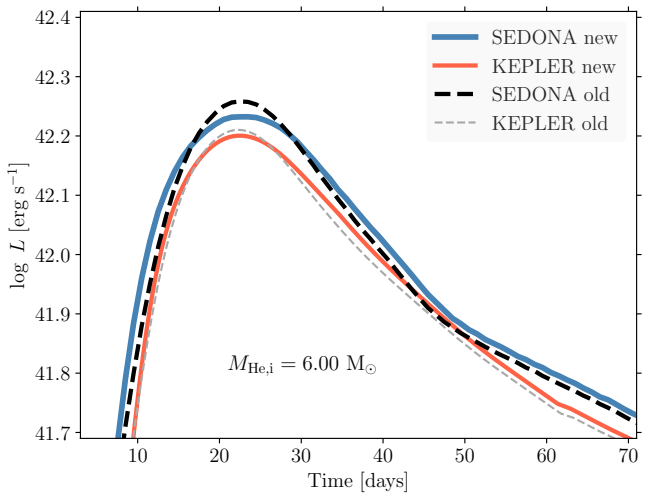

FIG. 2.— The effect of two mixing prescriptions on the light curve is shown for Model He6.00 calculated with two codes, KEPLER and SEDONA. The curves labeled "old" use the mixing defined in Ertl et al. (2020), including the unrealistic mixing of ^{56}Ni to arbitrarily high velocities. The "new" mixing is described in the text and Fig. 1. In both cases, the KEPLER and SEDONA calculations are in good agreement for the bolometric light curve. The difference at peak is about 9%.

greater speeds, a small amount of matter is mixed out to a value 30% greater. This formula would not describe mixing in a red or blue supergiant and is only for stripped helium stars.

This mixing is accomplished by the usual boxcar averaging technique. Two zones, n_1 and n_2 are determined that have velocities equal to v_{mix} and 1.3 v_{mix}. Two mixing masses (boxcar sizes) are taken to be $m_1 = 0.1M_{ej}$ and $m_2 = 0.02M_{ej}$. The boxcar m_1 is passed 7 times from the center of the star to zone n_1 and then the boxcar m_2 is passed 4 times from the center of the star to zone n_2. The results for three different choices for v_{mix} are shown for Model He6.00 in Fig. 1. The choice of 6400 km s^{-1} corresponds to the characteristic value in eq. (1).

Calculations using SEDONA show that neither the bolometric luminosity nor V magnitude at peak is very sensitive to the mixing prescription, but the B and especially U magnitudes are. Were the mixing assumed in Ertl et al. (2020) to be employed here, the colors of the supernova at peak, as characterized by $(B - V)$, would be too red compared with observations.

3. NORMAL TYPE IB AND IC SUPERNOVAE

It is first necessary to define just which observations and models will be considered "normal" Type Ib and Ic supernovae. We exclude any observed events displaying gross asymmetry, broad lines, or extreme energy (much greater than 2×10^{51} erg). Our observational sample will thus not include broad-lined Type Ic supernovae or gamma-ray burst supernovae. Present modeling does not support the hypothesis that these are non-rotating, neutrino-powered, radioactivity-illuminated explosions. The stars that uniformly collapse to black holes in our survey or pulsational pair-instability form a gross upper boundary mass to normal Type Ib and Ic supernovae. Stars that experience strong silicon flashes or produce very little ^{56}Ni form a lower one. Such stars exist, are abundant, and probably explode, but the early evolution of the typical Ib light curve excludes their inclusion in the "normal" sample. The width of the light curve also excludes additional models on the upper end. These cases are thus discussed separately in §4 and §5.

Applying these criteria, Ertl et al. (2020) claimed that normal Type Ib and Ic supernovae resulted from presupernova masses 2.7 to 5.6 M$_\odot$. For the standard mass loss rates this implied initial helium star masses from 3.3 to 8.0 M$_\odot$ (Table 1). For $f_{WR} = 1.5$, the corresponding initial helium star mass range increased to 3.7 to 13 M$_\odot$. This larger mass loss rate was actually preferred by Yoon (2017) and Woosley, Sukhbold, & Janka (2020). We will find later (§3.2) that the results, especially near peak, are most sensitive to the presupernova mass, not the initial mass and mass loss that was used to get there, so these

models with higher mass loss rates are included in our analysis, but not emphasized.

Here, in order to include what could potentially be a large number of lower mass explosions for which the silicon flash is not very strong, we extend the definition of ordinary Type Ib and Ic supernova to include smaller presupernova masses down to 2.2 $M_\odot$. For standard mass loss rates, this means we include initial helium core masses as low as 2.7 $M_\odot$. The new lower bound still excludes a few stars with still smaller masses that have substantial radius expansion even without a strong silicon flash (Woosley 2019) and make little ^{56}Ni, and models with such a strong flash that the light curve would be dominated by circumstellar shock interaction. The larger set thus continues to exclude Models He3.00 and He3.10 for which we have no explosion calculation from Ertl et al. (2020) that did not also experience a strong silicon flash. They also exclude He2.50 and He2.60 which made very little 56Ni (less than 0.02 $M_\odot$).

The flash in Model He3.20 was weak enough that the resulting light curve was dominated by radioactivity and not circumstellar interaction, so it is included. Table 1 lists the full range of models treated as normal Type Ib and Ic in the new survey.

When averages are to be calculated, two ranges will be considered: a high one, 3.3 - 8 $M_\odot$ consistent with Ertl et al. (2020), and a new low one that we now favor, 2.7 - 8.0 $M_\odot$ (excluding 3.1 and 3.2), which includes a substantial fraction of potentially observable low mass events. Obviously the inclusion of lower mass models will decrease the averages for ^{56}Ni produced, kinetic energy, luminosity, and ejected mass.

Except for Model He8.00x2, no new explosion models have been calculated, so all previous conclusions that depended only on stellar evolution and hydrodynamics and not on detailed radiation transport carry over from Ertl et al. (2020). That includes ejected masses, compositions, explosion kinetic energies, and ^{56}Ni production for individual supernovae (Table 1). These quantities are summarized for other central engines in Table 5 and Fig. 24 of Ertl et al. (2020). The greatest ^{56}Ni mass produced for the W18 parametrization was 0.135 $M_\odot$ (as upper limit, $3/4 \times M_{\rm NSE}$) in Model He7.13, which also had the greatest explosion energy, 1.70×10^{51} erg. (Table 1). When the more energetic S19.6 central engine was employed, the maximum ^{56}Ni production and explosion energy rose only slightly to 0.148 $M_\odot$ and 1.94×10^{51} erg (also for the 7.13 $M_\odot$ model).

3.1. *Bolometric Light Curves*

The peak bolometric luminosities and times for the standard models are given in Appendix B. All used the new prescription for mixing (§2.3). Also given in the tables are rise times ($t_{-1/2}$), decline times ($t_{+1/2}$), and decline rates (Δm_{15}) for the bolometric luminosity and similar information for the filtered luminosities. From this information one can approximately reconstruct any model light curve near its peak.

In Fig. 3, the light curves of typical models, He4.10 (based on a Salpeter IMF average of supernovae for models He2.70 to He8.00) and He4.60 (based on average between He3.30 and He8.00), are compared with the Carnegie sample of stripped-envelope supernovae (Taddia et al. 2018). Also given are the light curves of

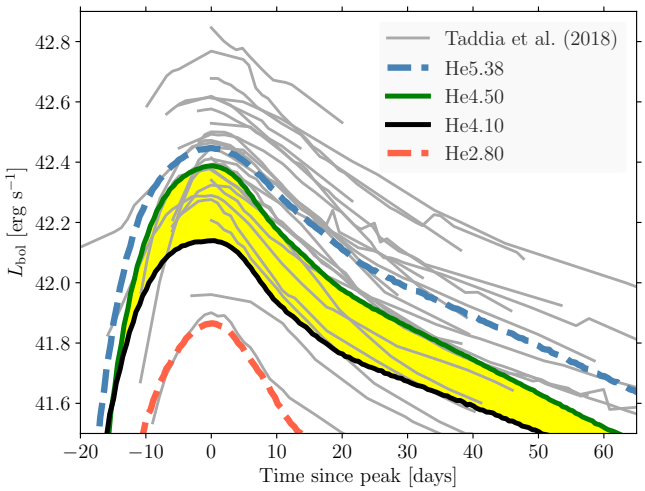

FIG. 3.— Bolometric light curves for the Carnegie sample of 32 Type Ib, Ic and IIb events (Taddia et al. 2018) compared with models. The dark black and green lines are Models He4.10 and He4.50 respectively. The yellow band bounded by these two models roughly represent the typical range of the survey. The red and blue dashed lines are our faintest (He2.80) and brightest (He5.38) ones. A substantial set of observed normal supernovae are brighter than the most luminous model. Fainter supernova pose a lesser problem since the ^{56}Ni masses used here are upper bounds (Table 1;§3.6.4).

the faintest (He2.80) and the most luminous models (He5.38). Other models would fill in the space between these two curves. The agreement with most of the observations, including the faintest, is encouraging. There is a substantial set though, perhaps as many as one-third of the observed events, for which the brightest models are just too faint. This is essentially the same dilemma noted by Ertl et al. (2020) restated with better calculations of radiation transport and new observations. Is a substantial fraction of the stripped supernovae called "normal" by the observers outside of the reach of standard models based on a neutrino-powered explosion and a radioactively illuminated light curve? For this model set, it seems so.

We also calculated the "quasi-bolometric" light curves of the same models for direct comparison with the tabulations of Prentice et al. (2019). This entailed integrating the SEDONA spectral histories assuming a complete measurement within the 4000 to 10000 Å wavelength range and no detection outside. Fig. 4 shows the comparison. When peak luminosity is plotted against rise time, the models rise too late and are too faint to explain the brightest events. Some of these bright events are Type Ic-BL supernovae and almost certainly involve other physics not included in this study. Two other events are unusual. SN 2013bb (off scale in Fig. 4) ejected a very large mass and is slowly moving. Its broad, faint light curve is better explained by a more massive model than the common events. The discussion of such events is deferred to §5. At the other other extreme, SN 2018ie is a faint, rapidly evolving, high velocity, high temperature event. This might have been a low mass explosion related to the fast blue transients discussed in §4.

A comparison that excludes these anomalous cases is given in the second panel of Fig. 4. Since more supernovae had their decay time measured than their rise time,

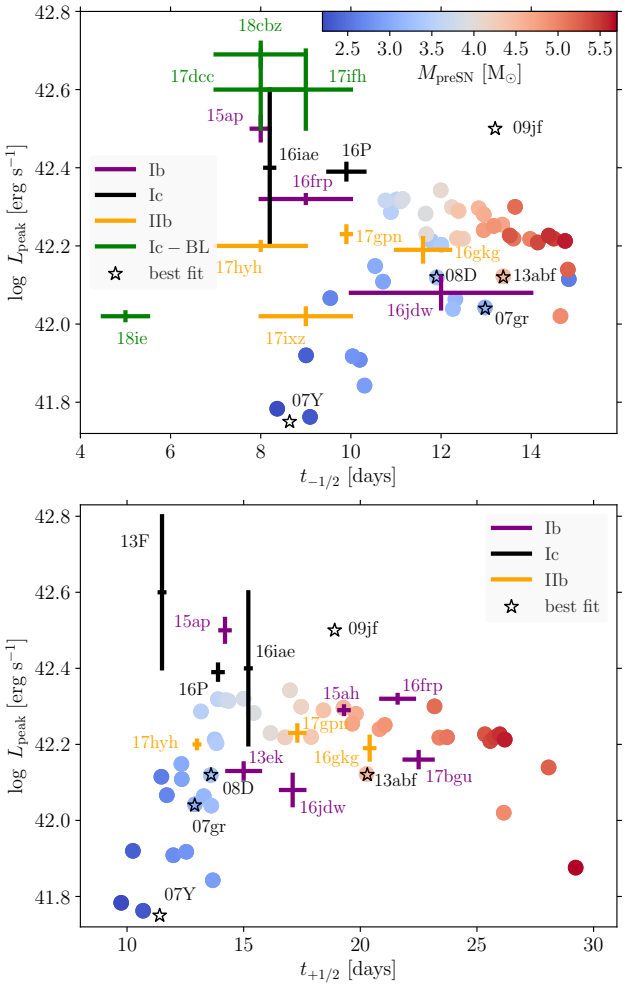

FIG. 4.— Peak luminosity in the 4000–10000 Å range vs time to rise to peak (top) or time to decline (bottom) for a baseline of 50% $L_{\rm peak}$. Filled circles are model results color coded by their presupernova mass while points with error bars are observations (Table 3 of Prentice et al. 2019). Five points indicated with asterisks, 07Y, 07gr, 09jf, 13abf, and 08D, are supernovae discussed in §3.6. The points are models that fit the observed light curves very well. In two cases, 09jf and 07Y, the ^{56}Ni abundance was adjusted to give these good fits (see Fig. 16 and Fig. 14). In the top panel, some outliers attributed by Prentice et al. (2019) to Type Ic-BL and a very low mass event (SN 2018ie) are included, while some supernovae that lacked data for $t_{-1/2}$ in the Prentice et al. table (SNe 2013F, 2013bb, 2013ek, 2015ah, and 2017bgu) are absent. In the bottom panel, the outliers are omitted and most of the previously missing supernovae now have data. The models predict a slightly longer rise to peak ($t_{-1/2}$) than these observations, but a comparable time to decay to 50% of peak luminosity ($t_{+1/2}$). For these observations, there is a deficiency of bright models with short time scales, but the observed luminosity of SN 2013F is uncertain.

there is slightly more data in this figure. The agreement is significantly improved. One outlier, SN 2013F, is a fast rising, very luminous supernova. The host galaxy extinction, $E(B-V)_{\rm host} = 1.4 \pm 0.2$ mag, is much larger than for any other supernova in the sample though and its colors are uncertain. Perhaps its luminosity might be correspondingly uncertain.

Prentice et al. (2019) also give median luminosities, time scales, and ejected masses for a larger set of several dozen supernovae with data extracted from several sources. All luminosities are only for the 4000 - 10000 Å range. Table 3 compares these median values to the IMF-averaged models of this paper for the two different assumptions about the progenitor mass range.

Now the agreement for all measured quantities is quite good. The median rise time is a day or so longer in the models and the decline time two days shorter. The sum, i.e., the light curve width agrees quite well. Even in the models, it is difficult to determine the exact time of peak to better than a day (more so in heavier models) because the luminosity varies so slowly there. Though the data is for a limited number of supernovae, the agreement is somewhat better than that of the same models with the Carnegie data set (Fig. 3, Taddia et al. 2018, see also Table 3). Perhaps it is only the statistics of small numbers and the definition of what constitutes a "normal" supernova. We see no obvious explanation for a discrepancy.

Many others have extracted average ejected masses, ^{56}Ni masses, and kinetic energies from surveys of Type Ib and Ic supernovae (Richardson et al. 2006; Drout et al. 2011; Cano 2013; Taddia et al. 2015; Lyman et al. 2016; Prentice et al. 2016; Taddia et al. 2018). For a summary table of these other results see Taddia et al. (2018). Most are consistent with Prentice et al. (2019), though often with larger error bars. Caution should be exercised when using the ^{56}Ni masses derived using Arnett's Rule, as some of these surveys did. These are usually overestimates (§A.2). Using numerical modeling, Taddia et al. (2018) concluded, for Type Ib and Ic respectively, that $M_{\rm ej} = 3.8 \pm 2.1$ and 2.1 ± 1.0 M$_\odot$; $E_{\rm exp} = 1.4 \pm 0.9$ and $1.2 \pm 0.7 \times 10^{51}$ erg; and $M_{\rm Ni} = 0.14 \pm 0.09$ and 0.13 ± 0.04 M$_\odot$.

Table 4 compares the IMF-averaged characteristics of the two model sets that used different mass loss rates ($f_{\rm WR} = 1$ and $f_{\rm WR} = 1.5$; Table 1). Unfortunately, no low mass explosions with $M_{\rm preSN}$ less than 3.43 M$_\odot$ were computed for $f_{\rm WR} = 1.5$ by Ertl et al. (2020), so one can only compare the averages for a limited range of masses whose boundaries do not reflect the full range of Type Ib and Ic progenitors. Table 4 should thus not be compared with surveys that do not select against low mass (typically low luminosity) events.

The use of a greater mass loss rate does not cause any major differences in the bulk characteristics of the supernovae. Even though the models to be averaged in Table 4 were selected on the basis of a common presupernova mass, 3.42 M$_\odot$ to 5.63 M$_\odot$ for $f_{\rm WR} = 1$ and 3.43 M$_\odot$ to 5.64 M$_\odot$ for $f_{\rm WR} = 1.5$, the average presupernova mass still differs by about 0.2 M$_\odot$ because the weighting factors in the averaging process depend on the estimated main sequence masses of the stars. The larger range of higher masses for $f_{\rm WR} = 1.5$ result in a more massive average. Even so, the ^{56}Ni masses and explosion energies are virtually identical. Because of the greater emphasis on more massive explosions, the ejected masses are a bit larger and that results in a slight lengthening of the time scales and decrease in the peak luminosity. From this limited study, one may conclude that the bulk characteristics of the supernovae are insensitive to the mass loss rate used to produce a given range of presupernova masses. This insensitivity does not carry over to the colors and spectra, however (§3.2).

Table 3. IMF Integrated Characteristics

	This work $2.70 \le M_{\rm He} \le 8.00$		This work $3.30 \le M_{\rm He} \le 8.0$		Ertl et al. (2020) $3.30 \le M_{\rm He} \le 8.00$		Observations Prentice et al. (2019)	
	median	mean	median	mean	median	mean	median Ib	median Ic
$M_{\rm preSN}$	3.22	3.41	3.57	3.77	3.57	3.77	—	—
$E_{\rm exp}$	0.77	0.89	1.26	1.06	1.26	1.06	—	—
$M_{\rm ej}$	1.70	1.87	1.98	2.19	1.98	2.19	$2.0^{+1.2}_{-0.9}$	$2.2^{+3.1}_{-0.9}$
$M_{\rm Ni}$	0.07	0.07	0.09	0.09	0.09	0.09	$0.07^{+.10}_{-.02}$	$0.09^{+.06}_{-.03}$
				Full Bolometric Luminosity				
$L_{\rm peak}$	42.21	42.20	42.32	42.27	42.30	42.25	—	—
$t_{-1/2}$	11.9	12.3	11.8	11.9	8.57	9.00	—	—
$t_{\rm peak}$	19.7	20.0	20.8	21.4	18.7	19.5	—	—
$t_{+1/2}$	15.1	15.9	15.6	17.6	15.3	17.3	—	—
				4000 – 10000 Å				
$L_{\rm peak}$	42.11	42.10	42.21	42.16	—	—	$42.2^{+0.4}_{-0.1}$	$42.3^{+0.3}_{-0.2}$
$t_{-1/2}$	11.0	11.1	11.9	11.9	—	—	$10.4^{+2.8}_{-1.7}$	$9.8^{+3.3}_{-3.1}$
$t_{\rm peak}$	20.0	20.3	21.2	21.6	—	—	—	—
$t_{+1/2}$	13.6	14.8	13.9	16.2	—	—	$17.0^{+4.7}_{-3.4}$	$17.5^{+7.1}_{-4.5}$

Note. — Observations are from Prentice et al. (2019). Type Ib is their "Ib +Ib(II)" sample and Ic is their "Ic-5/6/7" sample in their Tables 4–7. Note that observationally inferred ^{56}Ni masses are all based on Arnett's rule. Broad line supernovae are excluded. $E_{\rm exp}$ is in 10^{51} erg, masses are in $M_\odot$, and times are all in days. Luminosities are in log base 10, and all models had mass loss with $f_{\rm WR} = 1$.

Table 4. Dependence of Explosion Properties on Mass Loss

	$f_{\rm WR=1}$ $4.40 \le M_{\rm He} \le 8.00$ $3.42 \le M_{\rm preSN} \le 5.83$		$f_{\rm WR=1.5}$ $5.00 \le M_{\rm He} \le 13.0$ $3.41 \le M_{\rm preSN} \le 5.84$	
	median	mean	median	mean
$M_{\rm preSN}$	4.21	4.31	4.45	4.42
$E_{\rm exp}$	1.42	1.38	1.41	1.37
$M_{\rm ej}$	2.55	2.69	2.84	2.76
$M_{\rm Ni}$	0.11	0.11	0.11	0.11
		Bolometric Luminosity		
$L_{\rm peak}$	42.39	42.36	42.35	42.36
$t_{-1/2}$	12.6	12.7	11.9	12.1
$t_{\rm peak}$	22.0	22.7	21.0	21.8
$t_{+1/2}$	18.5	19.7	21.8	20.9

Note. — This table is only to illustrate the effect of using different mass loss rates to evolve the same limited range of presupernova masses. It is not to be compared with observations that generally will include lower mass supernovae. See Table 3 for averages over the full range. Masses are in $M_\odot$; explosion energy is in units of 10^{51} erg; luminosity is log base 10 of L in erg s^{-1}; and time is in days.

3.2. *Photometry*

Absolute magnitudes were computed by passing the SEDONA spectral histories through appropriate filters and using the prescribed zero points for various magnitude systems. In order to accommodate both convention and the data of several sets of observers, three different magnitude systems were used: Vega for Johnson–Cousins $UBVRI$, AB for SDSS $ugriz$, and "natural" for CSP $uBgVri$. All filters, and also zero points for Vega magnitudes, are given at `http://svo2.cab.inta-csic.es/svo/theory/fps3`. The zero points for the AB system was taken to be 3631 Jy. For natural magnitudes, they were calculated according to Krisciunas et al. (2017). Offsets at peak for a typical model are given in Table C1 in the Appendix. Unless otherwise stated, $UBVRI$ magnitudes in this paper are on the Vega scale and $ugriz$ magnitudes are on the AB scale. Exceptions are when models are compared with data exclusively from the Carnegie group. Then natural magnitudes are used.

The photometry and spectrum of a typical model calculated with SEDONA is shown in Fig. 5. As noted previously, He4.50 is close to the median presupernova mass, 4.6 $M_\odot$, that one calculates for an IMF-weighted distribution of helium cores in the mass range 3.3 to 8 using the equivalent ZAMS masses. The mean ejected mass, kinetic energy, and ^{56}Ni mass for the same model set (Table 3) are also close to those of Model He4.50 (Table 1). The spectrum in Fig. 5 has been color coded to show the wavelengths to which the $ugriz$ filters are most sensitive.

Fig. 6 shows that the bolometric light curve depends chiefly on the bulk properties of the supernova - ejected mass, kinetic energy, ^{56}Ni mass - and not much on the composition of the presupernova star. Models He4.50 with $f_{\rm WR} = 1$ and He8.00x2 with $f_{\rm WR} = 2$ end up ejecting similar masses with the kinetic energies (Table 1 and Table 2). They also eject, by design, the same masses of ^{56}Ni. It is then perhaps not too surprising that their luminosities at peak are very similar, $10^{42.39}$ erg s^{-1} at day 19.5 for He4.50 and $10^{42.37}$ erg s^{-1} at day 20.2 for He8.00x2. The spectrum and colors are different though, especially at early times (see also similar results by Yoon et al. 2019). The carbon-rich star (He8.00x2) is redder than the helium-rich star (He4.50). Even with large mass loss rates the surface is never devoid of helium (e.g. Woosley 2019) due to the recession of the helium convective core in the presence of mass loss, but Model He8.00x2 has a lot less total helium than He4.50. The helium, carbon, and oxygen masses in the two explosions are 0.13 $M_\odot$, 0.47 $M_\odot$, and 0.84 $M_\odot$ for He8.00x2, but 0.96 $M_\odot$, 0.13 $M_\odot$, and 0.41 $M_\odot$ for He4.50. The little

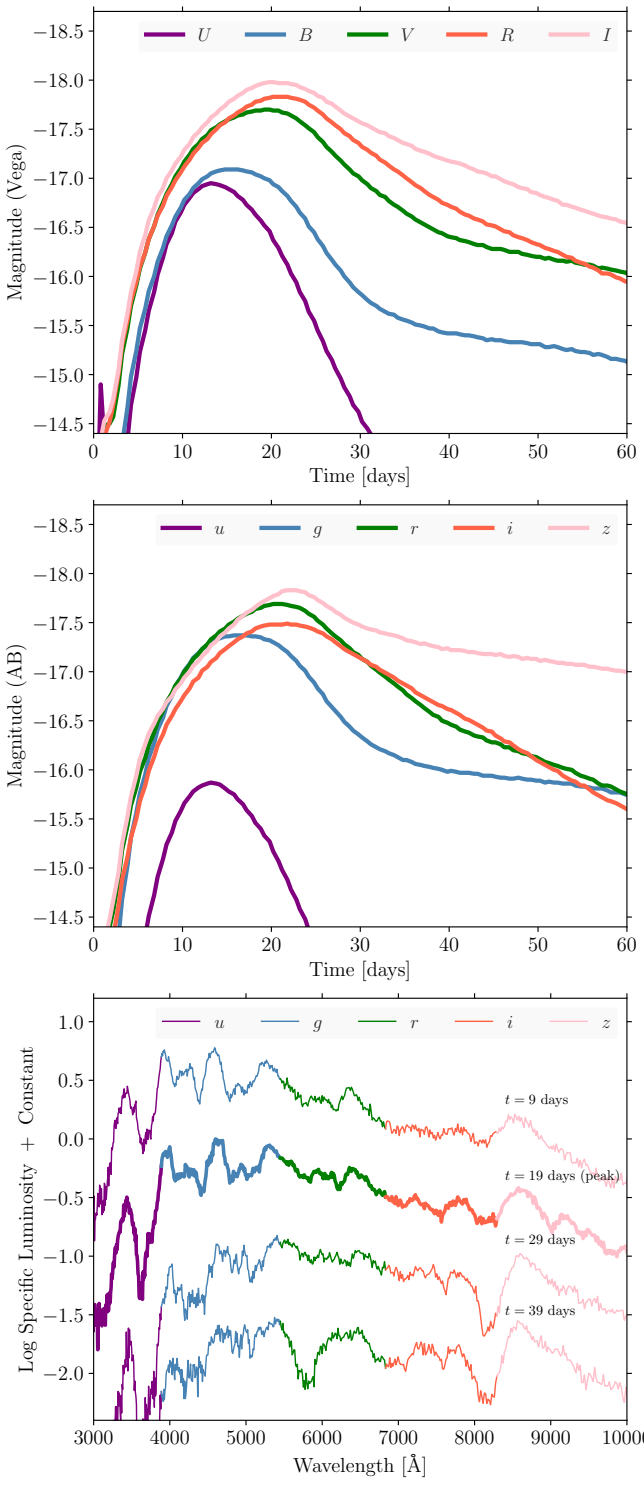

FIG. 5.— Multiband Light curves and spectra for Model He4.50 (Table 1), a typical Type Ib model in our study. The model ejected 1.90 $M_\odot$ with a kinetic energy of 1.28×10^{51} erg and synthesized 0.099 $M_\odot$ of ^{56}Ni. The peak bolometric luminosity was $10^{42.39}$ erg s^{-1}. (top:) *UBVRI* light curves are given as indicated for Vega-based zero points. (Middle:) Light curves in the *ugriz* wavebands based on an AB magnitude zero point. (Bottom:) The spectrum calculated using SEDONA at bolometric peak (19 d) and 10 days before and 10 and 20 days after. To facilitate comparison with the light curve, the spectrum has been color coded with the filters indicated corresponding to the wavelength range for AB-based magnitudes.

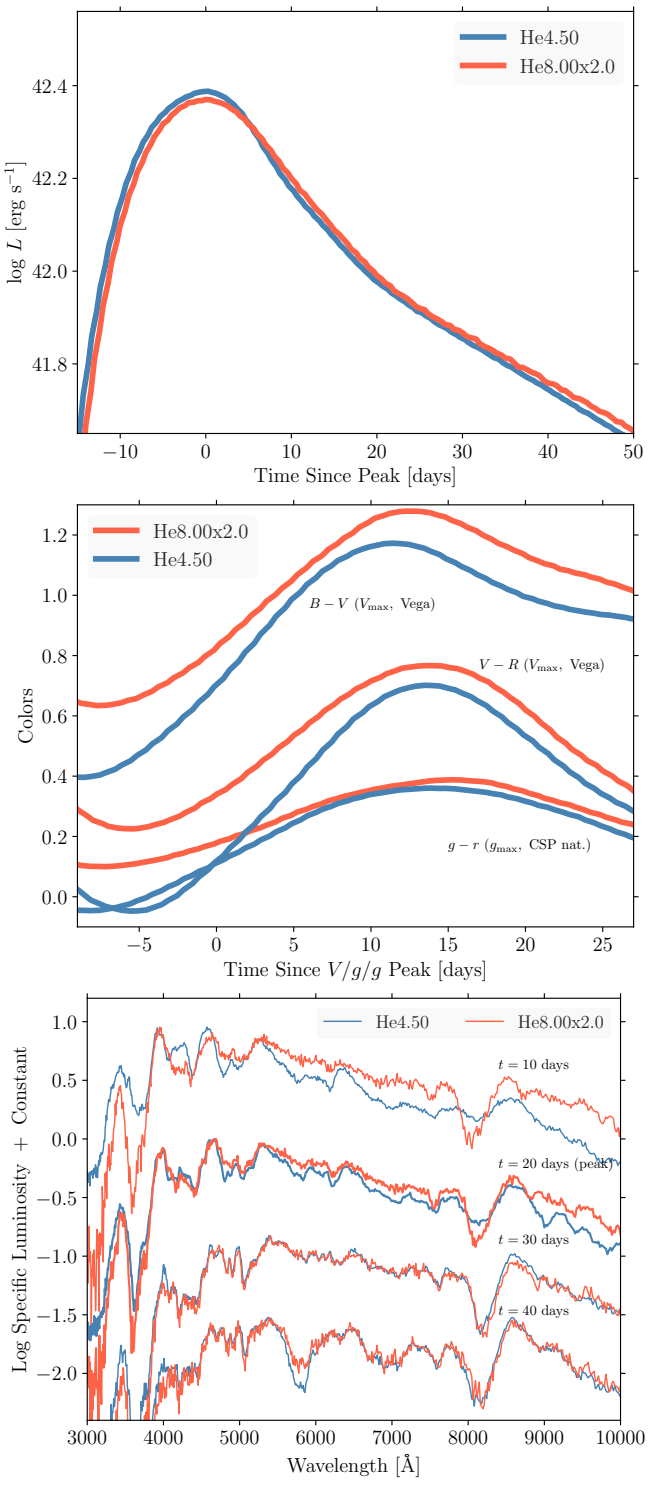

FIG. 6.— Bolometric light curve (top), color indices (middle) and spectrum (bottom) for Model He8.00x2 compared with Model He4.50. Both models had identical explosion energies and ^{56}Ni masses and similar ejecta masses. Model He8.00x2 was evolved from a larger mass star with a greater mass loss rate ($f_{\rm WR} = 2$) and thus lost almost all its helium before exploding. Model He4.50 on the other hand (Fig. 5) was helium-rich with about half of its ejected mass being ^{4}He. The carbon-rich Model He8.00x2 has a very similar bolometric light curve, but its colors are redder, especially at early times. The calcium infrared triplet is also stronger at earlier times in the carbon-rich model.

TABLE 5. IMF AVERAGED PEAK MAGNITUDES, TIMESCALES, AND COLORS

	median $f_{\rm WR}=1$	mean $f_{\rm WR}=1$	median $f_{\rm WR}=1.5$	mean $f_{\rm WR}=1.5$
$U_{\rm peak}$	-16.50	-16.42	-16.34	-16.47
$B_{\rm peak}$	-16.74	-16.60	-16.65	-16.54
$V_{\rm peak}$	-17.30	-17.22	-17.25	-17.13
$R_{\rm peak}$	-17.39	-17.37	-17.43	-17.29
$I_{\rm peak}$	-17.54	-17.52	-17.58	-17.45
$u_{\rm peak}$	-15.40	-15.33	-15.33	-15.39
$g_{\rm peak}$	-17.05	-16.89	-16.92	-16.82
$r_{\rm peak}$	-17.25	-17.22	-17.27	-17.14
$i_{\rm peak}$	-17.06	-17.06	-17.15	-16.99
$z_{\rm peak}$	-17.40	-17.36	-17.44	-17.28
$t_{-1/2,U}$	5.82	6.05	5.68	5.78
$t_{-1/2,B}$	8.03	8.47	8.23	9.10
$t_{-1/2,V}$	10.50	10.74	10.68	10.68
$t_{-1/2,R}$	11.64	11.76	11.66	11.68
$t_{-1/2,I}$	10.92	11.45	11.02	11.36
$t_{-1/2,u}$	5.64	6.09	5.55	5.48
$t_{-1/2,g}$	8.39	9.01	8.94	8.97
$t_{-1/2,r}$	11.36	11.57	11.51	11.45
$t_{-1/2,i}$	12.56	12.64	12.07	12.35
$t_{-1/2,z}$	11.22	11.40	11.64	11.37
$t_{\rm peak,U}$	13.82	13.52	13.43	12.65
$t_{\rm peak,B}$	16.03	16.22	15.82	16.15
$t_{\rm peak,V}$	19.34	19.82	19.28	19.82
$t_{\rm peak,R}$	21.38	21.74	21.33	21.57
$t_{\rm peak,I}$	20.35	21.27	20.41	21.38
$t_{\rm peak,u}$	13.49	13.25	13.29	12.43
$t_{\rm peak,g}$	16.83	17.20	16.34	17.43
$t_{\rm peak,r}$	21.20	21.45	20.84	21.28
$t_{\rm peak,i}$	22.83	22.88	22.02	22.51
$t_{\rm peak,z}$	22.87	22.37	22.97	22.38
$t_{+1/2,U}$	8.16	8.69	8.94	9.29
$t_{+1/2,B}$	10.38	10.92	10.94	11.13
$t_{+1/2,V}$	11.64	12.79	11.77	13.48
$t_{+1/2,R}$	13.21	14.09	13.66	15.06
$t_{+1/2,I}$	17.96	20.01	17.93	21.63
$t_{+1/2,u}$	7.56	8.13	8.12	8.64
$t_{+1/2,g}$	11.35	11.64	11.96	11.74
$t_{+1/2,r}$	12.33	13.32	12.75	14.34
$t_{+1/2,i}$	15.34	16.30	17.23	17.84
$t_{+1/2,z}$	37.06	40.45	37.69	45.21
$(V-R)_{t_{\rm peak,V+10d}}$	0.340	0.336	0.330	0.323
$(V-R)_{t_{\rm peak,R+10d}}$	0.360	0.349	0.361	0.345

NOTE. — $f_{\rm WR}=1$ averages were integrated between He2.70 and He8.00, and $f_{\rm WR}=1.5$ averages between He3.00 and He13.0. See text for details.

bit of helium in He8.00x2 is in the outer layers and is ejected with high velocity. Removing an electron from carbon or oxygen is easier than taking one from helium, so the matter remains ionized farther out for a longer time in Model He8.00x2. This sustains a photosphere with a larger radius and may be why He8.00x2 is redder at a given luminosity, especially at times so early that something like a photosphere still exists. Another factor that could potentially affect the color is the abundance of iron group elements at the photosphere, but the abundance of iron in the unmixed outer layers was the same (solar), and the mixing and iron-group synthesis was also the same in the two models. This is therefore not an important effect.

While the rest of the paper will focus on the results

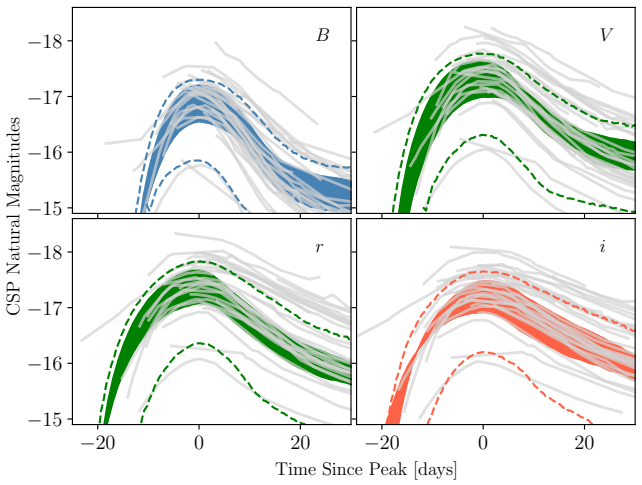

FIG. 7.— Photometry for the Carnegie sample of light curves for Type Ib, Ic and IIb light curves (gray curves Taddia et al. 2018; Stritzinger et al. 2018a, 2020) compared with models (colored curves). The dark band is bounded by Models He4.10 and He4.50, our typical explosions, and the dashed lines are for our faintest (He2.80) and brightest (He5.38) models using the standard W18 engine and mass loss ($f_{\rm WR}=1$). Both the data and model are given in CSP "natural" magnitudes. No correction has been made in the data set for host galaxy extinction.

using the standard mass loss rate, $f_{\rm WR}=1$, one should keep in mind these possible mass-loss-rate dependent variations in color indices. The mass loss rate used in He8.00x2, $f_{\rm WR}=2$, is probably an upper bound to the actual mass loss ate (Yoon 2017; Woosley, Sukhbold, & Janka 2020) so the variations shown in Fig. 6 may also be upper bounds.

Not all wavebands are treated equally well in SEDONA. U (and u) are probably the least accurate and will not be emphasized in this study. The U-band is more sensitive to iron-line blanketing compared to other bands and to the strength of the calcium H and K lines. That means the U-band is quite sensitive to the distribution of iron-group elements with velocity, hence to mixing. It is also sensitive to temperature and luminosity, since small changes in temperature can change the ionization state (e.g., the ratio of Fe III to Fe II) in some zones, which has a big effect on the line blanketing. Uncertainties due to non-LTE effects can also play a role. A small error in, say, the LTE computation of the ionization state may have a significant effect on the U-band while only a modest effect on on the R-band.

Uncertainties in the input atomic line data can also play a role. The calculations for the main models here used a large line list (§2.2). Calculations with a reduced set of 370,000 lines showed a modest increase in the ultraviolet brightness and blue magnitudes, but not much change for other filters.

IMF-averaged color characteristics are given in Table 5 for the mass range considered as typical for normal Type Ib and Ic supernovae. Compared with observations, the absolute magnitudes of our models in various filters agree quite well with the Carnegie tabulation for 34 Type Ib, Ic and IIb supernovae (Fig. 7). Since the data in Stritzinger et al. (2018a) and Stritzinger et al. (2020) are given in CSP natural magnitudes, model light curves were computed accordingly. The faintest observed curve in Fig. 7

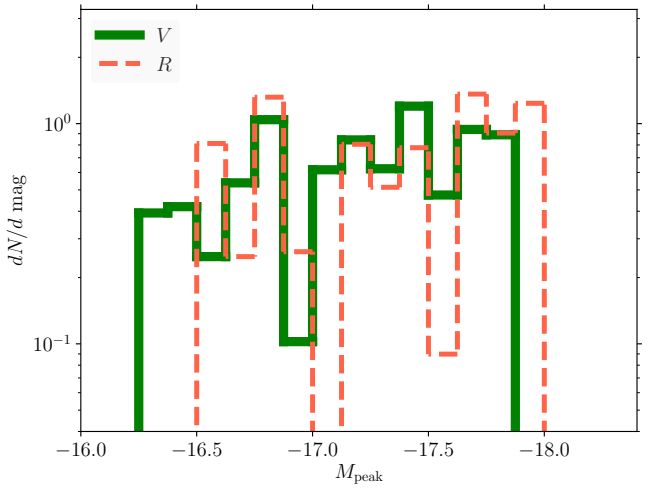

FIG. 8.— IMF averaged peak magnitude in the V and R bands for the standard model set with starting helium star masses from 2.7 to 8.0 $M_\odot$.

is SN 2007Y, a brief Type Ib supernova (Stritzinger et al. 2009, 2018a; Taddia et al. 2018). This supernova is treated in greater detail in §3.6.1. Explaining faint events generally poses no problems since the ^{56}Ni masses used here are upper bounds (Table 1).

3.3. *Peak Magnitude Distributions*

The distributions of peak magnitudes in V and R magnitudes are given for our model set in Fig. 8. These are averages calculated using a Salpeter IMF (Salpeter 1955) applied on the zero age main sequence mass distribution as described in Ertl et al. (2020). The time of maximum is defined for each color, i.e., the brightest V magnitude is evaluated at the time of V-band peak, not bolometric maximum. The brightest V magnitude for any of the standard models is −17.83. The brightest R magnitude is −17.99. This is for Model He5.38. Slightly brighter models exist for other choices of explosion energy and mass loss. For Model He5.25S, exploded with slightly more powerful S19.8 engine, the magnitudes at peak are $B = -17.48$, $V = -17.96$, and $R = -18.03$. For He5.00 with 1.5 times the standard mass loss (Table 1) and with W18 engine the peak magnitudes were $B = -17.52$, $V = -17.97$, and $R = -18.00$. Interestingly, the peak luminosities reach a maximum value around He5.00 to He6.00 and decline for heavier masses, especially above He8.00 (Table B1). This is because the ^{56}Ni masses cease rising (Table 1), but the slower expansion results in later peak times, more ^{56}Ni decay before peak, and thus lower luminosities. Our distribution of peak brightnesses is not being influenced on the upper end by the neglect of more massive models, at least for the neutrino-transport models considered here.

These distributions agree reasonably well with observations for about 2/3 of the ordinary Type Ib and Ic supernovae given in Fig 19 of Drout et al. (2011) which have been corrected for host galaxy extinction. Fainter, briefer events could come from lower mass stars (§4) and fainter broader events from higher mass ones (§5). Fainter values for peak magnitude could also be obtained by acceptable downwards adjustments of the ^{56}Ni yield in any of our models. The distributions in Fig. 8 lack, however, the brighter events in the observed distribution of Drout et al. (2011), even after broad-lined Type Ic supernovae are removed and we see no obvious reason for the discrepancy. A comparison with the more recent data of Taddia et al. (2018, see their Fig 8 and Fig. 3 here) shows somewhat better agreement and some support for a cut off around $V = -18$.

3.4. *Color Indices*

Fig. 9 shows the evolution of several frequently used color indices for the standard model set. The first three days of the explosion are not plotted because the KEPLER model is linked to SEDONA on day one, after homologous expansion has become a good approximation, and it takes another day or so for the radiation transport to adjust to the new code. The evolution near and shortly after peak has been best studied observationally and there is considerable interest in "pinches" in the various color indices about 10 days post-maximum (Drout et al. 2011; Taddia et al. 2015; Stritzinger et al. 2018b) since they might be used to estimate reddening.

Model results for $(B-V)$, $(g-r)$, $(g-i)$, and $(V-r)$ are plotted in CSP natural magnitudes and compared, at 10 days post-peak of V or g, with measurements by Stritzinger et al. (2018b). Model results for $(V-R)$ and $(V-I)$ are given in Johnson-Cousins Vega magnitudes and are compared, for $(V-R)$, with data from Drout et al. (2011). Approximate offsets for other magnitude systems are given in Table C1 and are less than 0.1 magnitudes. All data has been de-reddened and reflects the intrinsic values at the host. Model results for $(V-I)$ have previously been published by Dessart et al. (2015). Overall the agreement between observations and the models at 10 days post-peak in Fig. 9 is reasonably good, though there is a tendency for the models to be a little too red at early times and far too blue at very late times. Compare our model curves with, for example, the intrinsic color templates in Fig. 9 of Stritzinger et al. (2018b).

There are several reasons for the disparity. One is an inherent uncertainty in the time of maximum light in the various bands. The visual brightness is slowly varying in the models near maximum with a typical full width at 97% maximum of about 6 days. Small changes in the spectrum would affect our estimated time of visual maximum appreciably and the observed dates of maximum brightness might also not be precise. At the same time, the color indices are rapidly evolving. An offset of 3 days would significantly affect the comparison between the models and observations. The model colors are also intrinsically sensitive to mixing, ^{56}Ni production (Fig. 10), the LTE approximation used in our studies, and the geometry of the explosion. Less line blanketing in the outer layers would make the model bluer near peak. Greater ionization in the outer layers, possibly due to non-LTE effects at late times, would make them redder.

Larger values for the color indices in Fig. 9 are indicative of cooler emission, so a positive slope indicates a time when the supernova is becoming redder. Abrupt changes of slope in a color index reflect evolving physical circumstances in the supernova. During the first several days (not shown), the color evolves sharply to the red as shock deposited energy diffuses out of the expanding outer lay-

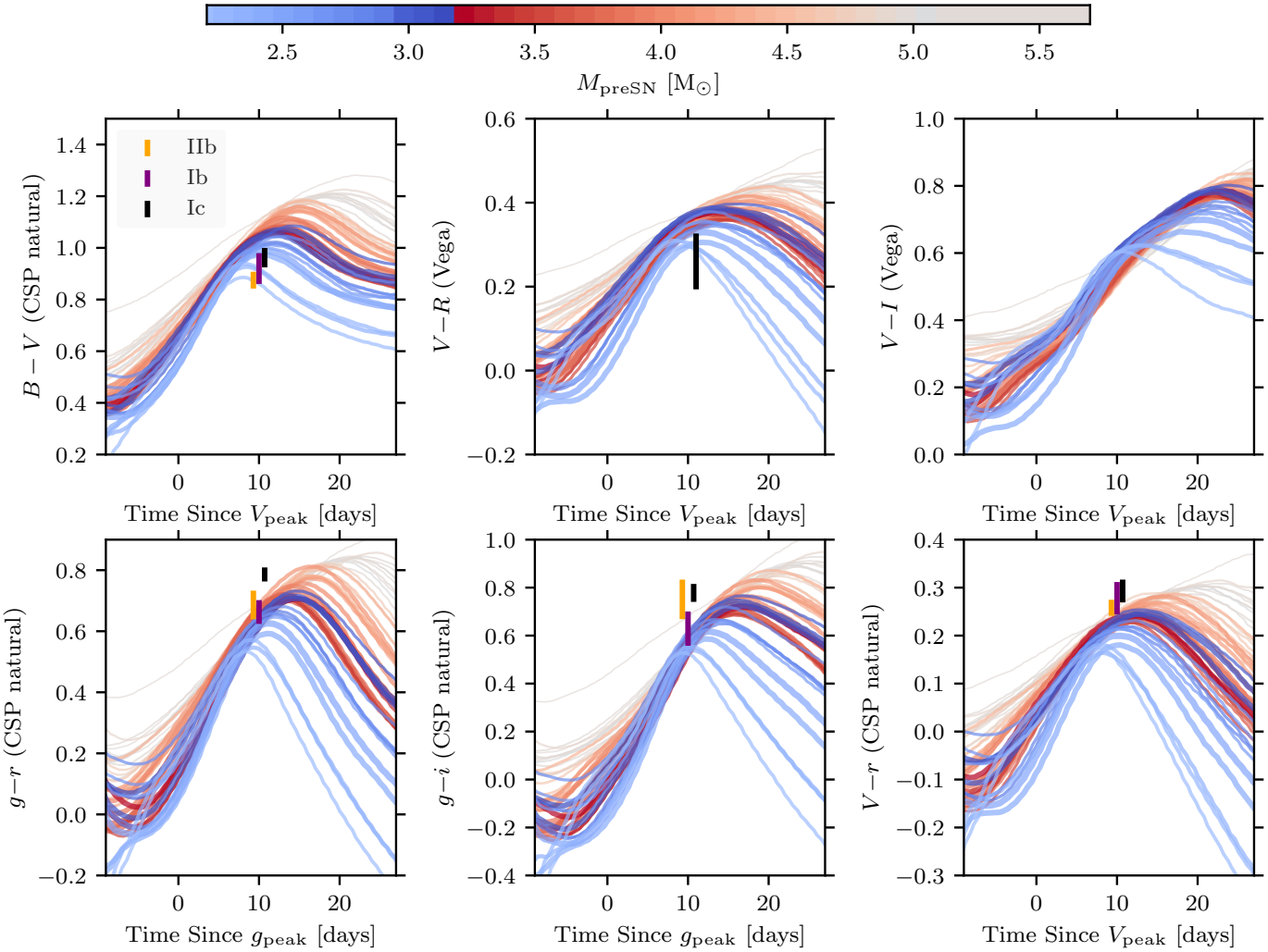

FIG. 9.— Color indices as a function of time for the standard model set. The model lines, color coded according to the presupernova mass, are for Models He2.70 through He8.00. The most common model has a presupernova mass of 3.22 $M_\odot$(Table 3). More massive models are colored red, and less massive ones are blue, with a line weight that declines farther away from this median. Data points at 10 days post-peak are from Stritzinger et al. (2018b), with separate lines for Type IIb, Ib and Ic (left to right) for $(B-V)$, $(g-r)$, $(g-i)$, and $(V-r)$. These data points are all in CSP natural magnitudes. Some of the data at 10 days have been offset slightly for clarity of display. The single data point for $(V-R)$ is from Drout et al. (2011), given in Vega magnitudes. The models themselves are computed in CSP natural magnitudes except for (B-V) and (V-I) which are based on Johnson-Cousins filters in Vega zeropoint. See Table C1 for approximate offsets. Note the "pinches" that occur in many color indices at about 10 days post maximum. For the purpose of presentation the model curves have been smoothed through a second order Savitzky–Golay filter.

ers. The luminosity declines or is nearly constant while the photospheric radius increases. Helium recombines at about 10000 K and a recombination front starts to move inwards in mass while still moving outwards in radius. This brief phase was not accurately captured in the SEDONA calculations and is not plotted, but is clearly seen in the KEPLER light curves and effective temperatures.

Once the outward moving diffusion front carrying energy from radioactive decay reaches the photosphere, the luminosity rises rapidly while the radius continues a slow increase. The combination causes the color to become blue and this is the cause of the first downward sloping part seen near the origin in some of the color index plots.

Shortly before peak, the luminosity rises more slowly while the radius rapidly increases. The color thus begins a long gradual ascent into the red that is prominent in all the panels of Fig. 9. By maximum luminosity roughly half the supernova has recombined. The photospheric radius is still increasing though and, as the luminosity declines, the reddening of the color indices continues. Other effects also come into play and the idea of a well-defined photosphere with a color governed by recombination like in a Type IIp supernova is increasingly overly simplistic. The opacity is not just due to electrons, but to lines that are sensitive to the ionization state and generally more important at lower temperature. The deeper the photosphere, the more heavy elements lie outside it, especially in mixed models, and this line blanketing also drives the color to the red.

About 10 to 20 days after maximum luminosity, with the longer time scale being appropriate to the more massive cases with longer diffusion times and larger fractions of carbon and oxygen, recombination reaches the center of the explosion and the photospheric phase ends. The concept of a photosphere is only an approximation anyway since different wavelengths originate from different

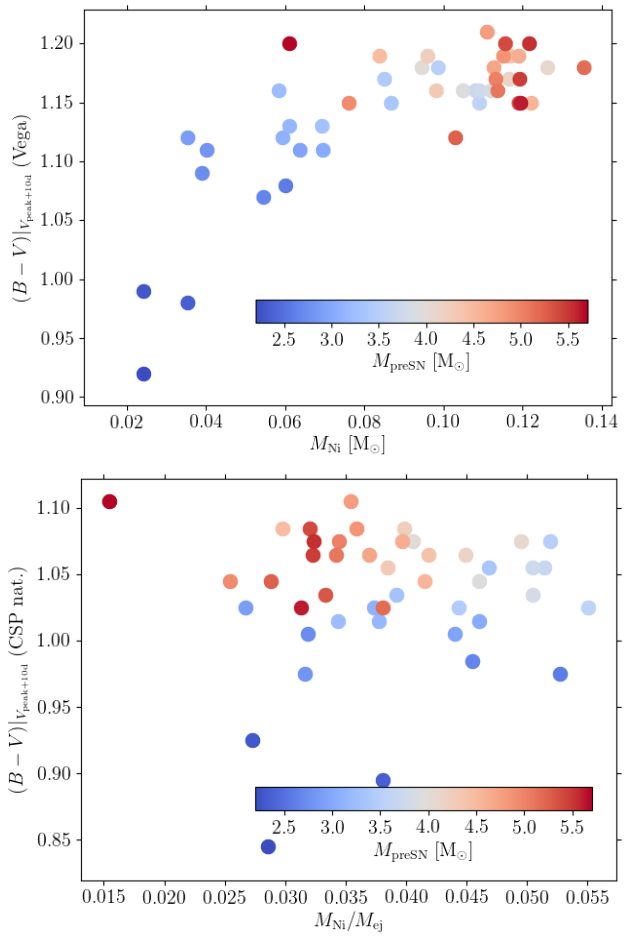

FIG. 10.— $(B-V)$ at 10 days post $V_{\rm max}$ vs ^{56}Ni mass ejected (top) and $M_{\rm Ni}/M_{\rm ej}$ (bottom). More ^{56}Ni makes the supernova brighter which tends to make it bluer at a given epoch, but more ^{56}Ni mixed to large radius also increases line blanketing and maintains a larger photospheric radius. The overall effect at 10 days after peak is to redden the supernova. The bottom panel compares favorably with Fig. 8b of Stritzinger et al. (2018b), especially if the three very low mass models are ignored, although the range of $M_{\rm Ni}/M_{\rm ej}$ sampled here is much smaller.

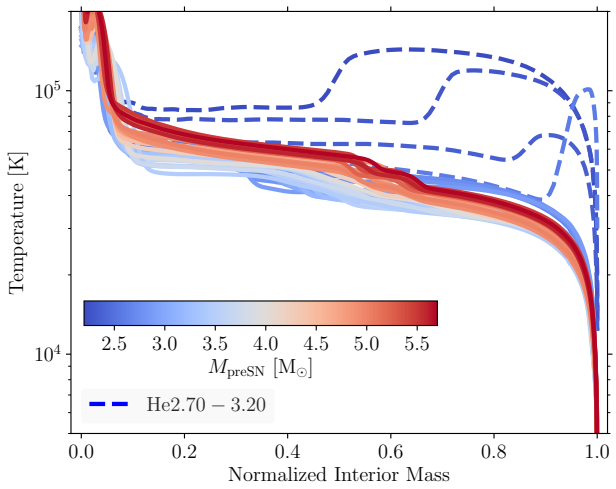

FIG. 11.— Interior temperature for the initial models calculated by KEPLER one day after core collapse. The shock has exited the supernova and the ejected matter has commenced a stage of homologous expansion, except for the lightest inflated models (dashed). For nearly the entire range of masses considered in the survey the temperature profile, normalized to the mass of the ejecta, is nearly a constant. Subsequent deposition of energy from radioactive decay will cause large deviations from the $T \propto 1/t$ behavior expected for adiabatic expansion in a gas dominated by radiation entropy.

depths and recombination is never complete, but from this point on, the supernova is increasingly just a cloud of ashes pumped by radiative decay. The power deposited by this decay (that which is not escaping) balances the luminosity. This is the onset of the nebular stage, though the full transition will take some time. Colors after this point vary according to the lines present in the filter, the mass of ^{56}Ni, and the density. The LTE model becomes an increasingly poor approximation. Among other things, it underestimates the ionization in a radioactively energized plasma. Underestimating the ionization means one sees to a deeper depth and hotter matter. For these reasons, the colors of our models are increasingly unreliable more than 20 days after peak luminosity.

As previously noted (Drout et al. 2011; Dessart et al. 2015; Stritzinger et al. 2018b), a "pinch" is seen in the distribution of colors measured in many wavebands about 10 days after peak. This reflects the regularity of the model set selected as Type Ib and Ic candidates and basic physics. The ratio of explosion energy to ejected mass and the ^{56}Ni mass do not vary greatly in the standard set (Table 1). One day after the explosion, all the models, except a few low mass ones with presupernova radius expansion, have a similar distribution of internal temperature (Fig. 11). The entropy in most of the ejecta at this time is about half due to radiation; the other half is electrons and ions. For adiabatic expansion, temperature thus declines more slowly than (radius)$^{-1}$, and hence slower that 1/t. This common thermodynamic configuration means that the light curves for the models without radius expansion will be quite similar during the first week. Nevertheless, the high density cores of all models would be fully recombined by 10 days after the explosion, well before peak, were it not for radioactive decay.

Helium recombines at ∼10,000 K. Carbon and oxygen combine with their last electrons at a lower temperature, typically ∼5000 K. For a blackbody, these two temperatures correspond to $(B-V) = 0$ and 1 which is very roughly the range of $(B-V)$ in Fig. 9. These are approximate values because of the variable density, the non-uniformity of the temperature, and gradients in the composition after mixing, but for temperatures cooler than about 5000 K, the supernova is effectively recombined. Prior to recombination, the photosphere continues to move out in radius, forcing the color to the red. This is the epoch corresponding to the well-defined upward slopes in Fig. 9. The lower mass models have faster expansion speeds in their deep interiors and greater helium fractions. They experience recombination earlier, so their color-index curves (e.g., for $B-V$) are steeper. These differences in slope result in a convergence, a "pinching" of the distribution as time passes. The convergence is truncated when the supernova recombines. After that the sudden collapse of the photosphere sends things to the blue, though what happens later is not well determined in the present study.

As Fig. 9 shows, there is observational evidence for

these pinches. Drout et al. (2011) have found a convergence of $(V-R)$ evaluated 10 days after V-band maximum. For their "gold" set of well-studied Type Ib and Ic supernovae, $(V-R)_{10\ \mathrm{days}} = 0.26 \pm 0.06$ mag. In a study similar to ours, Dessart et al. (2016) found a similar convergence, but with a value 0.33 ± 0.035 magnitudes, if they removed two high energy outliers. Stritzinger et al. (2018b) also observed similar pinches in a number of different filters, especially $(V-r)$. These are shown as vertical error bars on the plot and agree reasonably well with the models.

It is encouraging that four studies, two observational and two theoretical agree on $(V-R)$ at 10 days. As Dessart et al. (2016) note, weaker mixing favors higher temperatures in the inner ejecta, causing redder colors early on, but bluer colors around maximum (see also Dessart et al. 2012), so this color index might be useful for constraining mixing. As discussed by Drout et al. (2011) and Stritzinger et al. (2018b), the narrow range of several color indices in Fig. 9 might also be useful for better estimating the host galaxy extinction.

Fig. 12 shows the time-dependent color indices for the Carnegie collection of of 34 stripped supernovae (Stritzinger et al. 2018a). Here both data and models have been displayed in the "natural" magnitudes in which they were measured. The agreement for $(B-V)$ is quite good. Both the average supernova models (between He4.10 and He4.50) and the band defined by the brightest and faintest models show near congruence with the observations. Interestingly the narrowing in $(B-V)$ for the models at 10 days post-peak is more pronounced than in the observations. Typical error bars on the observations are 0.03 magnitudes.

The agreement is not as good for $(V-r)$ and $(V-i)$ showing again that our models emit inadequate radiation above about 5500 Å at late times. See also the spectroscopic comparisons to individual supernovae in §3.5. This could be due to the LTE approximation used in the models. Inadequate blue radiation is being processed into the red. The photosphere is collapsing and becoming quasi-nebular prematurely.

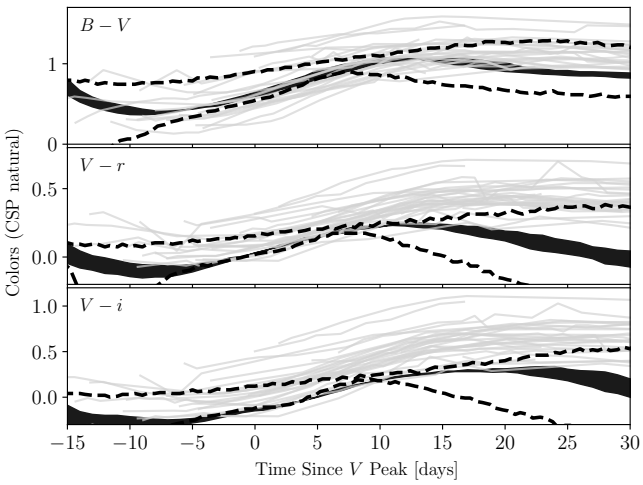

FIG. 12.— Color indices from the Carnegie sample compared with the models of this paper. Stritzinger et al. (2018a) recommend the interval from 0 to 20 days as most reliable. While the agreement with $(B-V)$ is good, the models are too faint in the i-band by about 0.3 magnitudes. As in Fig. 7, our model colors have been computed in CSP natural magnitudes to directly compare with the data. No host galaxy extinction is included. The dark solid curve is the range between our standard models He4.10 and He4.50. The brightest and faintest events have similar color histories to these typical models and are not plotted here. Instead, we show as dashed lines the lowest (He2.70) and highest ejecta mass (He8.00) models. The higher mass models, though rarer in nature, resemble the data for $(V-r)$ and $(V-i)$ better.

3.5. *Spectra*

Fig. 13 shows the spectra for our models. Similar to Shivvers et al. (2019), the spectra within 10 days of peak are rather uniform, similar to the uniformity in colors in Fig. 9. This is especially true if the very light and very heavy models, those with initial masses over 7 $M_\odot$ and below 2.9 $M_\odot$ are excluded from the sample. The lighter models have experienced radius expansion and are unusual because of it. The heavier models are fainter, rarer, and may be unusually red. The differences that exist in the models are mostly in the ultraviolet short of 4000 Å where there is a deficiency in emission, perhaps due to line blanketing. This same deficiency is also seen in the similar (but non-LTE) models of Dessart et al. (2015). The 5880 Å line of He I here is not particularly strong, even 10 days post-maximum, suggesting that all of these supernovae could be identified as Type Ic. Helium is certainly present in the models, ranging from 83% of the ejected mass in He2.90 to 21% in He8.00. Probably the weak line reflects the use of the LTE approximation which does a poor job of reproducing the level populations in a mixture of ^{4}He irradiated by the radiation from ^{56}Ni decay (Lucy 1991; Dessart et al. 2012; Woosley & Eastman 1997). Other line identifications can be made by comparison with Fig. 9 of Shivvers et al. (2019) and Fig. 14 of Dessart et al. (2015). The O I 7740 Å line is apparent, but not strong, and the 6200 Å line may be due to Si II. No hydrogen was included in the present study.

3.6. *Comparison with Observations*

To illustrate the strengths and shortcomings of our models and to gain a better perspective on their differences in peak luminosity, five models were compared with five well-analyzed Type Ib and Ic supernovae. The events chosen were selected by observers (see "Acknowledgments") to be representative cases. No effort was made to seek out the observations with which we agreed best. The five cases span a range of luminosities from very faint (SN 2007Y) to quite bright (SN 2009jf) and low mass to high mass. They include two events with double peaks (LSQ13abf and SN 2008D) and one low mass Type Ic event (SN 2007gr).

Spectra from the UV to the near IR for the 100 days following explosion were calculated for all models using SEDONA and photometry was obtained by numerically passing those spectra through various filters. As discussed in §3.4, the supernova undergoes a major adjustment about 20 to 30 days after the explosion (Fig. 9) when it ceases to be substantially ionized. In reality, gamma-rays from radioactive decay may keep the gas at least partly ionized longer than calculated in SEDONA, which assumes thermal equilibrium. This may have the effect of maintaining something resembling a photosphere for a longer time and make the supernova generally red-

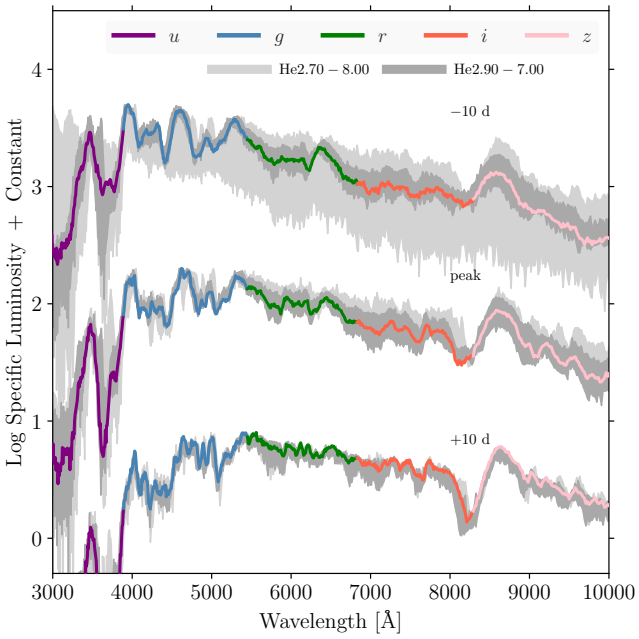

FIG. 13.— Spectra for our models. For a subset of models spanning the lowest and highest masses, spectra are presented at the time of peak luminosity and 10 days before and after. The light gray range is bounded by Models He2.70 and He8.00, while the darker gray range spans between Models He2.90 and He7.00. A typical model, He4.10, is highlighted as a colored line. Except at low and high mass, the the models display little diversity, especially 10 days after peak.

der than calculated here. We thus trust the SEDONA calculations of spectrum and photometry only to about 20 - 30 days past peak, or about 50 days after the explosion.

3.6.1. *SN 2007Y*

Table 6 and Fig. 14 show the comparison between Model He3.40 and Type Ib SN 2007Y (Stritzinger et al. 2009). The bolometric light curve for Fig. 14 is taken from Taddia et al. (2018). Apparent magnitudes given at `https://csp.obs.carnegiescience.edu/data/` were converted to absolute magnitudes using the offsets at peak provided in Tables 4 and 5 of Taddia et al. (2018). Typical error bars at peak in the absolute magnitudes are 0.37 magnitudes, dominated by the uncertain distance. SN 2007Y is one of the faintest Type Ib supernovae ever studied (Fig. 3).

Model He3.40 had a presupernova mass of 2.74 $M_\odot$ and ejected 1.2 $M_\odot$ with a kinetic energy of 4.0×10^{50} erg. These values are consistent with previous estimates based on model light curves, and spectral analysis, all of which suggest that SN 2007Y was a low-mass, low-energy event that produced less than typical ^{56}Ni (Table 6). Based on its late-time spectrum, Stritzinger et al. (2009) estimated 0.44 $M_\odot$ of ejecta moving slower than 4500 km s^{-1}, of which $\sim$ 0.20 $M_\odot$ was oxygen. Model He3.40 has 0.55 $M_\odot$ moving slower than 4500 km s^{-1}, of which 0.13 $M_\odot$ was oxygen. Total oxygen in the ejecta is 0.15 $M_\odot$. All in all, the model is similar to the 3.30 $M_\odot$ helium star suggested as a prototype for SN 2007 by Stritzinger et al. (2009), although the presupernova mass here is more like the 5.0 $M_\odot$ model of Woosley et al. (1995).

Fig. 14 shows the light curve of Model He3.40 compared with observations. The unmodified model is too bright. Since our ^{56}Ni yield is an upper bound (Table 1; Ertl et al. 2020), we are at liberty to use a smaller value while maintaining the overall composition and dynamical structure of the standard case. Consequently, we also calculated for comparison a version of Model He3.40 with 0.025 $M_\odot$ of ^{56}Ni instead of 0.039 $M_\odot$ (Table 6). The agreement with both the bolometric luminosity and the color magnitudes is greatly improved.

The calcium infrared triplet at around 8500 – 8600 Åis poorly modeled. By default, the Sedona calculations treat all lines as purely absorbing. This is a reasonable approximation for modeling the pseudo-continuum of weaker lines from complex iron group species; after a photon excites an iron ion, fluorescence will redistribute the energy in cascades across numerous lines. For strong transitions in simple ions like the Ca II triplet, however, there are few fluorescence channels, and the interaction is better modeled as purely scattering. Sedona has the option to adjust epsilon, the ratio of absorptive to absorptive plus scattering opacity, for each element individually (Kasen 2006). In the third panel of Fig. 14, the curve labeled "$\epsilon_{\rm Ca} = 0$" is a case for which the lines of calcium, and only calcium were treated as purely scattering. This resulted in substantial improvement with the observed spectrum. The overall photometry was not greatly affected by this change however.

Another major discrepancy in the +12 day spectrum of SN 2007Y, is the lack of strong features at 4900, 5800, 6600, and 6900 Å. The latter three are probably lines of He I not replicated correctly in our LTE study (Shivvers et al. 2019).

A degeneracy in the models should be noted. An almost identically good fit, including good spectroscopic agreement, could be obtained using the Model He3.60 or Mode He2.90. Getting the characteristics at peak right largely depends on the use of an appropriate ^{56}Ni mass, and the mapping between ^{56}Ni and presupernova mass is not monotonic (Table 1). Similarly, the time of bolometric peak which sets the light curve width, only varies by 3 days for the He2.90, He3.40, and He3.60 models.

3.6.2. *SN 2007gr*

SN 2007gr is one of the closest stripped-envelope supernovae ever discovered. Measurements by Valenti et al. (2008) gave an absolute R-band magnitude, at maximum, of −17.3, an estimated ^{56}Ni mass of 0.07 - 0.1 $M_\odot$, and showed compelling evidence for carbon in the spectrum. Later measurements (Table 6) gave similar characteristics. Maund & Ramirez-Ruiz (2016) estimate that the progenitor of SN 2007gr was $M_{\rm ZAMS} \sim 30$ $M_\odot$.

Here we take for comparison the unmodified Model He3.90 with characteristics given in Table 1 and Table 6. For the standard mass loss rate, $f_{\rm WR=1}$, the main sequence progenitor of this model would have been 18 $M_\odot$, though larger progenitors could be easily tolerated if the mass loss rate were greater. The important quantity again is the presupernova mass, 3.09 $M_\odot$. The comparison is given in Fig. 15. Digitized photometry and spectra were provided by Simon Prentice and were corrected for redshift, reddening, and extinction. Photometric data is from Hunter et al. (2009) and spectra are from Valenti et al. (2008) and Modjaz et al. (2014). Magnitudes for

Table 6. Supernova Observations and Models

	$t_{\rm peak}$ [day]	log $L_{\rm peak}$ [erg s^{-1}]	$M_{\rm ej}$ [M$_\odot$]	$E_{\rm exp}$ [10^{51} erg]	$M_{\rm Ni}$ [M$_\odot$]
			SN 2007Y		
Str09	18	42.1	···	~ 0.3	0.06
Lym16	> 13.6	42.00	$1.4^{+1.3}_{-0.4}$	$0.7^{+0.7}_{-0.3}$	$0.04^{+0.01}_{-0}$
Pre16	18.8	$42.01^{+0.10}_{-0.12}$	···	···	$0.051^{+0.015}_{-0.013}$
Tad18	18	41.90	1.9	0.6	0.03
He3.40	19.5	42.01	1.20	0.40	0.039
He3.40Ni	17.5	41.85	1.20	0.40	0.025
			SN 2007gr		
Hun09	~ 14	42.24	2.0 - 3.5	1 – 4	0.076±0.02
Lym16	> 13.5	42.28	$1.8^{+0.6}_{-0.4}$	$1.1^{+0.5}_{-0.4}$	$0.08^{+0.01}_{-0.01}$
Pre16	13.1	$42.30^{+0.10}_{-0.08}$	···	···	$0.073^{+0.020}_{-0.013}$
He3.90	22	42.15	1.59	0.59	0.059
			SN 2009jf		
Val11	~ 22	42.62	5 – 7	5 – 10	0.23±0.02
Sah11	19±1	$42.48^{+0.08}_{-0.05}$	4 – 9	3 – 8	0.17±0.03
Lym16	> 20.5	42.60	$4.7^{+1.7}_{-1.1}$	$2.5^{+2.2}_{-0.9}$	$0.24^{+0.03}_{-0.02}$
Pre16	21.3	$42.68^{+0.07}_{-0.06}$	···	···	$0.271^{+0.051}_{-0.035}$
He5.38	21.5	42.48	2.55	1.65	0.126
He5.38Ni	23	42.61	2.55	1.65	0.20
			LSQ13abf		
Str20	23	42.41	5.94±1.1	1.27±.23	0.16±.02
He6.0	24.5	42.23	2.82	1.07	0.084

Note. — Hun09 = Hunter et al. (2009);Str09 = Stritzinger et al. (2009); Val11 = Valenti et al. (2011); Sah11 = Sahu et al. (2011); Lym16 = Lyman et al. (2016); Pre16 = Prentice et al. (2016); Tad18 = Taddia et al. (2018); Str20 = Stritzinger et al. (2020). The hydrodynamical model of Taddia et al. (2018) was used to get $M_{\rm ej}$, $E_{\rm exp}$, and $M_{\rm Ni}$.

both the model and observations are expressed in the Vega system. The luminosity plotted from the model is just the portion in the 4000 - 10000 Å range, which is appropriate for the comparison.

Overall the agreement is excellent even though the model has a significantly longer time to peak, lower ejected mass, lower explosion energy, and smaller ^{56}Ni mass than previously estimated by the observers. Except for the time of peak, the discrepancy is not substantial. Our peak time includes 5 days spent at low optical luminosity ($\lesssim 2{\times}10^{41}$ erg s^{-1}) before the main diffusion dominated display commenced. The time of peak luminosity is also not very precisely defined. From 17 to 25 days after the star's initial explosion, the bolometric luminosity varied only 3% from its peak value. The ratio $M_{\rm ej}^3/E$ (in units of M$_\odot$ and 10^{51} erg) was 6.8 for the model, but varies from 1.39 to 0.35 for an assumed constant opacity 0.05 to 0.1 cm^2 g^{-1} for the observations (Prentice et al. 2016). Our opacity is not constant and our time to peak is quite different. Based on nebular spectroscopy Mazzali et al. (2010) estimates that $\sim$ 1 M$_\odot$ of heavy elements were ejected. Model He3.90 ejected 0.62 M$_\odot$ of heavy elements (besides neon) and 0.97 M$_\odot$ of helium and neon. A model with larger mass loss and the same presupernova mass would probably have the same ejecta mass, but more of its ejecta in the form of heavy elements. Also consistent with Mazzali et al. (2010), the intermediate mass elements in the model constitute 0.17 M$_\odot$ of the ejecta and the carbon to oxygen ratio is about 1/3. Mazzali et al. (2010) says $\sim$ 0.1 M$_\odot$ and a ratio of $< 1/5$. The latter ratio may be sensitive to convection physics and the rate for $^{12}{\rm C}(\alpha,\gamma)^{16}{\rm O}$.

The model spectrum again displays a striking deficiency in the ultraviolet, though the B magnitude appears well behaved. Unlike models for SN 2007Y and LSQ13abf, the pseudo-bolometric luminosity (4000 - 10000 Å) and the absolute magnitudes seem to be consistent. About 20 days after peak, the model spectrum begins to exhibit prominent features not apparent in the observations and we no longer trust the model. The bolometric luminosity should remain accurate til later though.

3.6.3. *SN 2009jf*

We next consider a supernova on the brighter end of the observed distribution, SN 2009jf. Observations in Table 6 suggest a luminosity and ^{56}Ni mass both greater than our fiducial limits of $10^{42.5}$ erg s^{-1} and 0.15 M$_\odot$. Our brightest model with standard mass loss is Model He5.38, with a peak bolometric luminosity of $10^{42.45}$ ergs^{-1}. Indeed, this is the brightest model for any central engine we considered (Ertl et al. 2020).

Valenti et al. (2011) suggest that SN 2009jf arose from a main sequence star of 25 - 30 M$_\odot$. The main sequence mass that produced Model He5.38 was 22 M$_\odot$, but the usual uncertainty regarding mass loss applies More mass

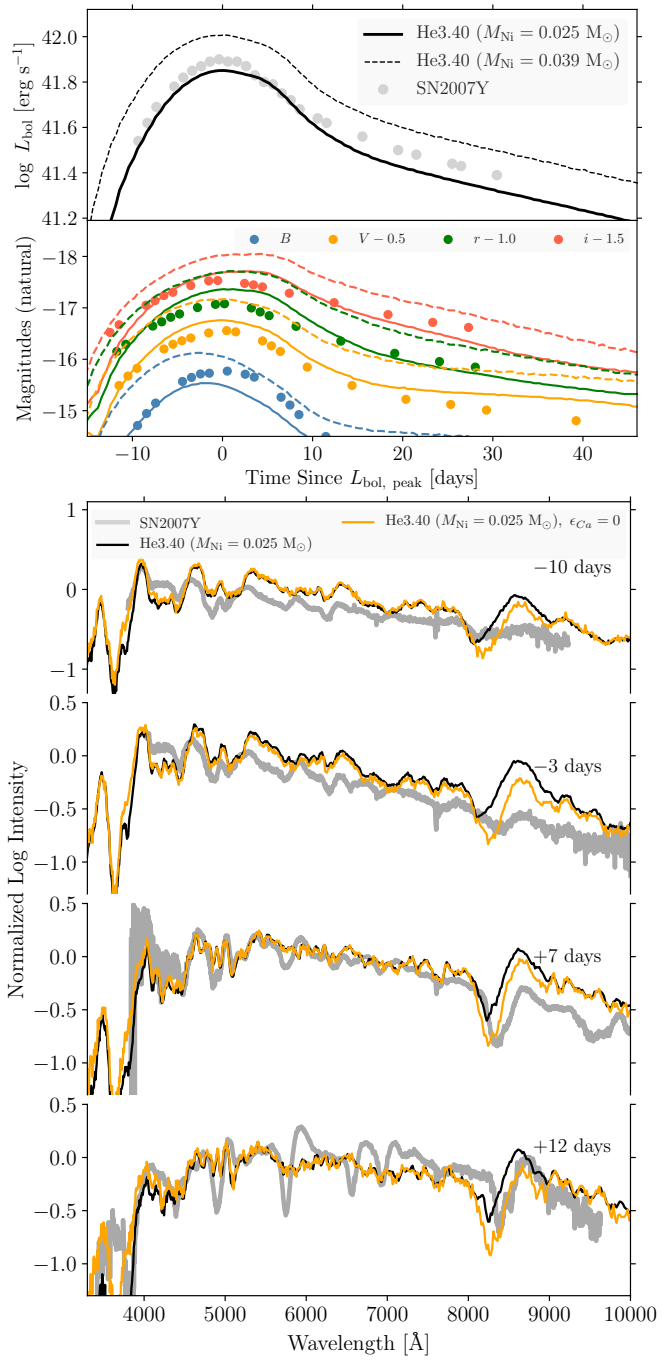

FIG. 14.— Bolometric luminosity, color magnitude evolution, and spectra for SN 2007Y (Stritzinger et al. 2009) compared with the standard Model He3.40 (0.039 M$_\odot$; Table 1; dashed line) and an equivalent model with with a reduced ^{56}Ni mass (0.025 M$_\odot$; solid lines in the top two panels). The model and observed spectra are normalized to give the same value at 5200 Å. The model and observations are in good agreement for the interval given for the smaller ^{56}Ni mass.

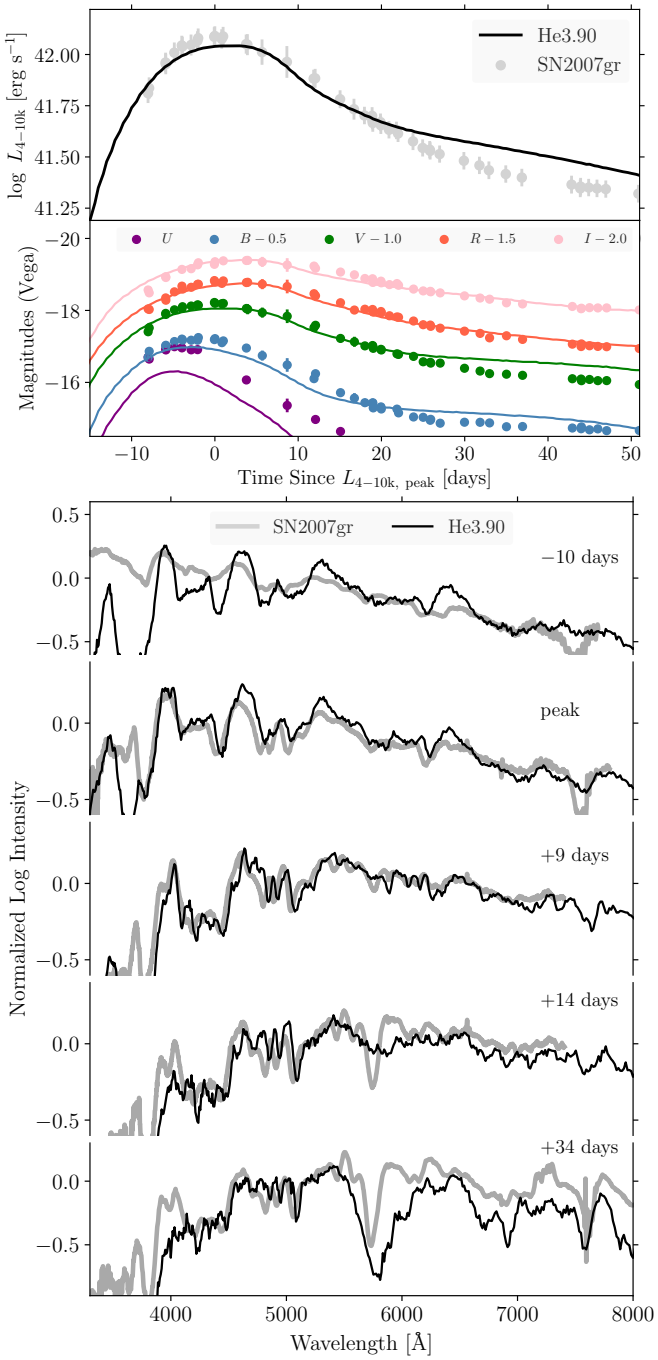

FIG. 15.— Bolometric luminosity (Prentice et al. 2019), color magnitude evolution (Hunter et al. 2009), and spectra (Modjaz et al. 2014; Shivvers et al. 2019) for SN 2007gr, a Type Ic supernova, compared with Model He3.90 (Table 1). The model and observations are in good agreement for the interval given.

loss implies a bigger main sequence progenitor.

Fig. 16 and Table 6 show the comparison between Model He5.38 and observations. The photometry and spectra were again provided by Simon Prentice and have been corrected for redshift, extinction and reddening. The pseudo-bolometric luminosity is shown which should be compared with our 4000 - 10000 Å evaluation. The original photometry is from Valenti et al. (2011) and the spectra are taken from Valenti et al. (2011) and Modjaz et al. (2014). Despite the inadequate luminosity, the agreement is pretty good. It can be made better by artificially invoking the synthesis of 0.20 M$_\odot$ of ^{56}Ni. Consistent with the estimates of what is needed in Table 6 this is a 60% increase for the standard model (0.126 M$_\odot$). Interestingly, the spectrum is not altered very much by this enhancement at times before and during peak, but

is appreciably better with enhanced ^{56}Ni at later times. The enhanced nickel maintains ionization to a later time and keeps the photosphere from collapsing.

While the improvement resulted here from augmented nickel, probably any source of centrally concentrated, energetic radiation would have a similar effect. It is an interesting question whether there might be spectroscopic signatures of a point source (magnetar) in a mixed supernova that also contains radioactivity. Whether that is all meaningful in the context of a one-dimensional model could be questioned. It does seem though that the spectrum and light curve are better explained by an augmented central source than by, e.g., circumstellar interaction.

From an analysis of the nebular spectrum, Sahu et al. (2011) estimated a lower limit to the oxygen ejected in SN 2009jf of ~ 1.34 M$_\odot$. Model He5.38 only ejected 0.72 M$_\odot$. There are three possibilities: a) their measurement could be an overestimate; b) SN 2009jf came from a more massive presupernova star; or c) our presupernova mass is correct, but SN 2009jf was derived from a more massive star that experienced greater mass loss so that much of what was helium in Model He5.38 (0.97 M$_\odot$) was actually ^{16}O. With regards to b), Model He7.13 (Table 1) fits the observations near peak reasonably well (with the same augmentation to ^{56}Ni) and ejects 1.35 M$_\odot$ of ^{16}O, but its light curve is overly broad and it declines too slowly compared with the observations. A larger explosion energy would help, but that is not a free parameter in the present study. With regards to c), Model He12.00x2, a 12 M$_\odot$ helium core evolved with twice the mass loss rate ($f_{\rm WR} = 2$) has almost the same presupernova mass (4.03 M$_\odot$) as He5.38 (4.05 M$_\odot$) and is thus expected to have similar luminosity, color, and time scale. The presupernova model for He12.00x2 contained 1.09 M$_\odot$ of ^{16}O. This would change slightly in the explosion.

3.6.4. *LSQ13abf*

Heavier supernovae have broader, redder light curves. Fig. 17 shows a comparison of Model He6.00 (presupernova mass 4.44 M$_\odot$) with Type Ib supernova LSQ13abf as reported by Stritzinger et al. (2020). Photometry for LSQ13abf is taken from their Table 2, where magnitudes are given in the CSP natural system. These apparent magnitudes are translated into absolute magnitudes using a distance modulus for SDSS J114906.64+191006.3 of 34.96 and a correction for extinction by the Milky Way of $A_V = 0.087$ mag assuming reddening law characterized by $R_V = 3$ (Stritzinger et al. 2020). The resulting values agree with what is plotted in Fig. 3 of Stritzinger et al. (2020). Assuming that LSQ13abf exploded on JD 2456395.80, yields the values compared with Model He6.00 in Fig. 17.

Model He6.00 agrees quite well with the observations except during the first week when factors other than the expansion of a compact Wolf-Rayet star are clearly at play. The similarity with SN 2008D (Stritzinger et al. 2020) naturally leads to the suspicion of an extended envelope or circumstellar interaction, as was invoked by many to explain the very early observations of that event (Bersten et al. 2013; Chevalier & Fransson 2008; Katz et al. 2010; Sapir et al. 2013; Piro 2015; Dessart et al. 2018; Ioka et al. 2019). An extended envelope is a natural solution (Dessart et al. 2018; Woosley 2019; Ertl et al. 2020), especially given the possibility of degenerate silicon flashes that can occasionally eject substantial amounts of matter during the weeks and months prior to the final explosion. For mild flashes, as in Model He3.20, the effects are difficult to distinguish from ordinary envelope inflation during earlier burning stages.

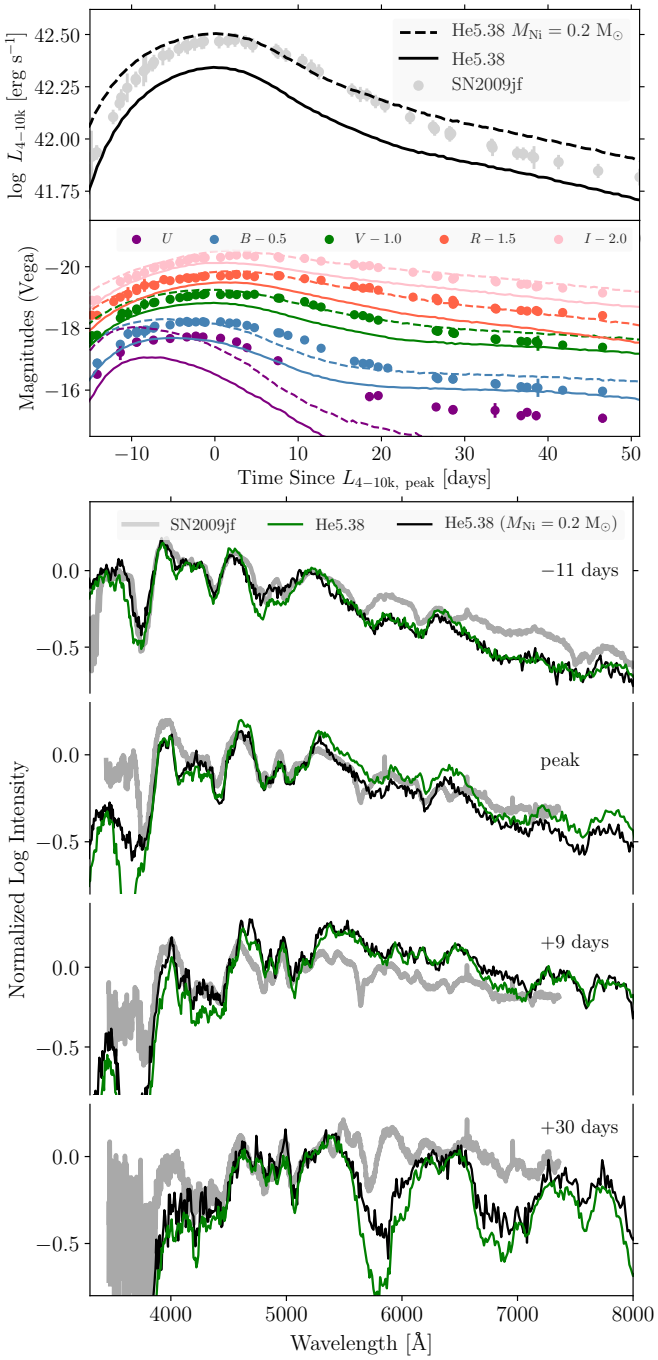

FIG. 16.— Bolometric luminosity (Prentice et al. 2019), color magnitude evolution, and spectra for SN 2009jf (Valenti et al. 2011), a Type Ib supernova, compared with Model He5.38 (Table 1). Solid lines in the upper two frames are the unmodified model which produced 0.126 M$_\odot$ of ^{56}Ni. Dashed lines show the effect of increasing the ^{56}Ni yield to 0.20 M$_\odot$ to improve agreement. The model and observations are in good agreement for times up to 10 days after the peak. By 30 days after peak, the model has broken down and the spectrum cannot be trusted.

Even Model He3.20 is too faint, especially in the red, to give the early light curve of LSQ13abf (Fig. 17). The deep dips in the light curve when the supernova is only a few days old, might be weaker in a multidimensional model or one where mixing was treated more realistically. Even then a greater mass at a larger radius seems to be required.

The problem is that for our presupernova model set (Woosley 2019) both radius inflation and silicon flashes are absent in models more massive than He3.20 (presupernova mass 2.7 $M_\odot$), yet the width of the light curve at peak seems to demand a greater mass. We are thus unable to fit the entirety of the LSQ13abf light curve. The situation might change if the envelope of the presupernova star for LSQ13abf, and similar supernovae like SN 2008D contained a trace of hydrogen (Dessart et al. 2018). This is well worth pursuing. Could a bit of high velocity hydrogen be hiding in the spectrum of many of these supernovae that show evidence for radius inflation? All our models are, by construction, hydrogen free, so we do not see this effect. Dessart et al. (2018) also described a single helium star model, He_R173, with large presupernova radius (173 $R_\odot$) and moderate presupernova mass (2.73 $M_\odot$). Our equivalent model in terms of presupernova mass, Model He3.40, had a much smaller radius, 7.7 $R_\odot$, but this star is near the boundary between large expansion and small. Different treatments of semiconvection (Dessart et al. 2018, have less) and opacities might explain the dichotomy. In any case, their Model He_R173, like our He3.20, was only capable of explaining the early evolution of the light curve and not its broad width.

If LSQ13abf did not contain hydrogen then something else may be going during that first week. Perhaps a magnetar is providing extra energy the first few days and becoming less important later on (Kasen et al. 2016)? Or perhaps there was circumstellar interaction. Our models have sufficient surface resolution to estimate the energy in mildly relativistic ejecta, $\beta > 0.1$. For Model He6.00, the outer $\sim 5\times10^{-4}$ $M_\odot$ had velocity greater than 30,000 km s^{-1}, corresponding to a kinetic energy in excess of 5×10^{48} erg. The total energy in the early light curve sampled during the first 10^6 seconds of the evolution of LSQ13abf is of order 10^{48} erg. Provided the fast moving ejecta encounters its own mass inside $\sim 3 \times 10^{16}$ cm, the energetic needs of the light curve could be satisfied. Assuming a wind or pre-explosive ejection speed of 1000 km s^{-1}, this requires a mass loss rate of $\sim 10^{-4}$ $M_\odot$ y^{-1}. This is much more than our standard Wolf-Rayet mass loss rate, but perhaps not too unusual for the last 10 years of the star's life when advanced burning stages and semi-degenerate flashes are in progress.

In any case, Fig. 17 shows the good agreement between the observations of LSQ13abf, especially for B and V near peak, and Model He6.00. The bolometric luminosity at peak is only 65% of the observed value (Table 6 here and Stritzinger et al. 2020), but half of that difference might reasonably be accommodated by a slight increase in the ^{56}Ni mass from 0.084 $M_\odot$ to say 0.11 $M_\odot$. This would also brighten the photometry in the B and V bands, but perhaps not unacceptably.

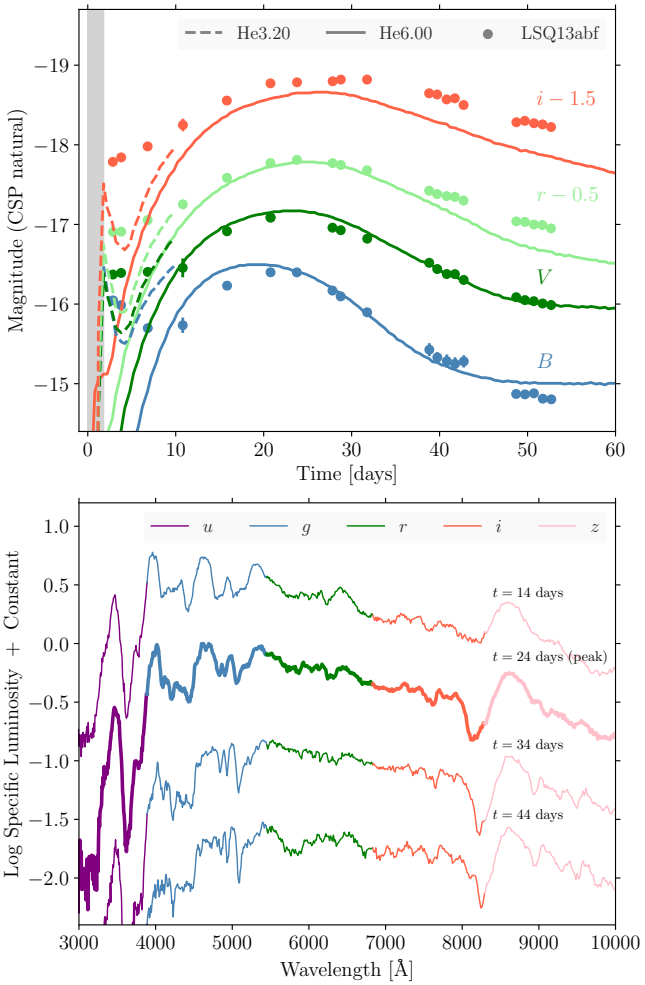

FIG. 17.— Comparison of Model He6.00 with supernova LSQ13abf. (top:) Photometry of the supernova LSQ13abf (Stritzinger et al. 2020) compared with Model He6.00 (solid line). The fit is remarkably good after the first week in all bands except i. The early light curve may be due to envelope expansion and the first 10 days of Model He3.20 are plotted for comparison (dashed line). (bottom:) The spectrum of Model He6.00 calculated using SEDONA at bolometric peak (24 days) and 10 days before and 10 and 20 days after. To facilitate comparison with the light curve, the spectrum has been color coded with the filters indicated corresponding to the approximate wavelength range for SDSS *ugriz* filters.

3.6.5. *SN 2008D*

Although similar to LSQ13abf in appearance and possibly in explanation, SN 2008D is worth separate mention because it is so well studied and has an accurately determined explosion time. Like LSQ13abf, the light curve has two peaks and is very bright during the first week possibly due to a large radius for the presupernova star or a recently ejected shell. Here apparent magnitudes are taken from Bianco et al. (2014) in standard (Vega) magnitudes. These are converted to absolute magnitudes by normalizing the peak V magnitude to 17.0±0.3 and B magnitude to 16.3±0.4. These values account for a substantial host reddening ($E(B-V) = 0.6\pm0.1$ mag). An explosion date of MJD 54474.56 is assumed (Soderberg et al. 2008).

Modjaz et al. (2009) estimate that SN 2008D reached its bolometric peak at 19.2±0.3 days post-explosion with a luminosity of $10^{42.2\pm0.1}$ erg s^1. Malesani et al. (2009)

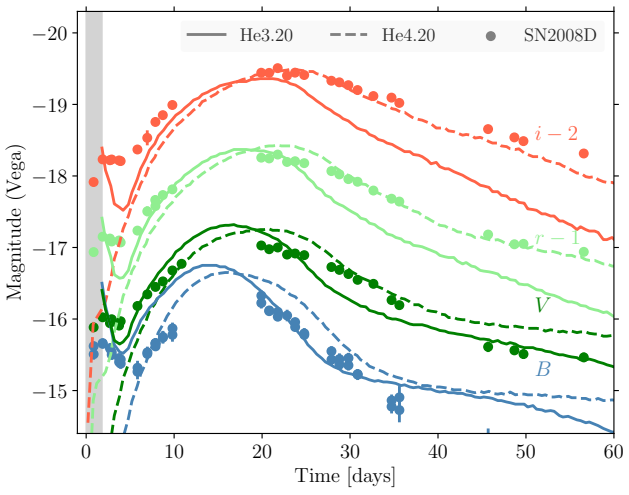

FIG. 18.— Comparison of Model He3.20 (solid line) and He4.20 (dashed line) supernova 2008D. Model He3.20 experienced a weak silicon flash and substantial radius expansion before exploding and that accounts for its brilliance at early times. The model overall gives too narrow a light curve however, and Model He4.20 is a better fit to the peak.

give $10^{42.3}$ erg s^{-1}. Fig. 18 shows a comparison of the $BVri$ light curves of SN 2008D and Models He3.20 and He4.20. Model He3.20 has a peak luminosity of $10^{42.22}$ erg s^{-1} at 16.5 days. Model He4.20 has a peak luminosity of $10^{42.22}$ erg s^{-1} at 21.0 days which agrees better with observations. The display from He3.20 might be made brighter and redder during the first week if it had a larger initial radius or an envelope containing more mass. Both could come from an earlier or more energetic silicon flash.

The problem with SN 2008D is the same as for LSQ13abf, though not as severe. Models with significant radius expansion give light curves that are too narrow to explain the peak. Models that explain the peak fail to reproduce the first week's data. A more massive model with a supergiant structure or shell ejection is needed (see also §3.6.4 and Dessart et al. 2018). The presence of residual hydrogen near the surface might facilitate this expansion for the more massive stars. Other similar "double-peaked" supernovae with ambiguous evidence for high velocity hydrogen might be noted, e.g. SN 2013ge (Drout et al. 2016).

4. LOW MASS EXPLOSIONS

For presupernova masses less than about 2.6 M$_\odot$ (standard initial helium star masses less than 3.3 M$_\odot$), advanced burning stages are punctuated by off-center burning and, at the lower end, by degenerate flashes (Table 7 of Woosley 2019). For presupernova masses less than about 2.1 M$_\odot$, electron-capture supernovae may occur. While presupernova masses less than 2.6 M$_\odot$ should be common in nature, their properties - low explosion energy, small ^{56}Ni mass, and small ejected masses - make them unlikely to appear as common Type Ib and Ic supernovae (Tauris et al. 2015; Moriya et al. 2017; Woosley 2019; Ertl et al. 2020). But what would explosions in presupernova stars with masses in this range look like?

Major uncertainties for those models that experience a strong silicon flash: He2.50, He3.00, He3.10, and He3.20, are the energy and timing of the flash (Woosley 2019). If the flash is powerful, it ejects a lot of mass and, since the recovery time for the remaining core is longer for a strong flash, this matter coasts to a large distance before the iron core finally collapses. In extreme cases, the ensuing supernova is powered by circumstellar interaction and can be very bright. For the weaker flashes, the star ejects less mass at slow speed. The effective radius is not greatly increased, and the supernova is similar to what would have happened without a flash - a faint, fast Type Ib supernova.

The version of SEDONA employed here is incapable of treating supernovae powered by shock interaction. Homologous coasting is assumed. For illustration, we thus consider only two cases. Model He2.50 is characteristic of stars where the silicon flash has a moderate influence, leading to the substantial expansion of the outer layers of the presupernova star prior to iron core collapse, but not to the extent ($\sim 10^{15}$ cm) where circumstellar interaction becomes a major contributor to the light curve. The other, Model He2.60, is a case where the silicon flash is avoided, or very weak, but the star already has an initial radius of over 100 R$_\odot$. As we shall show, both have similarities to one another and to SN 2010X and similar fast blue transients. These stars are similar to He3.20 which we treated as an ordinary Type Ib supernova, but are treated separately here because their lower explosion energies, small ^{56}Ni production, and large radii cause them to appear qualitatively different.

Model 2.5B as defined in Table 7 and Fig 14a of Woosley (2019), experienced a silicon flash 19 days before core collapse and ejected 0.25 M$_\odot$ with a typical speed of just a few hundred km s^{-1}. By the time the shock from core collapse arrived at the surface, the outer edge of the ejected matter had only coasted to $\sim 7 \times 10^{13}$ cm. The subsequent explosion thus resembled what would have happened in a helium red supergiant with an unusually large radius. The shock interaction in the outer layers was different (the shock decelerated rather than accelerating, generating a strong reverse shock), but the light curve was similar. The main shock took about a day to reach the photosphere and, after expanding an additional two days, was coasting approximately homologously. At that point the KEPLER model was linked into the SEDONA code. Except for a very thin high velocity layer at the surface, the exploding star was all optically thick at this point

The results of the explosion (Ertl et al. 2020) for this model and several variations are shown in Fig. 19. For the standard case, the total ejected mass was 0.737 M$_\odot$ including that already ejected in the silicon flash; the kinetic energy was 1.1×10^{50} erg and 0.0151 M$_\odot$ of ^{56}Ni was produced. The light curves in the U, B, V, and r bands are shown. Shock break out and early expansion were not followed. A plateau, as shock deposited energy is released by helium recombination and diffusion, is followed by the abrupt fall off to a faint radioactive tail. On the plateau typical photospheric temperatures, from KEPLER, ranged from 16000 K on day 5 to 10000 K on day 15 and the photospheric velocity ranged from 12,000 to 4,000 km s^{-1} in the same period. A similar model was considered by Kleiser et al. (2018a), but here we use different approach to model the presupernova evolution and explosion. The radius is larger due to the silicon flash and the kinetic energy and ^{56}Ni masses were com-

puted in a less parametrized model for the explosion. Also shown on the plot are data points for the r-band light curve of SN 2010X. Data is taken from Kasliwal et al. (2010) with Julian date 55231.8 days in their table corresponding to day 0 on the plot, and with a distance modulus of 34.11. (The Open Supernova Catalog; `https://sne.space/sne/SN2010X/`).

The unmodified model is similar to the r-band light curve of SN 2010X, but a bit too faint and expands too slowly at late times (Kasliwal et al. 2010). Reasonable modifications can improve the fit. Kleiser et al. (2018a) obtained a similarly good fit to the r-band light curve with a dialed-in explosion energy of 1.0×10^{51} erg and 1.33 $M_\odot$ of ejecta (their Model M2.73-E1). The neutrino-transport models of Ertl et al. (2020) that underlie the present study suggest an explosion energy of, at most, a few $\times 10^{50}$ erg for this low mass range. Even with an ejected mass half as large, we would be unable to approach the brilliance of SN 2010X using the radii adopted by Kleiser et al. (2018a). The large radius from the silicon flash helps substantially, and a still larger radius is well within the range of possible silicon flash characteristics, but this does not address the low velocity.

Raising the explosion energy from 0.11 to 0.3 $\times 10^{51}$ erg helps with both issues and, while not specifically what Ertl et al. (2020) calculated for this star, a higher energy is found in other cases with low mass, e.g., Model He3.00 had an explosion energy of 0.3 $\times 10^{50}$ erg and also experienced a silicon flash. Using this energy and a slight adjustment to the ^{56}Ni synthesis yields a better fit to the r-band light curve of SN 2010X and raises the velocity by about 50%.

One merit of fitting SN 2010X this way is that similar models might fit other more luminous supernovae with rapid rise and decline rates. Explaining supernovae like SN 2002bj (Poznanski et al. 2010; Kasliwal et al. 2010; Kleiser et al. 2018b) is difficult because the ^{56}Ni abundance required to explain its peak luminosity, if the supernova light curve is powered by radioactivity, would also produce a bright tail. If the luminosity at peak is determined by recombination releasing shock-deposited energy however, then one is at liberty to vary ^{56}Ni to fit the tail. SN 2002bj had a similar rapid rise and decline to SN 2010X, but was 1.5 magnitudes brighter and seemingly lacked a radioactive tail. A good first approximation to that event might be Model 2.5C of Woosley (2019, his Fig. 14).

A similarly good fit to the r-band light curve of SN 2010X and similar events is possible using a different sort of model. Model He2.60 had a presupernova mass of 2.15 $M_\odot$, a radius of 7.8×10^{12} cm. Using the standard W18 central engine (Ertl et al. 2020), the star exploded with a final kinetic energy of 1.5×10^{50} erg and produced 0.018 $M_\odot$ of ^{56}Ni. The explosion left a bound remnant of 1.36 $M_\odot$ and thus ejected 0.782 $M_\odot$, mostly composed of helium. The resulting light curves are shown in Fig. 20.

The bolometric light curve of the unmodified model shows a strong first peak resulting from the expansion and recombination of the helium, similar to but fainter than Model He2.6 because of the smaller radius. Because the ejected mass is smaller, the velocity is higher, $\sim$7000 km s^{-1} at day 10. Following helium recombination, the photospheric radius is small and the high luminosity again gives a hot temperature and a blue color. A secondary maximum in bolometric emission occurs around 20 days due to radioactivity. For a star with a smaller presupernova radius and greater ^{56}Ni production, this secondary peak dominates and one would have a more typical Type Ib or Ic supernova. In the unmodified model the two components are comparable and, depending on the filter employed, one might see a double-peaked light curve.

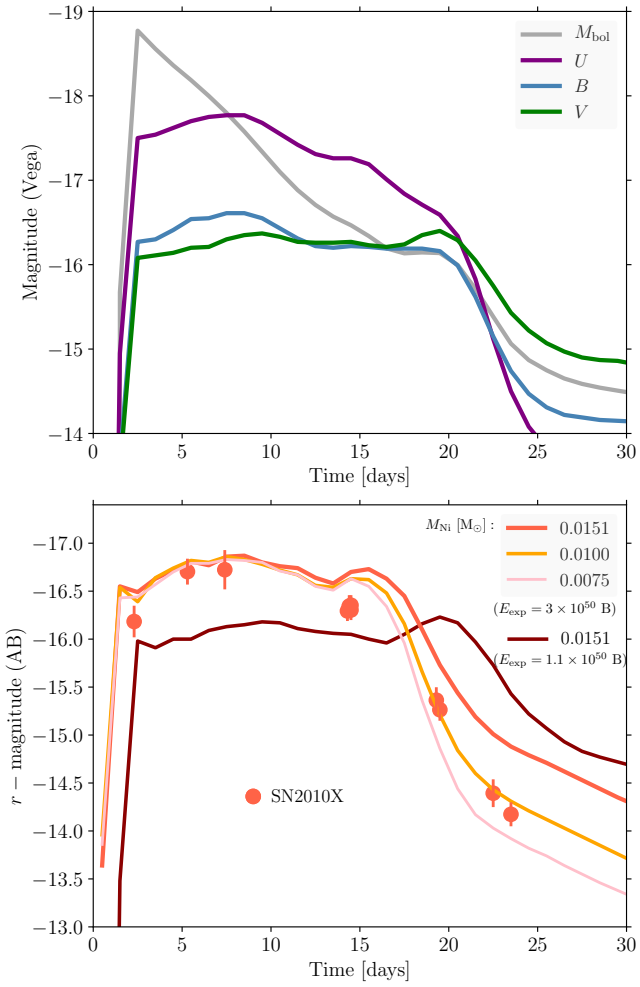

FIG. 19.— Light curves for Model He2.50. This model had a large initial radius, 6.40×10^{13} cm, owing to a degenerate silicon flash 19 days before final core collapse (see Model 2.5B of Woosley 2019). The model ejected a mass of 0.737 $M_\odot$ of which 0.0151 $M_\odot$ was ^{56}Ni. The kinetic energy of the unmodified explosion was low, 1.1×10^{50} erg. The top panel shows the bolometric and UBV light curves for this explosion in the Vega magnitude system. Results before 3 days are not reliable due to the initialization of the calculation in SEDONA. The bottom panel shows the r-band light curves for the same model and some modifications. The solid dark purple curve shows the results for the unmodified model. The pink, orange, and red curves are artificial adjustments that used a larger explosion energy of 3×10^{50} erg with varying masses of ^{56}Ni, 0.0075 $M_\odot$ (pink); 0.01 $M_\odot$ (orange) and 0.0151 $M_\odot$(red). The higher energy explosions with slightly lower ^{56}Ni mass are a good fit to SN 2010X.

The bottom frame of Fig. 20 shows the r-band light curve with several modifications again compared with observations of SN 2010X. A model with a smaller presupernova mass was generated by artificially increasing the mass loss rate so that the ejected mass was about half as large, 0.37 $M_\odot$. With this smaller mass the early display

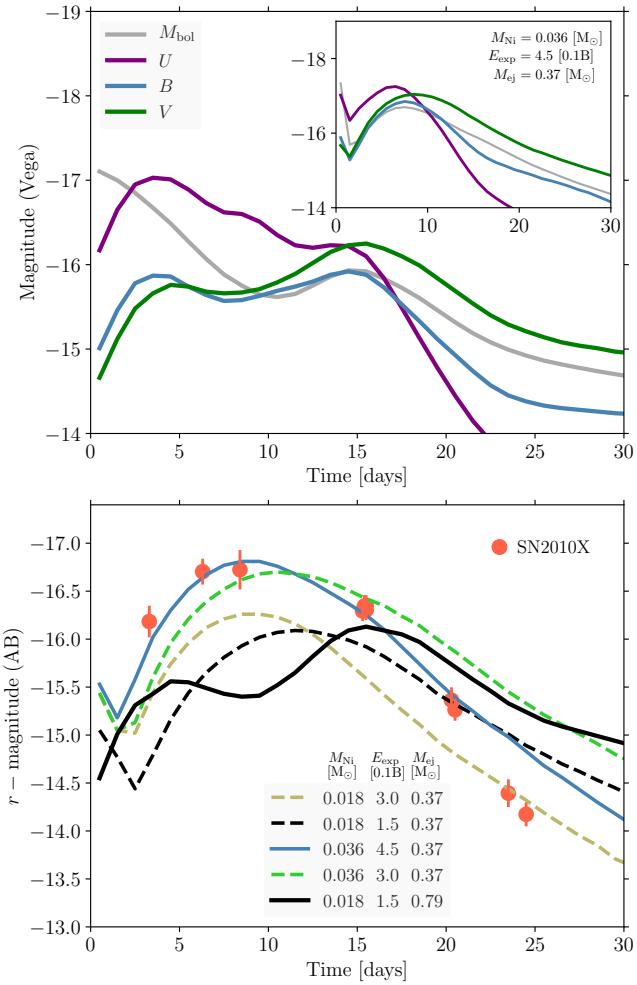

FIG. 20.— Light curves for Model He2.60. This model experienced no silicon flash and had an initial radius of 7.8×10^{12} cm. The explosion ejected 0.782 M$_\odot$ with a kinetic energy of 1.5×10^{50} erg and produced 0.018 M$_\odot$ of ^{56}Ni. (top:) U, B, V, and bolometric light curves for the unmodified model with the best-fit modified model from the lower panel shown as an inset. (bottom:) the r-band light curve for the standard case (solid black line) and four variations that reduced the ejecta mass by about a factor of two to 0.374 M$_\odot$ and varied the amount of ^{56}Ni. The ^{56}Ni mass and kinetic energies are indicated in the inset table. Unlike Fig. 19, all light curves here are powered at peak by radioactive decay. Red data points are for SN 2010X (Kasliwal et al. 2010) and are fit reasonably well by the blue curve. U, B, V, and bolometric magnitudes for the blue curve are given as an inset in the top panel.

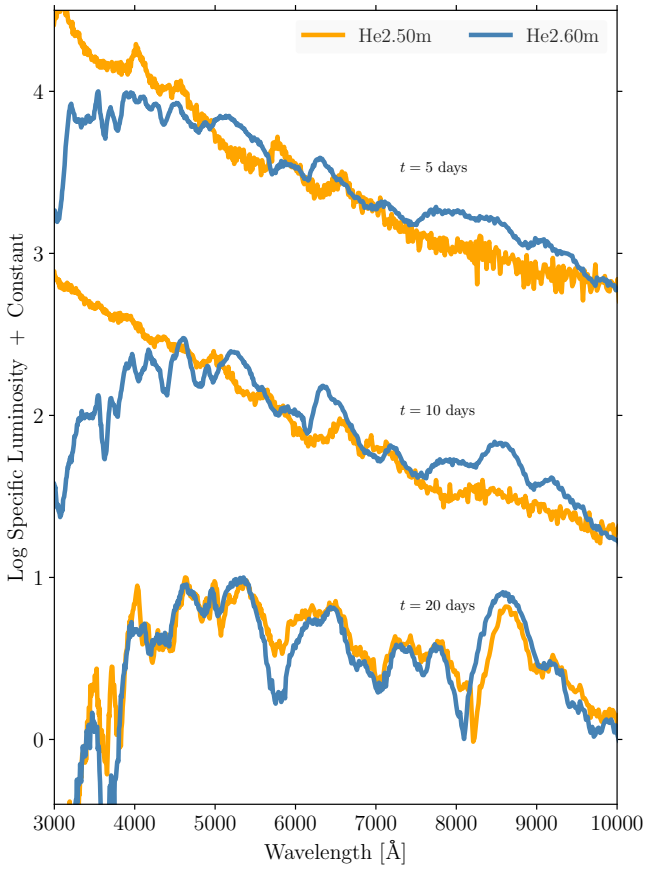

FIG. 21.— Spectra for the modified ("m") best fit models in the lower panels of Fig. 19 and Fig. 20. Both models are evaluated (from top to bottom) at 5, 10, and 20 days post explosion. Model He2.50m declines rapidly bolometrically during its r-band plateau phase (5 and 10 days), and becomes similar to Model He2.60m as both approach their radioactive tails (20 days). Model He2.50m declined monotonically after shock break out and had bolometric magnitude of -18.19 and -17.10 at days 5 and 10 respectively. This corresponds to luminosities of 5.7 and 2.1 $\times 10^{42}$ erg s^{-1}. It reached an r-band maximum magnitude of -16.82 at 8.7 days. Model He2.60m had bolometric maximum of M_{bol} = -16.7, L_{bol} = 1.4 $\times 10^{42}$ erg s^{-1} at 8.0 day and a r-band maximum magnitude of -16.89 at 10 days. t = 10 days in the figure is thus approximately r-band peak.

from helium recombination is reduced and the radioactive peak occurs earlier (black dashed line in Fig. 20). Additional artificial increases in the ^{56}Ni mass and explosion energy both brighten and shorten the display. Increasing the energy by a factor of three to 4.5×10^{50} erg and doubling the ^{56}Ni mass to 0.036 M$_\odot$ results in a Model He2.6m (solid blue line in Fig. 20) that agrees quite well, except at very late times, with SN 2010X. As with Model He2.50, these changes are substantial, but not incredible. Indeed, this model is quite similar to what Kasliwal et al. (2010) themselves proposed to explain their observations. The outer third of the ejecta now moves at over 10,000 km s^{-1} and this is also in better agreement with observations.

Model He2.6m is also similar to the "ultra-stripped" supernovae discussed by Tauris et al. (2013), Tauris et al. (2015), and Moriya et al. (2017). In their typical model for SN 2010X, there is no silicon flash and the entire light curve after breakout is powered by radioactive decay. In that model, core collapse ejects a small amount of mass ($\sim$ 0.16 M$_\odot$) with a low explosion energy (1 to 2.5×10^{50} erg) that contains a modest amount of ^{56}Ni ($\sim$ 0.02M$_\odot$). Our Model 2.60m (Fig. 20), on the other hand, ejects 0.37 M$_\odot$, of which 0.036 M$_\odot$ is ^{56}Ni, with an explosion energy of 4.5×10^{50} erg. In terms of peak bolometric luminosity, 1.4×10^{42} erg s^{-1}, peak time of about 8 days, and velocity $\sim (E/M)^{1/2}$, the two models are similar. Model He2.60m had a greater presupernova mass though, 1.70 M$_\odot$ vs Moriya's 1.50 M$_\odot$. More critically, the presupernova models of Tauris et al. (2013) had a small helium envelope (0.033 M$_\odot$) and a much smaller radius (0.4 R$_\odot$) due to the assumption of evolution in a very compact binary. Our modified best fit model ejected 0.28 M$_\odot$ of helium and had a presupernova

radius of about 100 $R_\odot$. Because of this large radius, it is much brighter early on than that of Moriya (Fig. 20).

The best model for a particular 2010X-like supernova, He2.50m or He2.60m, can be better determined from the time history of the colors and spectrum. Fig. 21 gives the spectrum for the two best-fit, modified models in Fig. 19 and Fig. 20 at three different times. He2.50m is derived from a helium supergiant and stays hotter longer with a temperature set, in part, by the partial recombination of helium. It is bluer near peak and much bluer at earlier times. Once the diffusion of decay energy dominates though, the spectrum of He2.5m resembles closely that of He2.60m. If the time of explosion were not well known, one model could be confused for the other, especially if data were lacking at wavelengths less than 4500 A. Comparing with Fig. 2 of Kasliwal et al. (2010), Model He2.6m, the radioactive model, is a better fit to the observed spectrum of SN 2010X itself 3 or 4 days before visual peak (approximately +5 days here).

5. HEAVIER MODELS - LONG RED TRANSIENTS

For presupernova masses above 5.6 $M_\odot$ which, for $f_{\rm WR} = 1$ correspond to initial helium star masses above 8 $M_\odot$ (13 $M_\odot$ for $f_{\rm WR} = 1.5$), the light curves become too broad and faint to be common Type Ib and Ic supernovae (Ensman & Woosley 1988; Ertl et al. 2020; Prentice et al. 2019). Fig. 22 and Fig. 23 show the multiband light curves and spectra for two cases. Compared with the events in §3, these massive explosions are not only fainter and broader, but redder than common events and characterized by narrower spectral lines. The color index $(B-V)$ for typical Type Ib supernova Model He4.50, at V-peak, is 0.70. For He12.0 and He19.0 it is 0.98 and 1.07. Based on KEPLER calculations the photospheric velocity for Models He6.00, 12.0 and 19.0 at peak are 7900, 5400, and 4800 km s^{-1} (Ertl et al. 2020). The explosion energies and ^{56}Ni masses are comparable (Table 1 and Table 2), but the ejecta masses are greater, so the velocity is lower and the time scales longer.

Because of their large mass, the frequency of such events is small. Ertl et al. (2020) speculated that at least a fraction of them might involve explosion mechanisms and light sources other than neutrinos and radioactivity. Some may be the progenitors Type Ic-BL supernovae and gamma-ray burst supernovae, but probably not all.

It is interesting to compare Model He12.0 with SN 2013bb (Prentice et al. 2019). Though classified as a Type IIb supernova, the appearance of SN 2013bb after the first few weeks might not be so different from a Type Ic event. It has the longest light curve yet observed for a stripped envelope explosion (Prentice et al. 2019). SN 2013bb had a peak luminosity (4000 - 10000 Å) of $\log L_{4-10k} = 42.0 \pm 0.1$ erg s^{-1}; an uncertain peak time of at least ~ 25 days; a decline time $t_{+1/2}$ of 56 ± 10 days; an inferred ejected mass of 4.8 $M_\odot$; a velocity at peak of 7000 km s^{-1}, and an inferred ^{56}Ni mass of 0.07 ± 0.02 $M_\odot$. Model He12.00 had a peak luminosity (4000 - 10000 Å) of $\log L_{4-10k} = 41.92$ erg s^{-1}; a peak time of 39 days; a decline time $t_{+1/2}$ of 41 days, an ejected mass of 5.33 $M_\odot$; a velocity at peak of about 5400 km s^{-1}; and an inferred ^{56}Ni mass of 0.079 $M_\odot$. The decline time for the model is perhaps a bit short, but the time of peak luminosity is poorly defined in the model and presumably

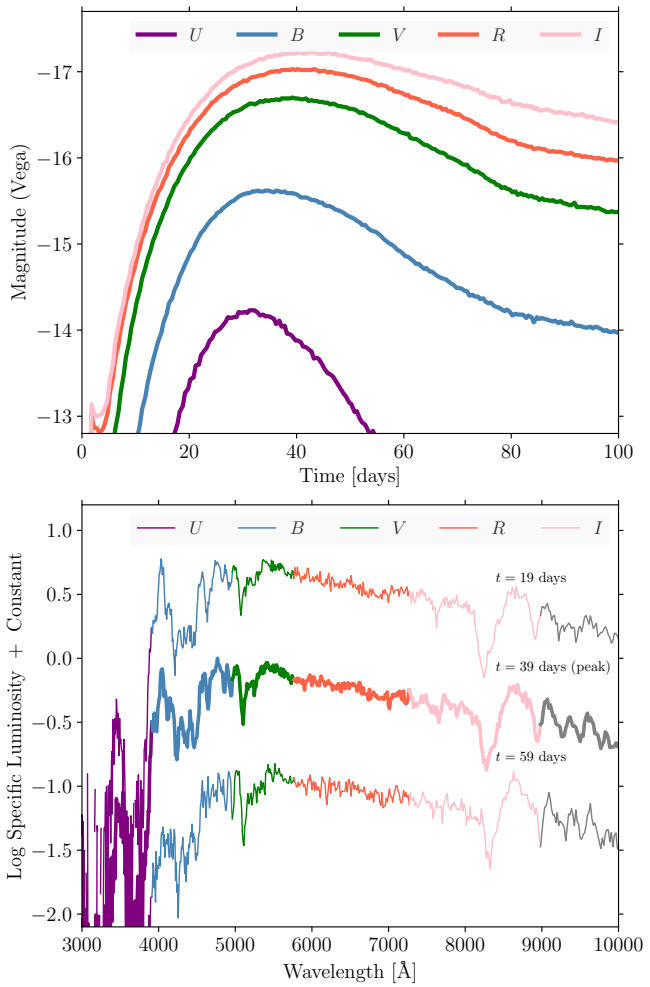

FIG. 22.— (Top:) Light curve for Model 12.0. The explosion ejected 5.33 $M_\odot$ with a kinetic energy of 0.81×10^{51} erg and synthesized 0.0792 $M_\odot$ of ^{56}Ni. (top:) Vega-based $UBVRI$ light curves until 100 days. (bottom:) Spectra at peak (39 days) and at minus and plus 20 days.

in the observations as well. The luminosity only varies 1% in an interval of 6 days around peak and 5% in 10 days. Shifting our definition of peak back 5 days would improve the agreement considerably. Other models with initial helium star masses in the range 9 to 13 $M_\odot$ had similar properties (Table 5 of Ertl et al. 2020). Minor modifications of the uncertain ^{56}Ni mass and explosion energy and including a small residual hydrogen envelope could account for the small differences with SN 2013bb.

Apparently SN 2013bb was of the same family as common Type Ib and Ic supernovae, but happened in a more massive star with a small residual hydrogen envelope. Observers should be on the look out for more of these and similar cases where there is less hydrogen.

6. CONCLUSIONS

The spectra and light curves resulting from the explosion of a broad range of mass-losing helium stars have been calculated and compared with observed "stripped envelope" supernovae. The models are representative of the endpoints of evolution in close, mass-exchanging binary systems. The presupernova evolution of these stars, their neutrino-powered explosions, their nucleosynthesis,

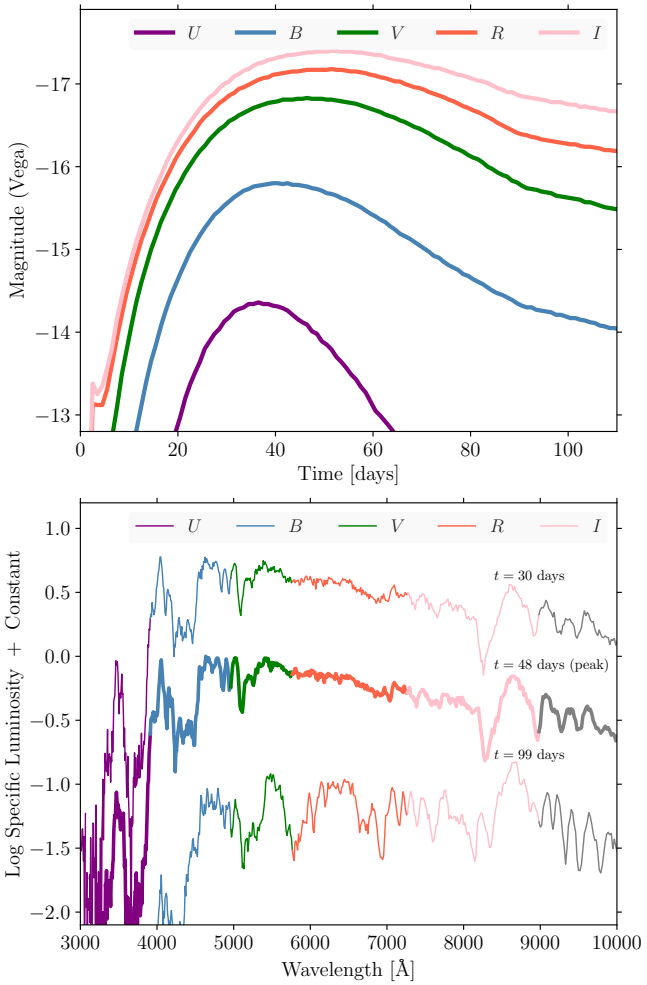

FIG. 23.— Multiband light curves and spectra for Model 19.0. (top:) *UBVRI* light curves as in Fig. 22. Due to the kinetic energy per unit mass the light curve is very broad, faint, and red. (bottom:) Spectra at peak light (48 days) and at 30 days and 99 days. Note the presence of many narrows lines reflecting the slow expansion speed.

and the distribution of remnant masses they leave behind has been published previously (Woosley 2019; Ertl et al. 2020; Woosley, Sukhbold, & Janka 2020). Here emphasis is on a careful treatment of the radiation transport using the SEDONA code and a comparison with modern observations.

For a range of presupernova masses from 2.2 to 5.6 $M_\odot$, the models are in good qualitative agreement with observations of common Type Ib and Ic supernovae. The median values of some major observables are given in Table 3 and the comparison depends on how well observers have sampled this broad mass range. Light curves from lower mass explosions are brief and faint and some may have been overlooked. Similarly, the light curves of very massive models are broad, faint, and red and could also be under-sampled. Depending upon the assumed mass loss rate, the presupernova mass range 2.2 to 5.6 $M_\odot$ corresponds to initial helium star masses of 2.7 to 8 $M_\odot$ for $f_{\rm WR} = 1$ and 3.0 to 13 $M_\odot$ for $f_{\rm WR} = 1.5$. These helium stars are, in turn, derived from main sequence mass stars of approximately 14 - 28 $M_\odot$ for $f_{\rm WR} = 1$ and 15 - 38 $M_\odot$ for $f_{\rm WR} = 1.5$. Still larger initial masses could be accommodated using larger values for $f_{\rm WR}$, but probably not smaller ones.

A typical ejected mass is 1.7 to 2.0 $M_\odot$ with kinetic energy 0.8 to 1.3 $\times 10^{51}$ erg (Table 3), though a range of both is allowed in individual events (Table 1 and Table 2). These energies and masses agree well with published values (Table 3; Drout et al. 2011; Lyman et al. 2016; Taddia et al. 2018; Prentice et al. 2019). Similarly the rise times, peak times, decline times, spectra, and colors are in good agreement with observations (e.g., Table 3, Table 6, Fig. 7, Fig. 9). The paradigm that most Type IIb, Ib and Ic supernovae originate in mass exchanging binaries with light curves powered by the decay of radioactive ^{56}Ni and ^{56}Co is strongly supported. Depending on the mass loss rates assumed, a subset of Type Ib and Ic supernovae could still come from single stars, but the presupernova mass would need to be less than 5.6 $M_\odot$ (Model He8.0; Ensman & Woosley 1988) in order not to have a light curve that was broader and fainter than common events. Presupernova stars with much greater mass might also be difficult to explode using only neutrinos. Producing such a low mass presupernova star from a massive star that only lost its envelope to radiative winds would require a main sequence mass well in excess of 30 $M_\odot$ and mass loss rates substantially larger than given by Yoon (2017) once the helium core was revealed. While we have attempted no studies of population synthesis, the number of lower mass stars (12 to 30 $M_\odot$) in mass exchanging binaries is probably much greater.

The situation with peak luminosities remains less clear. Our models agree with the bolometric luminosities and absolute magnitudes of most normal Type Ib and Ic supernovae, but fail to explain the brighter events (Fig. 3 and Fig. 4). This is true even when anomalies such as broad-lined supernovae, superluminous supernovae, and gamma-ray burst supernovae are removed from the observational sample and the theoretical maximum ^{56}Ni production is employed in the models. The disagreement exists both for bolometric light curves (Ertl et al. 2020; Lyman et al. 2016; Prentice et al. 2016), as well as peak magnitude distributions (§3.3). Interestingly, the disagreement might not be as great when the comparison is made with specific colors (Fig. 7) or for limited wavelengths (Table 3,Fig. 4 Prentice et al. 2019), though even then quite a few bright events remain unexplained. This suggests that part of the discrepancy with peak bolometric values could be in the way the observers have assembled their bolometric light curves by extrapolations into the infrared and ultraviolet, or by using overly simple models for the light curve.

On the other hand, our treatment of the ultraviolet and infrared light curves in SEDONA is not definitive and 1D models of neutrino transport could be missing important aspects of a putative ultimate 3D treatment. This includes e.g., convection in the neutrino-heated "hot bubble". The models of Ertl et al. (2020) seek to compensate for this by normalizing key parameters to the observed properties of SN 1987A and the Crab, but if, for example, the explosions were to develop earlier and the mass separation was deeper, ^{56}Ni production would be modestly increased. No existing 3D models of which we are aware show such large ^{56}Ni production (greater than 0.15 $M_\odot$) and the tendency of current 3D models

is towards explosion at late times. Nucleosynthetic constraints and the observed masses of neutron stars limit increases in ^{56}Ni production for all but a few rare cases (Ertl et al. 2020). Further work is needed.

We are now confident though that we have calculated the bolometric luminosity for this particular set of models correctly. The results of two very different codes, KEPLER and SEDONA, give essentially the same answer and mixing, though important for the colors and spectrum does not affect the peak bolometric luminosity greatly. A substantial fraction of bright supernovae categorized as normal Type Ib and Ic continue to be mysterious. We encourage observers to undertake new surveys and reanalyze past ones. It may be convenient to avoid constructing "bolometric light curves" and compare instead with theoretical models adjusted to individual passbands now that such predictions are becoming available. We have provided many (Table 5, Table B1, Table B2), and we and others could provide more. Host-galaxy extinction and bolometric corrections seem to have played an important role in some of the observational estimates, and may need to be carefully examined. Major exceptions might be studied for other signs of peculiarity.

In any case, it is risky to arbitrarily vary ^{56}Ni masses and explosion energies for bright supernovae that may not be exploded by neutrinos and hence, whose source of illumination – rotation or radioactive decay – is uncertain. Our predicted maximum bolometric luminosity remains $10^{42.5}$ erg s^{-1}. Our maximum explosion energy is 2×10^{51} erg and maximum ^{56}Ni mass is 0.15 M$_\odot$. The brightest B, V, R, and I peak absolute magnitudes are -17.2, -17.8, -18.0, and -18.1. The V limit is the best determined.

As noted by others (Dessart et al. 2016; Khatami & Kasen 2019), Arnett's rule does not work well for Type Ib and Ic supernovae (§A). Dessart et al. (2016) found that the ^{56}Ni mass inferred for a given peak luminosity overestimated the actual value by a factor, on the average, of 1.41 ± 0.072. Here, possibly because of different assumptions about mixing explosion energy, and opacity, we find a smaller discrepancy 1.30 ± 0.095 (§A.2). Starting with the analytic treatment of Khatami & Kasen (2019), we derive a more accurate way of determining the ^{56}Ni mass using Khatami's characteristic parameter, β, to describe a given model set (§A).

While the deficiency of bright events is interesting, it should not be overlooked that our models do agree with the observed properties of many observed events. Detailed comparisons have been made with six of them: SN 2007Y, SN 2007gr, SN 2009jf, LSQ13abf, SN 2008D, and SN 2010X, and are largely successful. The models do display deficiencies in the ultraviolet and infrared that increase with time 10 to 20 days post-peak. We confirm and explain, on the basis of our models (§3.4), the pinch seen in the color index $(V - R)$ 10 days after V peak. Drout et al. (2011) measured a mean value of 0.26 ± 0.06 mag for this quantity. Dessart et al. (2016) calculated a mean value of 0.33 ± 0.035 mag. We calculate a median value here of 0.34 mag for our standard $f_{\rm WR} = 1$ models and 0.29 mag for the models with greater mass loss, $f_{\rm WR} = 1.5$. These and other predictions for similar pinches in many other color indices are given in Table 5 and Fig. 9. Given the robustness of this number and other indices as a measure of temperature at a specific epoch, they may prove useful in calculating the host-galaxy extinction (Stritzinger et al. 2018b). We also note that it is not just the colors, but the spectrum itself that appears to converge on a standard value 10 days after the explosion (Fig. 13).

Fig. 5 and Fig. 6 show the light curves and spectra of two typical models from our survey, Models He4.50 and He8.00x2. Despite a very different presupernova evolution, these stars ejected similar amounts of mass and, by construction, had the same ^{56}Ni masses and explosion energies. Even with very different compositions, their bolometric light curves are almost identical. Except at early times their colors and spectra are also nearly indistinguishable. While some variation in ^{56}Ni synthesis and explosion energy is naturally expected, the supernova depends much more on the presupernova mass than how the star got there. Unless one is interested in colors at early times, surveys with variable mass loss rates may not be necessary in certain situations. The natural chaos in presupernova core structure (Sukhbold et al. 2018) may dominate over the smaller effects of variable composition. There are two clear exceptions to this: 1) the weighting assigned to the event when computing averages depends on the zero age main sequence mass which will be different for different mass loss prescriptions; and 2) loss of most of the helium envelope will make it difficult to produce a supernova that is spectroscopically Type Ib.

In addition to ordinary Type Ib and Ic supernovae, we also studied the properties of several explosions for masses that lay outside our standard range ($M_{\rm preSN}$ = 2.2 - 5.6 M$_\odot$). Models with radius expansion, either due to the low mass of the star or a silicon flash a few weeks before core collapse, can produce events similar to LSQ13abf (Fig. 17), SN 2008D (Fig. 18), and SN 2010X (Fig. 19 and Fig. 20). Interestingly, the available r-band data is, by itself, consistent with two solutions for SN 2010X. For Model He2.50, the light curve has a peak lasting about two weeks resulting from the release of shock deposited energy in a blue supergiant envelope by helium recombination. On the peak, radioactivity plays little role. This is a solution also explored by Kleiser et al. (2018a). Ours differs in that the large radius is due to a silicon flash 19 days prior to iron core collapse. Even so, a good fit to duration and luminosity required an artificial, though not unrealistic increase in the explosion kinetic energy. One attractive feature of this model is that a slight variation of the silicon flash energetics might also produce other supernovae with rapid rises and declines and weak radioactive tails, e.g., SN 2002bj. Other similar double-peaked light curves have been reported (Gorbikov et al. 2014; Taddia et al. 2016) and attributed to radius expansion.

A second solution, similar to that suggested by Kasliwal et al. (2010) themselves and also studied by Tauris et al. (2013), Tauris et al. (2015), and Moriya et al. (2017), has SN 2010X illuminated at peak by radioactive decay. Our standard Model He2.60 (Fig. 20) produces a distinctive double-peaked light curve in the r-band that should exist in nature, but does not look like SN 2010X. Several modifications to the ejected mass, explosion energy, and ^{56}Ni mass are required to achieve a good fit, but they are again reasonable modifications. The most successful Model He2.60m differs from previous studies (e.g.,

Moriya et al. 2017) by happening in a progenitor with much larger radius and is therefore brighter early on. Such a large presupernova radius would require a much wider binary system, but loss of the hydrogen envelope when a red supergiant forms near helium ignition and a blue supergiant structure at the presupernova stage are not incompatible.

Relative to SN 2010X the overall r-band light curve is better fit by the recombination model, especially at late times (Fig. 19 and Fig. 20). The low nickel mass ($\lesssim$0.01 $M_\odot$) and explosion energy are also consistent with expectations for a star of such small mass. On the other hand, the velocity is a bit low unless the ejected mass is further artificially reduced, and the properties of the silicon flash are uncertain. The high luminosity and very blue spectrum prior to peak may also be difficult to reconcile with observations of SN 2010X. The radioactive model requires a very low ejected mass that contains a substantial amount of ^{56}Ni ($\sim$ 0.03 $M_\odot$). This may be difficult to achieve in a self-consistent neutrino-powered explosion (Ertl et al. 2020), but for now we favor this model for SN 2010X based on its spectrum near peak light (Fig. 21 here and Fig. 2 of Kasliwal et al. 2010), but the issue needs further study.

Very massive explosions produce faint, red, long transients (Fig. 22 and Fig. 23). SN 2013bb is not a bad match to Model He12.00 (§5) and such faint, long transients could have been selected against in past surveys. Given their high mass, they would be relatively rare. It is also possible that stars of such great mass have explosions augmented by non-neutrino sources (Ertl et al. 2020).

All explosion models, spectra, light curves and tables in this paper are available on request.

ACKNOWLEDGMENTS

We have benefited greatly, both in understanding and in privately supplied data, from interactions with several observers. Max Stritzinger provided directions for using the Carnegie data set and the data used in Fig. 3, Fig. 7, Fig. 12, Fig. 14, and Fig. 17. Simon Prentice helped us on many occasions with insights and data. He provided the data in Fig. 4, Fig. 15 and Fig. 16. Mansi Kasliwai provided data for Fig. 19 and Fig. 20. Stefano Valenti provided infrared data for SN 2007gr. Mark Phillips, Francesco Taddia, Maria Drout, Isaac Shivvers, and Alex Filippenko provided valuable assistance in understanding and using their works. Christopher Kochanek helped us to understand the complicated landscape of photometric systems. At Santa Cruz this work was partly supported by NASA NNX14AH34G. TS was supported by NASA through a NASA Hubble Fellowship grant #60065868 awarded by the Space Telescope Science Institute, which is operated by the Association of Universities for Research in Astronomy, Inc., for NASA, under contract NAS5-26555. The authors acknowledge use of the LUX supercomputer at UC Santa Cruz, funded by NSF MRI grant AST 1828315.

APPENDIX

A. ANALYTIC FITS TO THE BOLOMETRIC LIGHT CURVE AND ARNETT'S RULE

A.1. *^{56}Ni and the Peak Luminosity*

Khatami & Kasen (2019) have recently derived analytic approximations for the light curves of stripped-envelope supernova. They find that recombination and the spatial distribution of heating modify the peak of the light curve and that these effects can be accounted for by varying a single dimensionless parameter, β, which is a measure of mixing. The parameter β also captures some of the effects of recombination on the opacity. In particular, they find for Type I supernovae heated by the decay of ^{56}Ni and ^{56}Co

$$L_{\rm peak} \;=\; 2\epsilon_{\rm Ni} M_{\rm Ni} F(t_{\rm peak}, \beta) \tag{A1}$$

where

$$F(t_{\rm peak}, \beta) \;= \frac{k_1\, g(\tau_{\rm Ni}) \;+\; k_2\, g(\tau_{\rm Co})}{\beta^2 \tau_{\rm Ni}^2} \tag{A2}$$

and

$$k_1 \;=\; 1 - r\,\frac{\epsilon_{\rm Co}}{\epsilon_{\rm Ni}} \tag{A3}$$

$$k_2 \;=\; r\left(\frac{\epsilon_{\rm Co}}{\epsilon_{\rm Ni}}\right)\left(\frac{t_{\rm Co}}{t_{\rm Ni}}\right)^2 \tag{A4}$$

$$r \;=\; \frac{t_{\rm Co}}{t_{\rm Co} - t_{\rm Ni}} \tag{A5}$$

$$g(\tau_i) \;=\; 1 - (1+\beta\tau_i)e^{-\beta\tau_i}. \tag{A6}$$

Here $M_{\rm Ni}$ is the initial mass of ^{56}Ni; $t_{\rm Co} = 111.3$ days and $t_{\rm Ni} = 8.77$ days are the mean lives of ^{56}Co and ^{56}Ni; $\tau_{\rm Co} = t_{\rm peak}/t_{\rm Co}$ and $\tau_{\rm Ni} = t_{\rm peak}/t_{\rm Ni}$ where $t_{\rm peak}$ is the time of bolometric light curve peak; and $\epsilon_{\rm Ni} = 3.90 \times 10^{10}$ erg g^{-1} s^{-1} and $\epsilon_{\rm Co} = 6.78 \times 10^9$ erg g^{-1} s^{-1} are the energy yields from ^{56}Ni and ^{56}Co decay. Typos in the values Khatami & Kasen (2019) published for k_1, k_2, and $g(\tau_{\rm Ni})$ have been repaired. Evaluating fixed constants gives $k_1 = 0.811$ and $k_2 = 30.4$. For comparison, the energy from radioactive decay at peak, if all energy were trapped, is

$$L_{\rm heat} \;=\; M_{\rm Ni}\left[(\epsilon_{\rm Ni} - r\epsilon_{\rm Co})e^{-\tau_{\rm Ni}} \;+ r\epsilon_{\rm Co}e^{-\tau_{\rm Co}}\right]. \tag{A7}$$

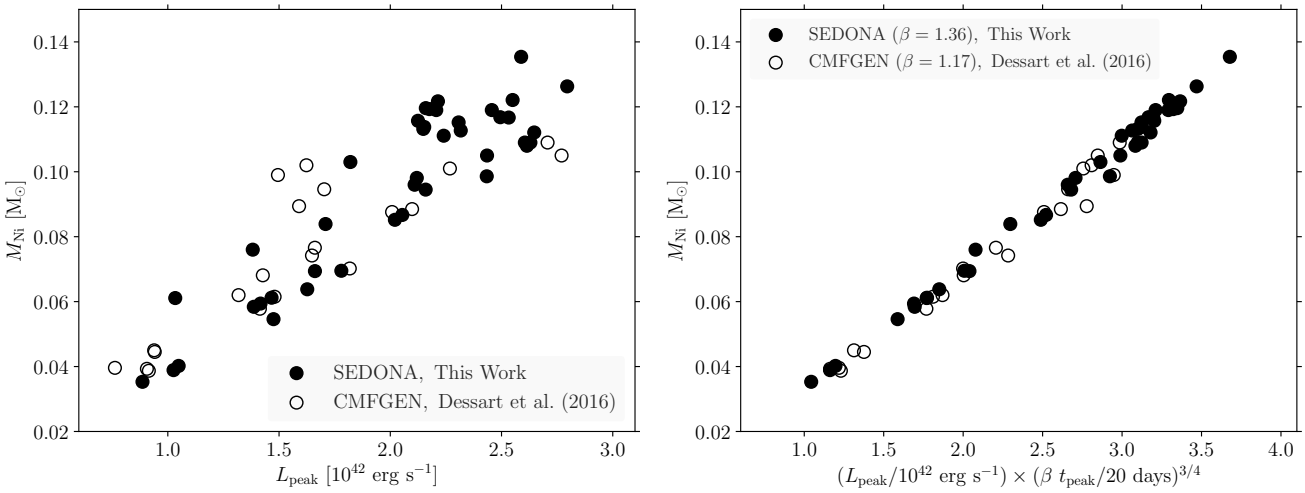

FIG. A1.— Bolometric luminosity at peak vs the initial mass of ^{56}Ni produced in the explosion. Filled circles are from the present study and open ones are from Dessart et al. (2016). (top:) The unmodified dependence. (bottom:) The comparison is greatly improved if the luminosity at peak is scaled by $(\beta t_{\rm peak})^{3/4}$ where $\beta = 1.17$ for the Dessart set and 1.36 for the present work. Four of the 27 models calculated by Dessart are not included because they produced more than 0.2 M$_\odot$ of ^{56}Ni and are not regarded as physical.

Based on models, Khatami & Kasen (2019) approximated $\beta \approx 4/3(1 + r_s^4)$ where r_s is the ratio of the radius of the homogeneously mixed region containing ^{56}Ni to the "radius of the ejecta", which is the maximum velocity of the ejecta times the age. $r_s = 0$ corresponds to no mixing and $r_s = 1$ to complete mixing. While a mathematically useful simplification, there are several difficulties in applying this definition to an actual model. First the radius of the ejecta is poorly defined when a shock wave in the outer layers can result in extremely high velocity in a small amount of mass. We can attempt to get around that by defining a cutoff at say, 99% of the mass. Second, as Khatami & Kasen (2019) discuss, recombination and other alterations to the opacity can change the value of β and its interpretation. In particular, recombination can reduce β. Dessart et al. (2016) discuss the complicated time and spatial dependence of the opacity, even in the absence of recombination. Finally, prescriptions for mixing are not so simple as homogenizing the composition inside a given velocity. There is an appreciable gradient in ^{56}Ni even in the mixed region (Fig. 1).

If we examine a typical model, He6.00, in some detail, the velocity at the 99% mass point is 13,900 km s^{-1}. At the 95% point it is 9890 km s^{-1}. The velocity containing 99% of the ^{56}Ni in the mixed model is 6300 km s^{-1}, but the velocity containing 50% of the ^{56}Ni is only 3570 km s^{-1}. The dimensionless radius would thus be somewhere between 0.26 and 0.64 and β between 1.34 and 1.55, without corrections for recombination. Probably the 50% mixing radius is more appropriate, so values of β less than about 1.4 are preferred. While some might regard our models as "well mixed", the ^{56}Ni actually remains centrally concentrated. In a version of He6.00 with no mixing at all (Fig. 1), the velocity at the outer edge of the ^{56}Ni was already 2700 km s^{-1}, or 75% of the radius of the half-nickel point in the mixed production model.

The average β for the (Dessart et al. 2016) data set is 1.17 (close to the 9/8 cited by Khatami & Kasen 2019). For our new models the average β is 1.36. There is a tendency for the lighter models with thick helium shells to have a smaller value of β, around 1.3 in the new set, while the heavier ones have $\beta \approx 1.4$.

For this range of β and a range of $t_{\rm peak}$ from 15 to 40 days, $F(t_{\rm peak}, \beta)$ in eq. (A1) can be fit to an accuracy of 2% by

$$F(t_{\rm peak}, \beta) \ = 0.1515 \left(\frac{\beta}{1.33} \frac{t_{\rm peak}}{20 \text{ days}} \right)^{-0.75}, \tag{A8}$$

so that the luminosity at peak is

$$L(t_{\rm peak}) \ = \ 2.35 \times 10^{42} \frac{M_{Ni}}{0.10 \text{ M}_\odot} \left(\frac{\beta}{1.33} \ \frac{t_{\rm peak}}{20 \text{ days}} \right)^{-0.75} \text{ erg s}^{-1}. \tag{A9}$$

Because $t_{\rm peak}$ is not always easy to determine observationally, it is possible to substitute other similar variables such as the decline rate post-maximum or the width of the peak. Fig. A2 shows that for a given value of β, a measurement of ΔM_{15} in the visual or red band can constrain the peak of the bolometric light curve for the present models to about a day, or $\sim 5\%$. Taken to a power 0.75, this means the ^{56}Ni mass can be determined by the peak luminosity to about 4%. The scaled peak, $\beta t_{\rm peak}$ is a measure of when the energy deposited by radioactive decay balances the light emitted by the star, i.e., the time derivative of the internal energy is zero (Khatami & Kasen 2019). It is a better choice for comparison with the decay time. Without the multiplication by β the Dessart et al. (2016) data is systematically higher than for the new models. Part of the remaining scatter results from the choice of a single β to characterize the two data sets. The models of Dessart et al. (2016) spanned a larger range of explosion energies and mixing prescriptions than the present study. The larger range also resulted from a broad choice of uncertain parameters. For example, we

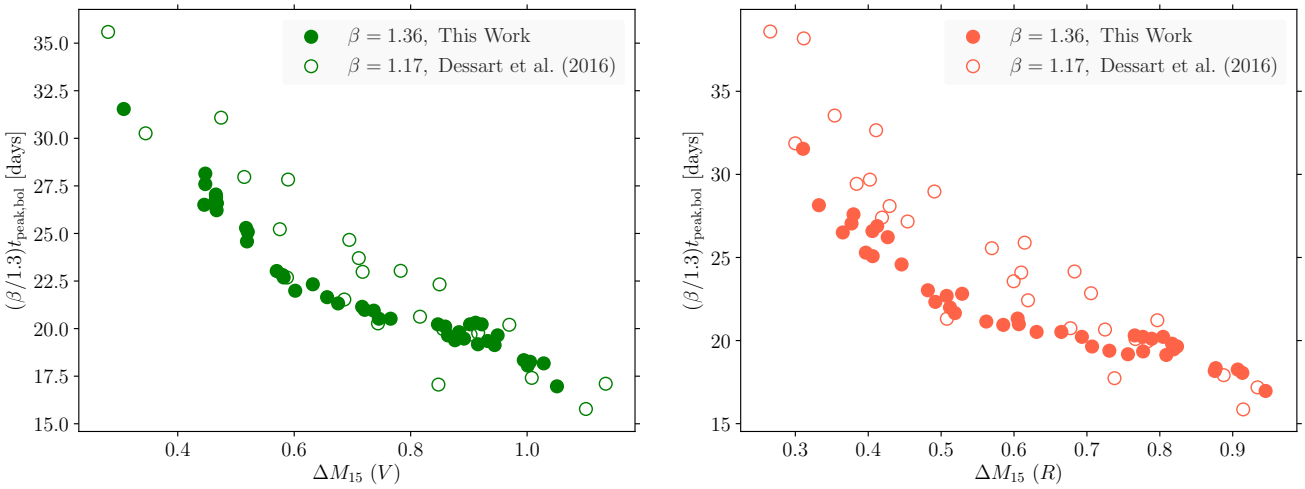

FIG. A2.— The scaled time of bolometric peak, $\beta/1.3$ times t_{peak} is plotted against the decline in the V magnitude 15 days after V-band peak (top) and decline in R-band (bottom). For the Dessart et al. data set $\beta = 1.17$; for the current models $\beta = 1.36$. A larger spread is seen in the Dessart et al. models which included a broader range of mixing prescriptions and explosion energies than the current study.

do not consider the higher energy, large ^{56}Ni-producing events, since our neutrino-powered explosions do not produce them. Mixing here also has a more physical, though still uncertain basis (§2.3). A relation between $t_{\rm peak}$ bolometric and ΔM_{15} in the B band shows greater scatter, perhaps reflecting inaccuracies in our B-band determination, and is not recommended. We recommend that observers assume a value $\beta = 1.3$ when using these figures. This gives slightly greater weight to our models ($\beta = 1.36$) than those of Dessart et al ($\beta = 1.17$).

All these approximations are derived from fitting models for Type Ib and Ic supernovae whose light curves are powered by the decay of ^{56}Ni. Without further study, they are not directly applicable to other situations.

A.2. *Arnett's Rule*

Originally derived with Type Ia supernovae in mind, but since often applied to all manner of Type I supernovae, Arnett's Rule (Arnett 1982) says the the bolometric luminosity, at peak, is equal to the current power being generated by the decay of ^{56}Ni and ^{56}Co. This radioactive power includes all radiation, trapped and untrapped. The Rule is often used to infer the mass of ^{56}Ni made in an explosion whose bolometric luminosity at peak has been determined (e.g., Drout et al. 2011). While a very good approximation for Type Ia supernovae (e.g., Stritzinger et al. 2006), previous studies have shown that the rule leads to a substantial overestimate of the ^{56}Ni actually required to power Type Ib and Ic supernovae (Dessart et al. 2015, 2016). The reasons for deviations and discussion of the restrictions for the rule's use have been discussed in the context of a more general analytic derivation by Khatami & Kasen (2019). The rule breaks down because of violations of the assumptions in its original variation, namely constant opacity and self-similarity of the energy density profile.

Dessart et al. (2016) also examined the relation between luminosity and radioactive power at peak for a grid of Type Ib and Ic supernova light curves calculated from current models of the explosion using the CMFGEN code (Hillier & Dessart 2012).

B. MODEL PROPERTIES

Here we provide additional details for all of the standard Type Ib and Ic models that used the W18 central engine (Ertl et al. 2020) and the standard Yoon (2017) mass loss rates with $f_{\rm WR} = 1$. The peak luminosities and magnitudes (listed in Table B1) and their corresponding peak times (Table B2) are measured using a third degree polynomial fit to the brightest 5 points in the light curve. The rise ($t_{-1/2}$) and decline ($t_{+1/2}$) times are measured between peak and 50% of the peak for luminosity, and between peak and peak plus 0.75 magnitude for the broad band filters (e.g., Ho et al. 2020). The decline rates ΔM_{15} (Table B3) are measured between peak and 15 days post peak. The bolometric and multiband light curves for our entire set of models are available on request.

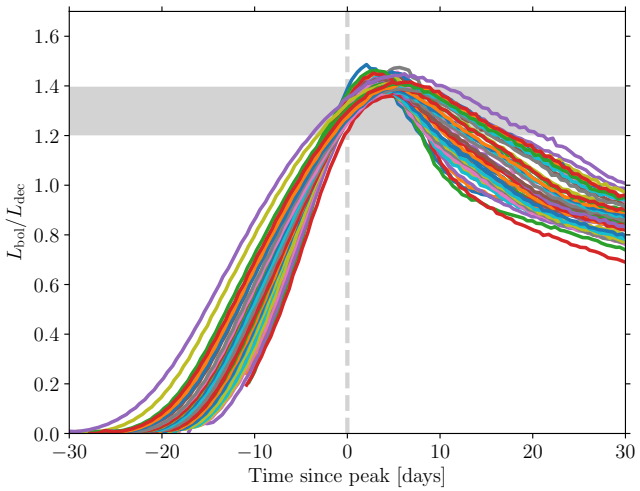

FIG. A3.— Ratio of the bolometric luminosity to current total power from the decay of ^{56}Ni and ^{56}Co as a function of time. Time zero is adjusted here to be the peak of the bolometric light curve. The average ratio and error bar, 1.30 ± 0.095, are indicated by the gray band. The ratio is sensitive to the timing of the the peak, but "Arnett's Rule" significantly overestimates the amount of ^{56}Ni required to explain the observed light curves of Type Ib and Ic supernovae. A similar study by Dessart et al. (2016) found a ratio at peak of 1.41 ± 0.072.

TABLE B1. PEAK LUMINOSITIES AND MAGNITUDES ($f_{\rm WR} = 1$)

$M_{\rm He,i}$ [$M_\odot$]	log $L_{\rm bol}$ [erg s^{-1}]	log L_{4-10k} [erg s^{-1}]	$U_{\rm peak}$	$B_{\rm peak}$	$V_{\rm peak}$	$R_{\rm peak}$	$I_{\rm peak}$	$u_{\rm peak}$	$g_{\rm peak}$	$r_{\rm peak}$	$i_{\rm peak}$	$z_{\rm peak}$
2.70	41.89	41.78	-16.26	-15.85	-16.41	-16.53	-16.73	-15.33	-16.12	-16.39	-16.23	-16.46
2.80	41.87	41.76	-15.81	-15.74	-16.35	-16.52	-16.70	-14.87	-16.03	-16.38	-16.21	-16.48
2.90	42.02	41.92	-16.23	-16.27	-16.79	-16.86	-17.02	-15.19	-16.53	-16.74	-16.51	-16.80
3.20	42.21	42.11	-16.59	-16.77	-17.30	-17.34	-17.50	-15.51	-17.05	-17.22	-16.99	-17.38
3.30	42.17	42.07	-16.50	-16.63	-17.16	-17.24	-17.40	-15.42	-16.90	-17.10	-16.91	-17.26
3.40	42.01	41.91	-15.86	-16.14	-16.73	-16.87	-17.03	-14.76	-16.42	-16.73	-16.57	-16.88
3.50	42.02	41.92	-15.79	-16.13	-16.75	-16.90	-17.07	-14.65	-16.43	-16.76	-16.61	-16.91
3.60	41.94	41.84	-15.48	-15.89	-16.55	-16.73	-16.89	-14.31	-16.20	-16.58	-16.46	-16.72
3.70	42.21	42.11	-16.54	-16.70	-17.25	-17.39	-17.54	-15.46	-16.98	-17.25	-17.06	-17.40
3.80	42.25	42.15	-16.66	-16.80	-17.35	-17.49	-17.63	-15.58	-17.07	-17.35	-17.16	-17.50
3.90	42.14	42.04	-16.30	-16.48	-17.05	-17.25	-17.40	-15.21	-16.74	-17.09	-16.96	-17.24
4.00	42.16	42.06	-16.44	-16.55	-17.11	-17.29	-17.45	-15.36	-16.81	-17.14	-16.99	-17.30
4.10	42.14	42.04	-16.19	-16.44	-17.04	-17.23	-17.39	-15.07	-16.71	-17.08	-16.94	-17.24
4.20	42.22	42.12	-16.45	-16.65	-17.25	-17.43	-17.58	-15.35	-16.92	-17.27	-17.13	-17.44
4.30	42.31	42.21	-16.79	-16.92	-17.50	-17.66	-17.80	-15.71	-17.19	-17.51	-17.33	-17.65
4.40	42.31	42.20	-16.74	-16.88	-17.47	-17.64	-17.78	-15.66	-17.15	-17.48	-17.32	-17.64
4.50	42.39	42.29	-16.95	-17.09	-17.70	-17.83	-17.98	-15.87	-17.37	-17.69	-17.48	-17.83
4.62	42.42	42.32	-17.07	-17.18	-17.78	-17.92	-18.06	-16.01	-17.47	-17.78	-17.57	-17.91
4.75	42.42	42.32	-17.03	-17.16	-17.77	-17.91	-18.05	-15.95	-17.45	-17.77	-17.56	-17.91
4.88	42.42	42.31	-16.95	-17.14	-17.77	-17.91	-18.05	-15.87	-17.42	-17.77	-17.56	-17.91
5.00	42.42	42.32	-17.02	-17.16	-17.78	-17.93	-18.07	-15.94	-17.44	-17.78	-17.58	-17.93
5.13	42.39	42.28	-16.82	-17.02	-17.67	-17.84	-17.97	-15.73	-17.32	-17.68	-17.50	-17.85
5.25	42.33	42.23	-16.61	-16.86	-17.53	-17.71	-17.85	-15.49	-17.16	-17.55	-17.39	-17.73
5.38	42.45	42.34	-17.06	-17.19	-17.83	-17.99	-18.12	-15.98	-17.47	-17.84	-17.66	-18.00
5.50	42.40	42.30	-16.72	-16.99	-17.70	-17.91	-18.03	-15.59	-17.29	-17.74	-17.60	-17.91
5.63	42.32	42.22	-16.53	-16.81	-17.50	-17.69	-17.83	-15.40	-17.11	-17.53	-17.39	-17.70
5.75	42.33	42.22	-16.55	-16.81	-17.50	-17.69	-17.82	-15.41	-17.12	-17.53	-17.39	-17.71
5.88	42.40	42.29	-16.83	-17.03	-17.68	-17.87	-17.99	-15.73	-17.31	-17.71	-17.56	-17.88
6.00	42.23	42.12	-16.05	-16.50	-17.24	-17.46	-17.61	-14.86	-16.83	-17.29	-17.20	-17.45
6.13	42.40	42.30	-16.81	-17.03	-17.69	-17.89	-18.02	-15.68	-17.32	-17.73	-17.58	-17.89
6.25	42.39	42.28	-16.72	-16.98	-17.65	-17.85	-17.98	-15.60	-17.27	-17.69	-17.55	-17.85
6.38	42.36	42.25	-16.59	-16.89	-17.58	-17.79	-17.92	-15.45	-17.20	-17.63	-17.50	-17.79
6.50	42.35	42.24	-16.48	-16.83	-17.54	-17.77	-17.90	-15.31	-17.14	-17.60	-17.49	-17.76
6.63	42.36	42.25	-16.56	-16.88	-17.57	-17.79	-17.92	-15.40	-17.19	-17.63	-17.51	-17.78
6.75	42.13	42.02	-15.64	-16.23	-16.97	-17.22	-17.38	-14.41	-16.57	-17.04	-16.98	-17.21
6.88	42.33	42.22	-16.38	-16.77	-17.48	-17.71	-17.84	-15.19	-17.09	-17.54	-17.44	-17.71
7.00	42.33	42.22	-16.33	-16.76	-17.48	-17.72	-17.85	-15.13	-17.07	-17.55	-17.45	-17.70
7.13	42.41	42.30	-16.73	-17.01	-17.68	-17.91	-18.04	-15.57	-17.30	-17.74	-17.63	-17.92
7.25	42.26	42.14	-15.94	-16.52	-17.27	-17.52	-17.68	-14.72	-16.85	-17.34	-17.28	-17.51
7.38	42.34	42.23	-16.33	-16.77	-17.49	-17.74	-17.87	-15.14	-17.09	-17.56	-17.48	-17.72
7.50	42.33	42.21	-16.24	-16.71	-17.45	-17.69	-17.84	-15.02	-17.04	-17.52	-17.44	-17.68
7.63	42.34	42.22	-16.25	-16.74	-17.47	-17.72	-17.85	-15.04	-17.06	-17.54	-17.47	-17.70
7.75	42.34	42.23	-16.27	-16.75	-17.49	-17.74	-17.89	-15.05	-17.08	-17.56	-17.49	-17.72
7.88	42.33	42.21	-16.17	-16.70	-17.46	-17.71	-17.86	-14.95	-17.03	-17.54	-17.47	-17.69
8.00	42.01	41.88	-14.85	-15.68	-16.59	-16.91	-17.10	-13.58	-16.09	-16.71	-16.73	-16.87
12.0	42.06	41.92	-14.23	-15.61	-16.69	-17.03	-17.23	-12.72	-16.10	-16.83	-16.86	-17.00
19.0	42.12	41.99	-14.35	-15.80	-16.82	-17.17	-17.40	-12.87	-16.28	-16.98	-17.01	-17.19

NOTE. — L_{4-10k} covers only 4000 – 10000 Å. $UBVRI$ and $ugriz$ magnitudes are based on Vega– and AB–systems respectively. For the peak, rise, and decline times for each model see Table B2.

TABLE B2. RISE, DECLINE, AND PEAK TIMES ($f_{\rm WR} = 1$)

$M_{\rm He,i}$ [$M_\odot$]	$t_{-1/2}$ [days]					$t_{\rm peak}$ [days]					$t_{+1/2}$ [days]				
	$L_{\rm bol}$	B	V	R	I	$L_{\rm bol}$	B	V	R	I	$L_{\rm bol}$	B	V	R	I
2.70	15.5	12.4	8.4	7.9	7.7	15.7	13.1	16.2	16.5	16.5	10.0	8.4	8.7	10.2	11.7
2.80	15.9	13.3	9.3	8.8	8.3	16.1	14.0	16.5	17.2	16.8	11.1	8.6	9.7	10.2	12.3
2.90	15.6	7.6	8.6	9.3	9.6	15.8	13.8	16.0	17.4	17.8	10.6	8.0	9.1	10.0	12.5
3.20	15.0	7.5	8.6	10.9	10.6	16.1	13.8	16.4	19.2	19.0	12.0	9.1	10.0	10.5	14.0
3.30	9.3	7.4	9.1	11.5	10.0	17.3	15.0	17.5	20.6	19.0	12.7	8.9	10.3	10.3	15.5
3.40	10.2	7.9	10.1	10.7	11.1	18.6	15.8	18.7	19.8	20.2	13.3	9.5	10.4	12.4	15.6
3.50	9.7	7.8	10.0	10.6	10.9	18.4	16.0	18.8	19.8	20.0	14.1	9.8	10.8	12.7	16.4
3.60	10.1	8.1	10.2	11.7	11.0	19.2	16.8	19.3	21.2	20.4	15.5	10.4	11.8	13.0	18.0
3.70	10.1	7.1	9.5	11.7	13.3	18.6	15.3	18.4	21.5	22.8	14.0	10.0	11.5	11.4	13.7
3.80	10.4	6.7	9.3	11.7	10.4	18.8	14.8	18.0	21.3	19.9	13.5	10.2	11.6	11.1	16.5
3.90	10.9	7.6	10.5	12.7	12.9	20.0	16.4	19.6	22.8	22.8	16.8	11.0	13.2	13.2	17.9
4.00	12.2	7.5	11.9	12.3	12.4	21.0	15.8	20.9	22.3	22.4	14.9	11.1	11.3	13.2	17.9
4.10	12.5	7.6	11.9	12.2	12.4	21.7	16.5	21.2	22.3	22.4	15.1	11.3	11.9	14.1	18.3
4.20	11.9	7.4	11.3	12.7	12.1	21.0	16.0	20.4	22.8	22.1	15.2	11.1	12.0	12.9	17.6
4.30	11.7	7.8	12.3	11.9	10.9	20.8	16.3	21.6	22.4	21.2	15.3	10.7	11.0	13.7	19.8
4.40	11.8	8.1	12.1	11.9	11.9	20.9	16.5	21.2	22.3	22.3	15.6	10.7	11.6	13.9	18.9
4.50	10.8	7.4	10.5	10.9	10.1	19.5	15.3	19.4	20.8	20.0	14.3	10.2	11.3	13.1	18.2
4.62	10.9	7.3	10.4	11.3	10.4	19.7	15.3	19.3	21.4	20.4	15.1	10.7	12.2	13.4	19.0
4.75	10.8	8.3	10.5	10.7	10.1	19.5	16.2	19.3	20.7	20.0	15.2	9.9	12.1	14.2	19.9
4.88	11.1	8.0	10.6	11.5	10.4	20.0	16.0	19.6	21.6	20.4	15.5	10.5	12.4	13.8	20.5
5.00	11.2	8.6	10.8	10.9	10.4	20.1	16.6	19.8	21.1	20.5	16.0	10.4	12.7	15.0	20.8
5.13	11.5	8.2	10.7	12.2	10.8	20.6	16.3	19.8	22.6	21.0	16.8	11.6	14.0	14.5	22.6
5.25	11.8	8.9	12.0	11.5	11.0	21.0	17.2	21.2	21.8	21.1	17.4	11.5	13.6	16.2	22.9
5.38	12.1	8.5	11.9	11.8	12.5	21.2	16.6	21.0	22.3	22.8	18.0	12.1	14.1	16.7	23.6
5.50	12.6	9.3	11.3	11.8	12.2	22.0	17.6	20.5	22.5	22.4	18.5	12.1	15.7	17.4	26.2
5.63	12.6	8.6	11.9	13.2	12.3	22.0	17.2	21.3	23.6	22.4	18.3	12.3	14.6	16.0	23.5
5.75	12.7	8.6	11.7	13.2	12.0	22.3	17.3	21.4	23.8	22.2	19.3	12.9	15.7	17.0	25.9
5.88	12.5	8.3	12.2	13.4	12.4	22.0	17.0	21.7	24.2	22.7	19.8	12.9	15.5	17.0	27.0
6.00	13.6	9.3	13.4	13.8	14.1	24.0	18.8	23.6	24.8	24.9	21.6	14.1	16.8	19.8	29.0
6.13	12.9	8.9	11.7	13.4	14.7	22.7	17.9	21.6	24.4	25.2	20.5	13.0	17.1	18.2	26.8
6.25	13.2	8.8	13.1	13.3	12.9	23.2	18.0	23.1	24.3	23.4	20.7	13.4	16.1	19.0	29.6
6.38	13.5	9.1	12.5	13.5	13.5	23.7	18.6	22.6	24.6	24.0	20.7	13.1	17.2	19.0	29.5
6.50	13.4	7.9	13.2	14.0	16.0	24.0	17.8	23.6	25.4	26.8	21.5	14.4	17.2	19.1	28.1
6.63	13.5	8.8	12.2	14.1	13.0	24.2	18.8	22.8	25.6	24.0	21.8	13.7	18.4	19.4	32.3
6.75	14.8	8.9	14.6	17.2	16.6	27.0	20.8	26.7	29.8	29.3	28.4	17.2	21.7	23.7	35.8
6.88	14.3	9.3	13.5	15.4	16.0	25.8	20.2	24.8	27.6	27.8	24.6	15.0	19.7	21.4	32.5
7.00	13.6	8.7	13.4	15.8	13.6	25.2	19.6	25.0	28.1	25.5	25.1	16.0	19.6	21.0	35.2
7.13	13.9	8.6	13.6	15.0	13.4	25.2	19.3	24.8	27.2	25.0	24.0	15.2	19.3	21.2	35.0
7.25	16.8	10.0	14.7	16.3	17.1	29.9	22.4	27.7	30.0	30.6	27.3	17.9	23.2	26.1	38.3
7.38	14.9	9.9	13.2	15.9	17.0	26.9	21.2	25.1	28.6	29.2	25.1	15.6	21.4	22.2	34.7
7.50	14.4	8.8	14.7	16.2	16.4	26.6	20.3	26.8	29.2	29.0	26.4	17.0	20.4	22.7	35.5
7.63	14.8	9.7	14.2	17.1	14.3	27.1	21.4	26.4	30.2	27.1	26.8	16.3	21.4	22.0	37.4
7.75	15.5	9.0	14.8	16.0	16.2	28.0	20.8	27.2	29.2	29.2	25.9	17.1	20.7	23.6	35.2
7.88	15.0	9.5	13.6	16.7	15.7	27.9	21.6	26.4	30.2	29.0	26.7	17.1	22.4	23.1	36.6
8.00	17.6	11.0	15.3	17.5	19.0	32.6	25.2	29.8	32.6	34.4	30.2	20.3	25.5	27.9	40.0
12.00	19.6	12.8	19.4	20.4	23.1	39.2	32.8	39.2	40.2	43.2	40.6	27.3	31.3	37.1	52.0
19.00	24.5	16.6	23.4	28.2	27.9	47.4	39.9	46.5	51.5	51.7	43.1	29.6	35.4	37.5	59.4

NOTE. — The rise ($t_{-1/2}$) and decline ($t_{+1/2}$) times are the intervals required for a 0.75 change in magnitude (i.e., 50% change in flux) relative to their peak values.

TABLE B3. ΔM_{15} DECLINE RATES ($f_{\rm WR} = 1$)

$M_{\rm He,i}$ [$M_\odot$]	ΔB_{15}	ΔV_{15}	ΔR_{15}	ΔI_{15}	Δg_{15}	Δr_{15}	Δi_{15}	Δz_{15}
2.70	1.35	1.15	1.10	0.92	1.15	1.16	0.99	0.62
2.80	1.30	1.10	1.11	0.86	1.12	1.18	0.98	0.61
2.90	1.45	1.17	1.10	0.87	1.24	1.18	1.00	0.59
3.20	1.49	1.12	1.07	0.78	1.28	1.15	0.93	0.64
3.30	1.47	1.09	1.05	0.73	1.26	1.09	0.90	0.64
3.40	1.37	1.05	0.92	0.74	1.15	0.98	0.88	0.59
3.50	1.33	1.04	0.89	0.70	1.15	0.98	0.90	0.59
3.60	1.26	0.95	0.88	0.64	1.07	0.90	0.85	0.54
3.70	1.37	0.99	0.97	0.77	1.19	1.05	0.83	0.60
3.80	1.34	0.99	1.00	0.68	1.20	1.08	0.83	0.62
3.90	1.24	0.86	0.85	0.66	1.02	0.93	0.75	0.54
4.00	1.22	0.97	0.86	0.66	1.02	0.94	0.76	0.56
4.10	1.20	0.93	0.81	0.63	0.99	0.89	0.73	0.55
4.20	1.19	0.94	0.86	0.65	1.01	0.88	0.73	0.55
4.30	1.24	0.99	0.82	0.60	1.03	0.89	0.68	0.54
4.40	1.23	0.96	0.82	0.62	1.02	0.83	0.67	0.51
4.50	1.29	1.00	0.87	0.63	1.13	0.96	0.73	0.55
4.63	1.25	0.95	0.85	0.61	1.08	0.94	0.60	0.54
4.75	1.28	0.95	0.82	0.57	1.11	0.91	0.56	0.54
4.88	1.22	0.91	0.83	0.56	1.02	0.92	0.54	0.51
5.00	1.24	0.89	0.75	0.55	1.02	0.82	0.54	0.50
5.13	1.12	0.80	0.78	0.52	1.00	0.84	0.62	0.49
5.25	1.14	0.84	0.67	0.49	0.97	0.77	0.58	0.47
5.38	1.07	0.80	0.66	0.50	0.94	0.68	0.49	0.46
5.50	1.06	0.70	0.62	0.45	0.91	0.65	0.55	0.40
5.63	1.02	0.78	0.70	0.46	0.85	0.69	0.58	0.45
5.75	0.97	0.71	0.64	0.41	0.83	0.63	0.52	0.42
5.88	0.97	0.72	0.65	0.39	0.88	0.62	0.48	0.41
6.00	0.84	0.65	0.52	0.39	0.77	0.56	0.48	0.34
6.13	0.95	0.64	0.58	0.45	0.76	0.59	0.46	0.37
6.25	0.91	0.69	0.54	0.37	0.83	0.58	0.42	0.37
6.38	0.94	0.64	0.54	0.37	0.77	0.58	0.50	0.35
6.50	0.79	0.63	0.54	0.43	0.72	0.59	0.51	0.32
6.63	0.86	0.57	0.52	0.32	0.71	0.53	0.47	0.36
6.75	0.59	0.47	0.41	0.31	0.51	0.45	0.32	0.29
6.88	0.75	0.52	0.47	0.34	0.61	0.52	0.40	0.28
7.00	0.68	0.52	0.48	0.27	0.56	0.53	0.44	0.28
7.13	0.73	0.54	0.47	0.26	0.70	0.49	0.37	0.31
7.25	0.54	0.41	0.35	0.29	0.49	0.39	0.35	0.22
7.38	0.71	0.46	0.43	0.33	0.59	0.48	0.38	0.29
7.50	0.60	0.50	0.41	0.30	0.63	0.46	0.39	0.27
7.63	0.64	0.47	0.45	0.24	0.56	0.47	0.41	0.24
7.75	0.58	0.48	0.41	0.32	0.52	0.35	0.37	0.22
7.88	0.59	0.41	0.41	0.26	0.57	0.42	0.37	0.24
8.00	0.43	0.29	0.28	0.26	0.35	0.30	0.32	0.21
12.00	0.23	0.22	0.19	0.19	0.22	0.18	0.24	0.13
19.00	0.21	0.16	0.17	0.12	0.17	0.19	0.15	0.09

NOTE. — *UBVRI* and *ugriz* magnitudes are based on Vega– and AB–systems respectively. The peak magnitudes are given in Table B1, and peak, rise, and decline times for each model are given in Table B2.

Table C1. Various Magnitude offsets at the peak of He4.10

			U	B	V	R	I	u	g	r	i
CSP_{nat}	–	CSP_{AB}		0.12	0.02			0.06	0.02	0.01	-0.00
JC_{Vega}	–	JC_{AB}	-0.91	0.11	-0.02	-0.20	-0.41				
						Peak					
CSP_{nat}	–	JC_{Vega}		-0.00	0.07						
CSP_{nat}	–	$SDSS_{AB}$						0.02	-0.05	0.02	0.02
						Peak + 10 days					
CSP_{nat}	–	JC_{Vega}		-0.02	0.08						
CSP_{nat}	–	$SDSS_{AB}$						0.00	-0.09	0.01	0.04

Note. — The peak is bolometric.

C. FILTERS AND ZEROPOINTS

Observers quantify their measurements using various combinations of filters and zeropoint systems (e.g., Bessell 2005). To accommodate the historical conventions as well as the specific types of data employed in this study, we have used three sets of filters: the generic Johnson–Cousins $UBVRI$ set (Bessell 1983), the standard Sloan $ugriz$ set (SDSS), and the $uBgVri$ set employed by the Carnegie Supernova Project (CSP). All filter transmission characteristics were obtained from `svo2.cab.inta-csic.es/theory/fps`, and a comparison of their normalized transmission functions are given in Fig. C1. For the most part CSP filters have a very similar response to the equivalent filters of Johnson–Cousins and SDSS sets. There are, however, small but noticeable differences generally with the CSP filters having slightly higher transmission at longer wavelengths.

These three filter sets have been paired with three different zeropoint systems. The Johnson–Cousins set was always normalized to the Vega system, with zeropoint fluxes of 1564, 4024, 3563, 3028, 2458 Jy for U, B, V, R, and I filters respectively (also obtained from `svo2.cab.inta-csic.es/theory/fps`). The SDSS filter magnitudes were always computed in the AB system (Oke & Gunn 1983), with a constant zeropoint of 3631 Jy for all filters. Finally, the CSP filter magnitudes were computed in their "natural" system according to Krisciunas et al. (2017), using their Eq.(45) and Table 15.

Table C1 lists offsets between various choices of filters and zeropoint systems used in our study, measured at the bolometric peak of our typical model He4.10 and 10 days after peak. There is a constant offset when only the zeropoint for a given set of filters is changed. Those are listed on top where only the zeropoints from natural to AB are being varied for CSP filters and Vega to AB in Johnson-Cousins filters. The offsets in Johnson-Cousins $UBVRI$ expressed in Vega vs. AB zeropoint systems are equivalent to the differences in their corresponding zeropoint fluxes (e.g., Blanton & Roweis 2007). When both filters and zeropoints are changed the offsets are time dependent. These changes are illustrated in the remainder of the table for a typical model, He4.10, at bolometric peak and 10 days after.

The difference between CSP filter magnitudes in natural vs. AB system are negligible for our purposes, except for B and u. These values are also closely consistent with the published offsets from Krisciunas et al. (2017, see their Table 16). CSP natural magnitudes in B are essentially identical to Johnson B magnitude expressed in Vega system, while the same comparison for V yields a difference of 0.07-0.08 mag. CSP natural magnitudes in $ugri$ are also quite close to SDSS filter magnitudes in AB system, but there is about 0.09 mag offset in g at late times. Overall, the offsets do not exceed 0.1 mag within the time range in which SEDONA provides reliable results.

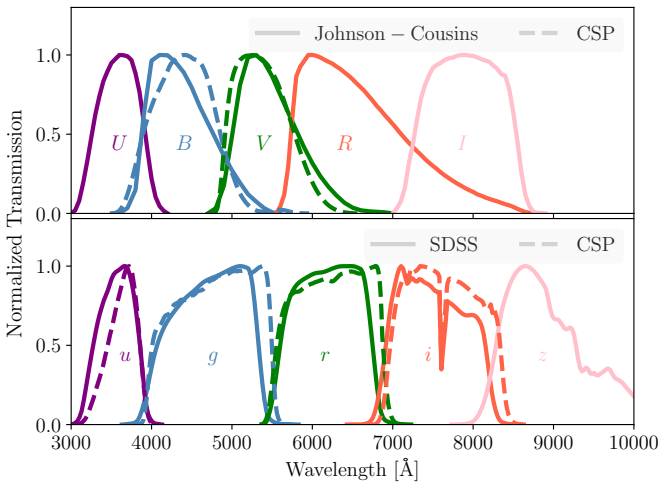

FIG. C1.— Normalized transmission functions for the three filter sets used in this study. (top:) Johnson-Cousins $UBVRI$ (solid) compared with CSP BV (dashed). (bottom:) SDSS $ugriz$ (solid) compared with CSP $ugri$ (dashed).

REFERENCES

Arnett, W. D. 1982, ApJ, 253, 785
Bersten, M. C., Tanaka, M., Tominaga, N., et al. 2013, ApJ, 767, 143
Bessell, M. S. 1983, PASP, 95, 480
Bessell, M. S. 2005, ARA&A, 43, 293
Bianco, F. B., Modjaz, M., Hicken, M., et al. 2014, ApJS, 213, 19
Blanton, M. R. & Roweis, S. 2007, AJ, 133, 734
Cano, Z. 2013, MNRAS, 434, 1098
Chen, K.-J., Moriya, T. J., Woosley, S., et al. 2017, ApJ, 839, 85
Chevalier, R. A., & Fransson, C. 2008, ApJ, 683, L135
Dessart, L., Hillier, D. J., Li, C., & Woosley, S. 2012, MNRAS, 424, 2139
Dessart, L., Hillier, D. J., Woosley, S., et al. 2015, MNRAS, 453, 2189
Dessart, L., Hillier, D. J., Woosley, S., et al. 2016, MNRAS, 458, 1618
Dessart, L., Yoon, S.-C., Livne, E., et al. 2018, A&A, 612, A61
Drout, M. R., Soderberg, A. M., Gal-Yam, A., et al. 2011, ApJ, 741, 97
Drout, M. R., Milisavljevic, D., Parrent, J., et al. 2016, ApJ, 821, 57
Ensman, L. M., & Woosley, S. E. 1988, ApJ, 333, 754
Ertl, T., Woosley, S. E., Sukhbold, T., et al. 2020, ApJ, 890, 51
Gorbikov, E., Gal-Yam, A., Ofek, E. O., et al. 2014, MNRAS, 443, 671
Hillier, D. J., & Dessart, L. 2012, MNRAS, 424, 252
Ho, A. Y. Q., Perley, D. A., Kulkarni, S. R., et al. 2020, ApJ, 895, 49. doi:10.3847/1538-4357/ab8bcf
Hunter, D. J., Valenti, S., Kotak, R., et al. 2009, A&A, 508, 371
Ioka, K., Levinson, A., & Nakar, E. 2019, MNRAS, 484, 3502
Kasen, D., Thomas, R. C., & Nugent, P. 2006, ApJ, 651, 366
Kasen, D. 2006, ApJ, 649, 939
Kasen, D., Thomas, R. C., Rpke, F., & Woosley, S. E. 2008, JPhCS, 125, 012007
Kasen, D., Metzger, B. D., & Bildsten, L. 2016, ApJ, 821, 36
Kasliwal, M. M., Kulkarni, S. R., Gal-Yam, A., et al. 2010, ApJ, 723, L98
Katz, B., Budnik, R., & Waxman, E. 2010, ApJ, 716, 781
Khatami, D. K., & Kasen, D. N. 2019, ApJ, 878, 56
Kleiser, I., Fuller, J., & Kasen, D. 2018, MNRAS, 481, L141
Kleiser, I. K. W., Kasen, D., & Duffell, P. C. 2018, MNRAS, 475, 3152
Krisciunas, K., Contreras, C., Burns, C. R., et al. 2017, AJ, 154, 211
Kurucz, R. L. 1994, CD-ROM 1, Atomic Data for Opacity Calculations (Cambridge: SAO)
Kurucz, R. L., & Bell, B. 1995, CD-ROM 23, Atomic Line List (Cambridge: SAO)
Kurucz, R. L. 2009, American Institute of Physics Conference Series, 1171, 43
Lucy, L. B. 1991, ApJ, 383, 308
Lyman, J. D., Bersier, D., James, P. A., et al. 2016, MNRAS, 457, 328
Malesani, D., Fynbo, J. P. U., Hjorth, J., et al. 2009, ApJ, 692, L84
Maund, J. R. & Ramirez-Ruiz, E. 2016, MNRAS, 456, 3175
Mazzali, P. A., Maurer, I., Valenti, S., et al. 2010, MNRAS, 408, 87
Modjaz, M., Li, W., Butler, N., et al. 2009, ApJ, 702, 226
Modjaz, M., Blondin, S., Kirshner, R. P., et al. 2014, AJ, 147, 99
Moriya, T. J., Mazzali, P. A., Tominaga, N., et al. 2017, MNRAS, 466, 2085.
Oke, J. B. & Gunn, J. E. 1983, ApJ, 266, 713
Piro, A. L. 2015, ApJ, 808, L51
Poznanski, D., Chornock, R., Nugent, P. E., et al. 2010, Science, 327, 58
Prentice, S. J., Mazzali, P. A., Pian, E., et al. 2016, MNRAS, 458, 2973
Prentice, S. J., Ashall, C., James, P. A., et al. 2019, MNRAS, 485, 1559
Richardson, D., Branch, D., & Baron, E. 2006, AJ, 131, 2233
Roth, N., & Kasen, D. 2015, ApJS, 217, 9
Sahu, D. K., Gurugubelli, U. K., Anupama, G. C., et al. 2011, MNRAS, 413, 2583
Salpeter, E. E. 1955, ApJ, 121, 161
Sapir, N., Katz, B., & Waxman, E. 2013, ApJ, 774, 79
Soderberg, A. M., Berger, E., Page, K. L., et al. 2008, Nature, 453, 469
Shivvers, I., Filippenko, A. V., Silverman, J. M., et al. 2019, MNRAS, 482, 1548
Stritzinger, M., Mazzali, P. A., Sollerman, J., et al. 2006, A&A, 460, 793
Stritzinger, M., Mazzali, P., Phillips, M. M., et al. 2009, ApJ, 696, 713
Stritzinger, M. D., Anderson, J. P., Contreras, C., et al. 2018a, A&A, 609, A134
Stritzinger, M. D., Taddia, F., Burns, C. R., et al. 2018b, A&A, 609, A135
Stritzinger, M. D., Taddia, F., Holmbo. S. et al. 2020, A&A, 634, A21
Sukhbold, T., Ertl, T., Woosley, S. E., et al. 2016, ApJ, 821, 38
Sukhbold, T., Woosley, S. E., & Heger, A. 2018, ApJ, 860, 93
Taddia, F., Sollerman, J., Leloudas, G., et al. 2015, A&A, 574, A60
Taddia, F., Fremling, C., Sollerman, J., et al. 2016, A&A, 592, A89
Taddia, F., Stritzinger, M. D., Bersten, M., et al. 2018, A&A, 609, A136
Tauris, T. M., Langer, N., Moriya, T. J., et al. 2013, ApJ, 778, L23.
Tauris, T. M., Langer, N., & Podsiadlowski, P. 2015, MNRAS, 451, 2123
Valenti, S., Elias-Rosa, N., Taubenberger, S., et al. 2008, ApJ, 673, L155
Valenti, S., Fraser, M., Benetti, S., et al. 2011, MNRAS, 416, 3138
Weaver, T. A., Zimmerman, G. B., & Woosley 1978, ApJ, 225, 1021
Wongwathanarat, A., Janka, H.-T., Müller, E., Pllumbi, E., & Wanajo, S. 2017, ApJ, 842, 13
Woosley, S. E., Langer, N., & Weaver, T. A. 1995, ApJ, 448, 315
Woosley, S. E., & Eastman, R. G. 1997, NATO Advanced Science Institutes (ASI) Series C, 821
Woosley, S. E. 2019, ApJ, 878, 49
Woosley, S. E., Sukhbold, T, & Janka, T. H. 2020, ApJ, in press
Yoon, S.-C. 2017, MNRAS, 470, 3970
Yoon, S.-C., Chun, W., Tolstov, A., et al. 2019, ApJ, 872, 174